



Transport of heat and mass for reactive gas mixtures in porous media: Modeling and application

David Brust^{a,d} , Katharina Hopf^c , Jürgen Fuhrmann^c , Andrii Cheilytko^b ,
Michael Wullenkord^a , Christian Sattler^{a,d} 

^a German Aerospace Center - Institute of Future Fuels, Im Langenbroich 13, 52428 Jülich, Germany

^b German Aerospace Center - Institute of Solar Research, Im Langenbroich 13, 52428 Jülich, Germany

^c Weierstrass Institute, Mohrenstraße 39, 10117 Berlin, Germany

^d RWTH Aachen University, Faculty of Mechanical Engineering, Chair for Solar Fuel Production, 52062 Aachen, Germany

ARTICLE INFO

Dataset link: <https://github.com/DavidBrust/MultiComponentReactiveMixtureProject>

Keywords:

Modeling

Porous media

Two-scale homogenization

Photo-thermal reactor

Thermodiffusion

ABSTRACT

We present a modeling framework for multi-component, reactive gas mixtures and heat transport in porous media based on the Maxwell–Stefan and Darcy equations for multi-component diffusion and forced, viscous flow through porous media. Analysis of the model equations reveals thermodynamic consistency and uniqueness of steady states, while their mathematical structure facilitates discretization via the Finite-Volume approach resulting in an open-source based implementation of the modeling framework in *Julia*. The model allows imposing boundary conditions that accurately reflect the conditions prevailing in a photo-thermal chemical reactor that is subsequently introduced as a case study for the modeling framework. Comparison of numerical with experimental results reveals good agreement. Improvement options for the physical reactor are derived from simulation results demonstrating the practical utility of the modeling framework. Additionally, the framework is used for the simulation of thermodiffusion in a ternary gas mixture and has been verified with published numerical results with very good agreement.

1. Introduction

Multi-component gas transport in porous media plays an important role in many present and emerging applications, among which are oil and gas exploration, environmental remediation, carbon sequestration [1], applications in chemical engineering such as catalysis and adsorptive separation [2], in the gas diffusion layers of electrochemical devices [3] and in solar reactors employing porous structures as catalyst or as receiver material [4].

Classically, multi-component gas phase mass transport was described in the Maxwell–Stefan (M–S) formulation [5] when diffusion is the dominating mass transport process. Modeling of multi-component mass transport involving porous media often requires the incorporation of viscous convective flow. Further, microporous structures with pore sizes comparable to the mean free path length of the gas cause the flow regime to deviate from continuum flow such that Knudsen diffusion must be considered. The most widely used model in this context is the Dusty Gas Model (DGM) [6]. In the DGM the solid porous structure (“dust”) is treated as an additional species in the gas phase, giving the DGM its name. As microscale features of the porous medium are not resolved geometrically in this approach, the characteristics of the porous medium impacting gas transport are accounted for via modification of the transport coefficients into effective transport coefficients. Variations of the DGM were developed in the form of the Mean Transport Pore Model Mean Transport Pore Model (MTPM) [7] and the Binary Transport Model Binary Transport Model (BTM) [8]. All three models have in common, that in the description of species mass transport they incorporate contributions from convective species fluxes with diffusive species fluxes into a combined total species flux. This yields a single equation per species which is similar in form to a diffusive flux equation in the M–S formulation that relates the total species flux to the driving forces. Another more recent contribution places emphasis on momentum transfer in mixture flow through porous media by incorporating momentum conservation equations along the mass conservation equations for each species contained in the gas phase mixture [2]. Thus, interspecies momentum exchange and gas–wall interactions are defined for each species separately. The authors also considered simultaneous heat transfer based on the assumption of local thermodynamic

* Corresponding author.

E-mail address: david.brust@dlr.de (D. Brust).

<https://doi.org/10.1016/j.cej.2025.162027>

Received 6 November 2024; Received in revised form 4 March 2025; Accepted 25 March 2025

Available online 30 April 2025

1385-8947/© 2025 The Authors. Published by Elsevier B.V. This is an open access article under the CC BY license (<http://creativecommons.org/licenses/by/4.0/>).

equilibrium between the gas and solid phases and by adopting a pseudo-homogeneous form of the energy equation with effective heat transfer properties of the gas mixture and the porous medium. The model is implemented in the commercial computational fluid dynamics (CFD) code FLUENT® by manipulation of the code's *Eulerian multiphase model* [2]. Alternatively, models based on the Lattice Boltzmann Method (LBM), a method that simulates fluid flow by describing molecule collisions and scattering on a mesoscopic scale have gained increasing attention due to the simplicity in implementation, scalability on parallel computers and favorable handling of complex geometries [9]. An application of the LBM for the simulation of flow, heat and species transport in porous media is presented in [10] where novel formulations for the equilibrium distribution functions are proposed that are calculated from macroscopic quantities and thus allow the specification of boundary conditions corresponding to boundary conditions defined in terms of macroscopic quantities.

In this work a model for multi-component gas phase heat and mass transfer in rigid, isotropic porous media is presented. It differentiates itself from the established models (DGM, MTPM, BTM) in that it formulates separate equations for convective fluxes stemming from bulk viscous flow and diffusive fluxes. The superposition of convective and diffusive fluxes is handled in the species mass balance. This alleviates criticism of the established models which lump convective and diffusive fluxes together, although they are physically different phenomena [11]. Further, the proposed model facilitates the definition of boundary conditions that arise from the physical system under consideration. To this end, the model is presented in three steps. First, after preliminary definitions in Section 2.1, gas phase balance equations describing multi-component species transport on the pore scale in isothermal conditions are presented in Section 2.2.1.

Second, the gas-phase equations are complemented to account for non-isothermal conditions by introducing an energy equation including the Dufour effect of multi-component heat transport originating from mass transport and by extending the driving forces for species mass diffusion to include thermodiffusion, referred to as Soret effect, in Section 2.2.2.

Third, the porous medium which in the scope of this study consists of a rigid, isotropic porous solid phase whose pore volume is filled by a gas phase mixture is introduced. Homogenized equations describing gas phase flow, multi-component species transport including chemical reactions and heat transport on the macroscopic scale in the porous medium are presented in Section 2.3 with detailed derivations based on the two-scale expansion method in Appendix E. Their thermodynamic consistency under isothermal conditions is analyzed in Section 2.3.1.

In Section 3 the model implementation based on the Finite-Volume approach and the open-source code *VoronoiFVM.jl* [12] is introduced alongside with the discretized forms of model equations.

Applications of the model are demonstrated in Section 4 where first, simulations of a photo-thermal catalytic reactor (PTR) that was recently investigated experimentally are presented and discussed in the context of the experimental setup and boundary conditions. Second, the capability of the model and implementation to account for thermodiffusion (Soret effect) in mixtures of gases in absence of porous media is demonstrated by reproducing a simulation of gas separation of a ternary noble gas mixture contained in a closed vessel by application of a temperature gradient [13].

We conclude with a summary and outlook on future work in Section 5.

2. Modeling

Remark 2.1. Since homogenized equations on the Darcy scale are derived from pore scale equations as part of this work, throughout this section the scale for which the respective equations are valid is indicated in the relevant subsection headings for clarity.

2.1. Preliminaries

We let $\rho = (\rho_1, \dots, \rho_n)$ denote the partial mass densities of the n gas species in the mixture with the total mass density $\rho = \sum_{i=1}^n \rho_i$. The molar mass of the i th species will be denoted by M_i . Then the partial and total molar densities, commonly referred to as concentrations, can be expressed as $c_i = \rho_i/M_i$ and $c = \sum_{i=1}^n c_i$. The molar and mass fractions are given by $x_i = c_i/c$ and $w_i = \rho_i/\rho$, respectively. By definition, it holds that $\sum_{i=1}^n x_i = 1 = \sum_{i=1}^n w_i$. Finally, the mean molar mass of the gas mixture follows as $M_{\text{mix}} = \sum_{i=1}^n x_i M_i$.

The ideal gas law is used as the constitutive equation for the mixture of ideal gases and relates the total pressure, total mass density and temperature via

$$p = \frac{\rho}{\sum_{i=1}^n x_i M_i} RT. \quad (2.1)$$

Since $\sum_{i=1}^n x_i M_i = \sum_{i=1}^n \rho_i \frac{1}{c}$, we can write equivalently

$$p = c RT = \sum_{i=1}^n \frac{\rho_i}{M_i} RT. \quad (2.2)$$

2.2. Gas phase balance equations (pore scale)

2.2.1. Isothermal case

Under isothermal conditions, the state of a gas phase mixture is fully characterized by the vector of mass densities $\rho = (\rho_1, \dots, \rho_n)$, whose evolution we assume to be governed by

$$\partial_t \rho_i + \nabla \cdot (\rho_i \vec{v}) + \nabla \cdot \vec{J}_i = r_i(\rho), \quad i = 1, \dots, n. \quad (2.3)$$

Here, \vec{v} denotes the mass-averaged (barycentric) velocity that in the general case can be obtained by solving the Navier–Stokes equations. Moreover, $\vec{J}_i, i = 1, \dots, n$ and $r_i, i = 1, \dots, n$ denote the species mass diffusion fluxes and the reaction rates. Throughout this work, they are chosen in a way as to satisfy

$$\sum_{i=1}^n \vec{J}_i \equiv 0, \quad (2.4)$$

$$\sum_{i=1}^n r_i \equiv 0. \quad (2.5)$$

Summing (2.3) over $i = 1, \dots, n$, and using (2.4), (2.5), we deduce the continuity equation

$$\partial_t \rho + \nabla \cdot (\rho \vec{v}) = 0 \quad (2.6)$$

for the total mass density. The diffusion fluxes \vec{J}_i are determined by the M-S formulation of multi-component diffusion [14–16]. In the isothermal case, the M-S equations take the form

$$\frac{p}{RT} \frac{1}{M_{\text{mix}}} \vec{d}_i = - \sum_{\substack{j=1 \\ j \neq i}}^n \frac{w_j \vec{J}_i - w_i \vec{J}_j}{\mathcal{D}_{ij} M_i M_j}, \quad i = 1, \dots, n, \quad (2.7)$$

with the so-called diffusive driving forces

$$\vec{d}_i = \nabla x_i + (x_i - w_i) \nabla p / p, \quad i = 1, \dots, n, \quad (2.8)$$

and the M-S diffusivities $\mathcal{D}_{ij} > 0$.

Notice that $\sum_{i=1}^n \vec{d}_i = 0$ as a consequence of $\sum_{i=1}^n x_i = 1 = \sum_{i=1}^n w_i$ and that of the n M-S Eqs. (2.7) at most $n - 1$ are linearly independent. In fact, the linear system (2.7) complemented by (2.4) forms a well-posed problem [15], ensuring the unique solvability for $(\vec{J}_i)_{i=1}^n$.

2.2.2. Non-isothermal case (pore scale)

In this section, temperature T is allowed to vary, and the mixture model (2.3) will be complemented by a thermal energy equation for an ideal gas mixture along the lines of [15,17]. We limit the scope of the model to flows with low velocity considering the intended application to flows in porous media as elaborated in Section 2.3. Thus, the total energy reduces to the internal energy, whose density is given by ρe , where e denotes the specific internal energy. Then, the mass continuity Eqs. (2.3) are complemented by a conservation law for the internal energy density ρe of the gas phase

$$\partial_t (\rho e) + \nabla \cdot (\rho e \vec{v}) + \nabla \cdot (p \vec{v}) + \nabla \cdot \vec{Q} = 0, \quad (2.9)$$

where \vec{Q} denotes the heat flux. Furthermore, in the non-isothermal case, the M-S equations for the diffusion fluxes \vec{J}_i take the adjusted form

$$\frac{p}{RT} \frac{1}{M_{\text{mix}}} \vec{d}'_i = - \sum_{j: j \neq i} \frac{w_j \vec{J}_i - w_i \vec{J}_j}{M_i M_j \mathcal{D}_{ij}}, \quad i = 1, \dots, n, \quad (2.10)$$

with the adjusted diffusive driving forces \vec{d}'_i additionally depending on the temperature gradient

$$\begin{aligned} \vec{d}'_i &= \vec{d}_i + x_i \widetilde{\mathcal{X}}_i \nabla \log T \\ &= \nabla x_i + (x_i - w_i) \nabla \log p + x_i \widetilde{\mathcal{X}}_i \nabla \log T, \quad i = 1, \dots, n. \end{aligned} \quad (2.11)$$

Here, $\widetilde{\mathcal{X}} = (\widetilde{\mathcal{X}}_i)_{i=1}^n$ are rescaled thermal diffusion ratios defined via

$$\widetilde{\mathcal{X}}_i = \sum_{j=1}^n \frac{x_j}{\mathcal{D}_{ij}} (D_i^T - D_j^T), \quad (2.12)$$

where D_i^T are the barycentric coefficients of thermal diffusion [14], see also [18]. Note that $\sum_{i=1}^n \widetilde{\mathcal{X}}_i x_i = 0$ because of the symmetry of \mathcal{D}_{ij} , and consequently $\sum_{i=1}^n \vec{d}'_i = \sum_{i=1}^n \vec{d}_i = 0$. Thus, again we see that the n Eqs. (2.10) are linearly dependent. As before, they are complemented by the constraint (2.4).

In the context of heat transfer in multi-component mixtures, the total diffusive heat flux \vec{Q} consisting of ordinary heat conduction and the net heat flux following from differing diffusive fluxes of the various gas phase species in the mixture (Dufour effect) takes the following form [13,14,18]:

$$\vec{Q} = -\lambda \nabla T + \sum_{i=1}^n \left(h_i + RT \widetilde{\mathcal{X}}_i / M_i \right) \vec{J}_i \quad (2.13)$$

where h_i is the mass specific enthalpy of gas phase species i and λ is the thermal conductivity of the gas phase mixture. It should be noted that the Soret and Dufour effects are not considered in the simulation of the PTR involving porous media in Section 4.1 due to uncertainty in the calculation of the respective coefficients in the multi-component mixture as experimental data on thermodiffusion coefficients for the gas species considered in the study is scarce [19,20] while the determination of the influence of porous media on thermodiffusion for the application considered in this work in the context of the homogenization method is left for future work. Instead of the internal energy equation (2.9), we may equivalently impose a balance law for the enthalpy $\rho h = \rho e + p$. Using (2.6) and (2.9) the enthalpy equation can be computed as

$$\partial_t (\rho h) + \nabla \cdot (\rho h \vec{v}) + \nabla \cdot \vec{Q} = \partial_t p. \quad (2.14)$$

For the derivation of homogenized equations valid for the porous solid and gas phase shown in Appendix E we reformulate the gas phase enthalpy Eq. (2.14) expressed in terms of the absolute enthalpy of the gas phase mixture $h = \sum_{i=1}^n w_i h_i$ as follows:

$$h_i = h_i^0 + \int_{T_{\text{ref}}}^T c_{p,i}(\widetilde{T}) d\widetilde{T} \quad (2.15)$$

$$= h_i^0 + h_i^{\text{th}}(T) \quad (2.16)$$

where h_i^0 is the enthalpy of formation at reference conditions ($T = 298.15 \text{ K}$, $p = 1 \text{ bar}_a$) and $h_i^{\text{th}}(T)$ is the thermal enthalpy. Rearranging as in [Appendix A](#) we thus obtain

$$\begin{aligned} \frac{\partial(\rho h^{\text{th}})}{\partial t} + \nabla \cdot (\rho h^{\text{th}} \vec{v}) + \nabla \cdot \left(\sum_{i=1}^n (h_i^{\text{th}} + RT \widetilde{\chi}_i / M_i) \vec{J}_i \right) \\ + \nabla \cdot (-\lambda \nabla T) + \sum_{i=1}^n h_i^0 r_i - \frac{\partial p}{\partial t} = 0 \end{aligned} \quad (2.17)$$

To further simplify the derivation of the homogenized heat transport equation, we neglect the terms associated with the multi-component diffusive mass fluxes \vec{J}_i and the heat source from dynamic pressure changes $\partial p / \partial t$ to obtain:

$$\frac{\partial(\rho h^{\text{th}})}{\partial t} + \nabla \cdot (\rho h^{\text{th}} \vec{v}) - \nabla \cdot (\lambda \nabla T) = - \underbrace{\sum_{i=1}^n h_i^0 r_i}_q \quad (2.18)$$

including heat source term q originating from bulk gas phase chemical reactions as described in [Appendix E.2](#). We approximate the temperature dependency of gas heat capacities by a mean value in the temperature interval of interest such that we can write:

$$h_i^{\text{th}}(T) \approx \bar{c}_{p,i} \underbrace{(T - T_{\text{ref}})}_{\hat{T}} \quad (2.19)$$

where we define $\hat{T} = T - T_{\text{ref}}$ with $\nabla \hat{T} = \nabla T$ to simplify notation. Thus, the derivation of the homogenized equation of heat transport in [Appendix E.3](#) starts from the following equation of heat transport in the gas phase:

$$\frac{\partial(\rho c_p \hat{T})}{\partial t} + \nabla \cdot (\rho c_p \hat{T} \vec{v}) - \nabla \cdot (\lambda \nabla \hat{T}) = q \quad (2.20)$$

with the heat capacity of the gas mixture $c_p = \sum_{i=1}^n w_i c_{p,i}$.

2.3. Porous solid phase and Darcy closure (Darcy scale)

This work focuses on the macroscopic description of transport processes occurring in a multi-component gas phase mixture occupying the pore space of a rigid, isotropic porous solid. Common techniques to derive macroscopic or darcy-scale equations from the pore scale equations are the volume averaging method, that relies on the definition of a representative elementary volume for spatial-averaging and obtains darcy-scale equations via the general transport theorem [21–24] and the homogenization method using two-scale expansions [25,26]. The latter is used in this work as outlined in [Appendix E](#). Though both procedures provide the same effective models and parameters when applied correctly, the homogenization method is used in this work as it has the potential to provide convergence proofs for the homogenized equations [27].

Homogenized equations for flow of the gas phase mixture through the pore space, species mass transport including chemical reactions, as well as thermal energy (heat) transport in the porous medium are derived in [Appendix E](#). As explained in Section 2.3.2 in this study we assume radial symmetry on the pore scale, permitting the use of scalar-valued parameters while effective model parameters corresponding to the real pore scale geometry will be calculated in future work. For the remainder of the text, the void fraction or porosity of the porous medium ϕ is defined as the ratio of void volume to total volume: $\phi = V_{\text{void}} / V_{\text{total}}$ with the solid fraction $1 - \phi = V_{\text{solid}} / V_{\text{total}}$. Further, we introduce the volumetric averaging operator that yields quantities that are spatially averaged over the volume of one representative elementary volume Ω of the porous medium:

$$\langle \cdot \rangle = \frac{1}{|\Omega|} \int_{\Omega} \cdot d\tilde{\Omega} \quad (2.21)$$

The derivation of effective media equations for compressible, non-isothermal gas phase flow through rigid, porous media is shown in [Appendix E.1](#) and to first order of approximation within the framework of two-scale expansions leads to the well-known Darcy equation:

$$\langle \vec{v} \rangle = -\mathbf{K} / \eta \nabla p \quad (2.22)$$

where $\eta > 0$ is the dynamic viscosity of the gas phase.

The columns of permeability tensor \mathbf{K} appearing in (2.22) correspond to $\langle \vec{k}_k \rangle$ for $k = 1, \dots, d$, the solutions of the so-called ‘‘cell’’ problems (\widehat{P}_k) [25] formulated during the homogenization procedure. \mathbf{K} is scaled by the square of the mean pore size d_p :

$$\mathbf{K} = d_p^2 \langle \vec{k}_1 \rangle \quad \dots \quad \langle \vec{k}_d \rangle \quad (2.23)$$

As the exact pore scale geometry of the porous medium is unknown and its determination via imaging techniques is out of the scope of this study, we cannot calculate \mathbf{K} from (2.23). Instead, we assume periodic grain structure at the pore scale with radially symmetric grains located in the center of the period leading to a scalar valued effective permeability $K > 0$ for which empirical values are known [28]. It should be noted that application of the averaging operator (E.7) yields a volume mean while we expect $\langle \vec{v} \rangle$ to be a flux and thus a surface mean. The equivalence of volume and surface means is shown in [26, Section 7.2.2.1] and holds for $\langle \vec{v} \rangle$ and $\langle \vec{J}_i \rangle$ in this text. Equations for multi-component species mass transport in a porous medium including chemical reactions are derived in [Appendix E.2](#). Chemical reactions are treated as bulk reactions taking place in the gas phase based on the argument of negligible mass transfer resistance as detailed in [Appendix E.2](#). The M–S formulation was chosen to describe the multi-component diffusion of gas phase species occupying the pore space. Thus, to first order of approximation in the framework of two-scale expansions we obtain:

$$\phi \frac{\partial \rho_i}{\partial t} + \nabla \cdot (\rho_i \langle \vec{v} \rangle + \langle \vec{J}_i \rangle) = \phi r_i(\varrho) \quad (2.24)$$

with the diffusive species mass fluxes $\langle \vec{J}_i \rangle$ in M-S formulation for $i = 1 \dots n - 1$:

$$-\sum_{\substack{j=1 \\ j \neq i}}^n x_j \langle \mathcal{D}_{ij}^{\text{eff}} \rangle^{-1} \left(\frac{\langle \vec{J}_i \rangle}{\rho_i} - \frac{\langle \vec{J}_j \rangle}{\rho_j} \right) = \nabla x_i + (x_i - w_i) \nabla p / p \quad (2.25)$$

complemented by:

$$\sum_{i=1}^n \langle \vec{J}_i \rangle = 0 \quad (2.26)$$

Summing (2.24) over $i = 1, \dots, n$, using (2.26), (2.5) we recover the mass conservation equation

$$\phi \frac{\partial \rho}{\partial t} + \nabla \cdot (\rho \langle \vec{v} \rangle) = 0. \quad (2.27)$$

In (2.25) the effective M-S diffusivities can be obtained via

$$\langle \mathcal{D}_{ij}^{\text{eff}} \rangle = \mathcal{D}_{ij} \langle \mathbf{I} + \nabla_{\mathbf{y}^*} \otimes \vec{\chi} \rangle \quad (2.28)$$

with the gas phase M-S diffusivities \mathcal{D}_{ij} and $\vec{\chi}$ being the solution of cell problems (MT_k). As for the other effective transport parameters we do not calculate $\langle \mathcal{D}_{ij}^{\text{eff}} \rangle$ from (2.28) but instead, in this work the $\mathcal{D}_{ij}^{\text{eff}} > 0$ are scalars obtained from empirical correlation shown in Section 2.3.2. The derivation in Appendix E.2 only considers molar fraction gradients ∇x_i as driving forces for diffusion to simplify notation. Inclusion of the pressure gradient term $(x_i - w_i) \nabla p / p$ follows without complication and leads to (2.25) as was demonstrated in [29]. Further, in the context of the porous medium, thermodiffusion (Soret effect) is not considered due to uncertainty in deriving effective thermodiffusion coefficients.

Homogenized equations for heat transport in porous media are derived in Appendix E.3. There, on the pore scale heat transport in the gas phase via conduction-advection accompanied by heat source originating from bulk chemical reactions as described in (2.20) are considered. In the porous solid phase, heat is transported via conduction. Heat exchange driven by the local difference in temperatures between the phases is described by a heat transfer coefficient.

Taking into account the relative magnitude of different terms relevant in our application as part of the homogenization procedure, to first order of approximation in the framework of two-scale expansions we obtain for heat transport in the porous medium:

$$(1 - \phi) \rho_s c_s \frac{\partial T}{\partial t} + \nabla \cdot (c \rho T \langle \vec{v} \rangle) - \nabla \cdot (\langle \lambda^{\text{eff}} \rangle \nabla T) = \phi q \quad (2.29)$$

with the density and heat capacity of the solid phase ρ_s and c_s and the mixture density and heat capacities in the gas phase $\rho = \sum_{i=1}^n \rho_i$ and $c = \sum_{i=1}^n w_i c_{p,i}$, the heat source term q from gas phase chemical reactions and further with the effective thermal conductivity $\langle \lambda^{\text{eff}} \rangle$:

$$\langle \lambda^{\text{eff}} \rangle = \lambda_f \langle \mathbf{I} + \nabla_{\mathbf{y}^*} \otimes \vec{t}_f \rangle \quad (2.30)$$

where \vec{t}_f is the solution of the cell problems (HT_k). A single temperature field, corresponding to thermal equilibrium between the gas and solid phase, describes the effective medium following the homogenization procedure given the scaling properties of our application. For different conditions thermal non-equilibrium between the phases could occur, and homogenization would lead to separate heat transport equations for each phase as demonstrated in [26] which could be implemented in the model in future work. As for the permeability \mathbf{K} and effective diffusivities $\mathcal{D}_{ij}^{\text{eff}}$, in this study we assume that the effective thermal conductivity is a scalar $\lambda^{\text{eff}} > 0$ and is calculated as shown in Section 2.3.2.

Summarizing, the isothermal model at Darcy scale consists of the equations for species mass transport (2.24), the Darcy (2.22) and M-S Eqs. (2.25), (2.26) with the ideal gas law (2.1) as constitutive relation. In the non-isothermal case the iso-thermal equations are complemented by the homogenized heat transport Eq. (2.29).

2.3.1. Free energy (Darcy scale)

In this subsection, focus on the isothermal case and show that the simplified PDE system with fixed temperature $T > 0$ is compatible with basic thermodynamic modeling in the sense that we identify a *Lyapunov functional* (see e.g. Definition 1.1 in [30]) which can be regarded as a free energy of the system. For a related approach with a van der Waals pressure law, we refer to [31]. Our results are valid under the mild hypotheses of symmetry and positive definiteness of the effective permeability tensor \mathbf{K} and effective diffusivities $\langle \mathcal{D}_{ij}^{\text{eff}} \rangle$:

- For all $\eta, \tilde{\eta} \in \mathbb{R}^d$ and all $i, j = 1, \dots, n$:

$$\tilde{\eta}^T \mathbf{K} \eta = \eta^T \mathbf{K} \tilde{\eta} \quad \tilde{\eta}^T \langle \mathcal{D}_{ij}^{\text{eff}} \rangle \eta = \eta^T \langle \mathcal{D}_{ij}^{\text{eff}} \rangle \tilde{\eta} \quad (S)$$

- For all $\eta \in \mathbb{R}^d \setminus \{0\}$ and all $i, j = 1, \dots, n$:

$$\eta^T \mathbf{K} \eta > 0 \quad \eta^T \langle \mathcal{D}_{ij}^{\text{eff}} \rangle \eta > 0. \quad (P)$$

Here, $d \in \mathbb{N}$ denotes the dimension of the physical space. The derivation of the symmetry and positive definiteness properties (S), (P) of effective homogenized tensors in prototypical situations can be found in classical literature, see Proposition 3.2 in [25, Chapter 1], for instance. We will further use the tensor identity $\langle \mathcal{D}_{ij}^{\text{eff}} \rangle = \langle \mathcal{D}_{ji}^{\text{eff}} \rangle$ for all $i, j = 1, \dots, n$, which is a direct consequence of formula (2.28) and the fact that $\mathcal{D}_{ij} = \mathcal{D}_{ji}$.

In the following, we suppose that the equations are formulated on a bounded spatial domain with *Lipschitz continuous boundary* (see Definition 1.2.1.1 in [32]) and complemented by no-flux boundary conditions. We assume, without loss of generality, that the fixed temperature T is the standard temperature. We further let p^{st} denote the standard pressure and $\rho_i^{\text{st}} = M_i \frac{p^{\text{st}}}{RT}$ the associated standard density of the i th species. As the free energy density of the model, we take

$$f(\phi) = \phi RT \sum_{i=1}^n \frac{\rho_i}{M_i} (\log(\rho_i / \rho_i^{\text{st}}) - 1).$$

Observe that

$$\mu_i := \frac{\partial f}{\partial \rho_i}(\rho) = \phi \frac{RT}{M_i} \log(\rho_i / \rho_i^{\text{st}}). \quad (2.31)$$

This yields the relation $f(\rho) + \phi p = \phi \sum_{i=1}^n RT \frac{\rho_i}{M_i} \log(\rho_i / \rho_i^{\text{st}}) = \sum_{i=1}^n \rho_i \mu_i$, which is reminiscent of the Gibbs–Duhem equation (cf. [33, Section 5]). As a consequence, we further have

$$\sum_{i=1}^n \rho_i \nabla \mu_i = \phi \nabla p. \quad (2.32)$$

Let now $F(\rho) = \int f(\rho) dx$ denote the free energy functional, where here and in the rest of this subsection, we do not explicitly indicate the space domain of integration. We assert that F is dissipated along sufficiently regular solutions ρ of (2.24), (2.22) obeying no-flux boundary conditions and positivity $\rho_i > 0$, $i = 1, \dots, n$, if the reaction rates $(r_i)_i$ are dissipative in the sense that $\sum_{i=1}^n \mu_i r_i(\rho) \leq 0$ or, equivalently,

$$\sum_{i=1}^n \frac{RT}{M_i} r_i(\rho) \log(\rho_i / \rho_i^{\text{st}}) \leq 0 \quad \text{for all } \rho \in (0, \infty)^n. \quad (2.33)$$

To show the asserted non-increase of the free energy, we compute using identities (2.24), (2.22), integration by parts, as well as (2.32)

$$\begin{aligned} \frac{d}{dt} F(\rho) &= \int \sum_{i=1}^n \mu_i \partial_t \rho_i \\ &= -\frac{1}{\eta} \int \mathbf{K} \nabla p \cdot \nabla p + \int \sum_{i=1}^n \frac{1}{\phi} \nabla \mu_i \cdot \langle \vec{J}_i \rangle + \int \sum_{i=1}^n \mu_i r_i(\rho). \end{aligned} \quad (2.34)$$

The first and third term on the right-hand side of (2.34) are non-positive since \mathbf{K} is positive definite, since $\eta > 0$, and due to (2.33). For treating the second term, we reformulate the M–S relations. Using the identities $\rho_i = c M_i x_i$, $w_i = \frac{c}{\rho} x_i M_i$, and $\frac{\nabla \rho_i}{\rho_i} = \frac{\nabla p}{p} + \frac{\nabla x_i}{x_i}$, we deduce from (2.25) and (2.26) that for $i = 1, \dots, n$

$$M_i x_i \left(\frac{1}{M_i} \frac{\nabla \rho_i}{\rho_i} - \frac{c}{\rho} \frac{\nabla p}{p} \right) = - \sum_{j:j \neq i} \frac{1}{c M_i M_j} \langle \mathbf{D}_{ij}^{\text{eff}} \rangle^{-1} \left(M_j x_j \langle \vec{J}_i \rangle - M_i x_i \langle \vec{J}_j \rangle \right).$$

Multiplying the last equation by $\frac{c}{M_i x_i}$, which is admissible if $x_i > 0$ for all i , and recalling (2.31), we further infer for $i = 1, \dots, n$

$$\frac{c}{RT} \left(\frac{1}{\phi} \nabla \mu_i - \frac{1}{\rho} \nabla p \right) = - \sum_{j:j \neq i} \frac{1}{M_i M_j} \langle \mathbf{D}_{ij}^{\text{eff}} \rangle^{-1} \left(\frac{M_j x_j}{M_i x_i} \langle \vec{J}_i \rangle - \langle \vec{J}_j \rangle \right),$$

Thus,

$$\frac{c}{RT} \left(\frac{1}{\phi} \nabla \mu_i - \frac{1}{\rho} \nabla p \right) = - \langle \mathbf{A}(\rho) \langle \vec{J} \rangle \rangle_i, \quad i = 1, \dots, n, \quad (2.35)$$

where $\langle \vec{J} \rangle = (\langle \vec{J}_1 \rangle, \dots, \langle \vec{J}_n \rangle)^T$ and with the understanding that

$$\langle \mathbf{A}(\rho) \langle \vec{J} \rangle \rangle_i = \sum_{j=1}^n \mathbf{A}_{ij}(\rho) \langle \vec{J}_j \rangle,$$

where we have introduced the tensor-valued matrix $\mathbf{A} = (\mathbf{A}_{ij})_{i,j=1}^n$, $\mathbf{A}_{ij} \in \mathbb{R}_{\text{sym}}^{d \times d}$, given by

$$\mathbf{A}_{ij}(\rho) = \begin{cases} \sum_{k:k \neq i} \frac{1}{M_i^2} \frac{x_k}{x_i} \langle \mathbf{D}_{ik}^{\text{eff}} \rangle^{-1} & \text{if } j = i, \\ -\frac{1}{M_i M_j} \langle \mathbf{D}_{ij}^{\text{eff}} \rangle^{-1} & \text{if } j \neq i. \end{cases}$$

If $\rho_i > 0$ for all i , it holds that for all $\vec{\zeta} \in \mathbb{R}^{d \times n}$, $\vec{\zeta} = (\vec{\zeta}_1, \dots, \vec{\zeta}_n)$,

$$\langle \mathbf{A}(\rho) \vec{\zeta} \rangle_i = \sum_{j=1}^n \frac{1}{M_i M_j} \langle \mathbf{D}_{ij}^{\text{eff}} \rangle^{-1} \left(\frac{w_j}{w_i} \vec{\zeta}_i - \vec{\zeta}_j \right),$$

and therefore

$$\begin{aligned} \vec{\zeta} : \mathbf{A}(\rho) \vec{\zeta} &= \sum_{i,j=1}^n \sqrt{\frac{w_j}{w_i}} \vec{\zeta}_i^T \left(M_i M_j \langle \mathbf{D}_{ij}^{\text{eff}} \rangle \right)^{-1} \left(\sqrt{\frac{w_j}{w_i}} \vec{\zeta}_i - \sqrt{\frac{w_i}{w_j}} \vec{\zeta}_j \right) \\ &= \frac{1}{2} \sum_{i,j=1}^n \vec{\eta}_{ij}^T \left(M_i M_j \langle \mathbf{D}_{ij}^{\text{eff}} \rangle \right)^{-1} \vec{\eta}_{ij}, \quad \vec{\eta}_{ij} := \left(\sqrt{\frac{w_j}{w_i}} \vec{\zeta}_i - \sqrt{\frac{w_i}{w_j}} \vec{\zeta}_j \right), \end{aligned} \quad (2.36)$$

where the second step follows from the symmetry property $\langle \mathbf{D}_{ij}^{\text{eff}} \rangle = \langle \mathbf{D}_{ji}^{\text{eff}} \rangle$. By hypothesis (P), each of the summands on the right-hand side of (2.36) is non-negative. This shows that

$$\vec{\zeta} : \mathbf{A} \vec{\zeta} \geq 0 \quad \text{for all } \vec{\zeta} \in \mathbb{R}^{d \times n} \quad (2.37)$$

with equality if and only if $\vec{\zeta}_i = w_i \vec{\xi}$ for all $i \in \{1, \dots, n\}$ and some $\vec{\xi} \in \mathbb{R}^d$.

Using (2.35), we thus deduce

$$\int \sum_{i=1}^n \frac{1}{\phi} \nabla \mu_i \cdot \langle \vec{J}_i \rangle = - \int \frac{RT}{c} \sum_{i=1}^n \langle \mathbf{A}(\rho) \langle \vec{J} \rangle \rangle_i \cdot \langle \vec{J}_i \rangle + \int \sum_{i=1}^n \frac{1}{\rho} \nabla p \cdot \langle \vec{J}_i \rangle$$

$$= - \int \frac{RT}{c} \sum_{i=1}^n (\mathbf{A}(\varrho) \langle \vec{J} \rangle)_i \cdot \langle \vec{J}_i \rangle \leq 0,$$

where the second step follows from (2.26) and the last inequality from (2.37). Insertion in (2.34) allows us to conclude

$$\begin{aligned} \frac{d}{dt} F(\varrho) &= -\frac{1}{\eta} \int \mathbf{K} \nabla p \cdot \nabla p - \int \sum_{i=1}^n \frac{RT}{c} (\mathbf{A}(\varrho) \langle \vec{J} \rangle)_i \cdot \langle \vec{J}_i \rangle \\ &\quad + \int \sum_{i=1}^n \mu_i r_i(\varrho) \leq 0, \end{aligned}$$

where each of the three integral terms in the last line has the “correct” sign. For the non-positivity of the term associated with the reactions we rely on the assumption (2.33).

Finally, let us observe that the free energy F is strictly convex. This can easily be seen by differentiating (2.31) with respect to ρ_j , which leads to

$$\frac{\partial^2 f}{\partial \rho_i \partial \rho_j}(\varrho) = \phi \frac{RT}{M_i \rho_i} \delta_{ij}, \quad i, j = 1, \dots, n, \quad \varrho \in (0, \infty)^n.$$

In particular, the Hessian of the free energy density is diagonal with positive entries, and therefore positive definite. Thus, without or under appropriate assumptions on the reaction rates, the steady states of the system, defined as the minimizers of the free energy under the natural constraints associated with the conservation laws, can be expected to be unique.

2.3.2. Effective transport properties in porous media (Darcy scale)

Effective thermal conductivity. As introduced in Section 2.3 an effective thermal conductivity λ^{eff} is required to describe diffusive heat transport in the homogenized model. In general, it is calculated from the thermal conductivities of the non-porous solid λ_s and fluid phases $\lambda_f = \lambda$, the porosity ϕ while considering the influence of the pore structure [34]. In principle, the homogenization approach based on two-scale expansions permits the direct calculation of $\langle \lambda^{\text{eff}} \rangle$ via (2.30). This requires the knowledge of the exact geometry of the porous medium that must be obtained via imaging techniques which will be part of future work.

As an alternative, this work makes use of a recently published calculation approach for the effective thermal conductivity in porous media [35]. This has the advantage that it is easy to implement and does not require detailed knowledge about the pore structure. Briefly, the aim of the approach is to provide a general, structure and geometry independent equation for the effective thermal conductivity of porous media (2.38) and to integrate the geometrical influence via the structure parameter ψ (2.39).

$$\lambda^{\text{eff}} = \frac{\frac{\lambda_f \lambda_s}{\lambda_s \phi + \lambda_f (1-\phi)}}{\frac{\lambda_s}{\lambda_f} \phi + 2\psi + \frac{\lambda_f}{\lambda_s} (1-\phi) + 1} \left[\frac{\lambda_s}{\lambda_f} \phi + (1-\phi) + \psi \right] \left[\phi + \frac{\lambda_f}{\lambda_s} (1-\phi) + \psi \right] \quad (2.38)$$

$$\psi = \frac{1}{k_y} (\phi - 1) \frac{\lambda_s - \lambda_f}{\lambda_s \lambda_f} [\lambda_f (\phi - 1) - \lambda_s \phi] \quad (2.39)$$

For the porous medium used in this study, the structure parameter ψ for an ordered packing of spheres with flattened contacts was chosen and the parameter k_y in (2.39) is the contact angle coefficient as defined in [35]. Different calculation approaches for the effective thermal conductivity as a function of porosity are shown in Fig. 1 and compared to the measured value at room temperature for a sample of the porous support material used within this study. The pure phase thermal conductivities shown as solid black lines correspond to Borosilicate glass (s, solid) [36] and air (f, fluid) at room temperature and amount to $\lambda_s = 1.13 \text{ W(m K)}^{-1}$ and $\lambda_f = 0.026 \text{ W(m K)}^{-1}$ respectively. Fig. 1 shows that the proposed formula by Cheilytko [35] gives values of the effective thermal conductivity of the backfill close to those obtained from the formula derived by Schütz [37].

Effective mass diffusivities. As a result of the homogenization procedure, effective M-S diffusivities $\mathcal{D}_{ij}^{\text{eff}}$ appear in (2.25). As for λ^{eff} , $\mathcal{D}_{ij}^{\text{eff}}$ could be directly calculated via (2.28) which is infeasible due to the unknown pore structure. Instead, a simple tortuosity-constrictivity correction [38] is applied. Here γ is a constriction factor, taking into account the additional drag on diffusing gas molecules through narrow pores and τ is the tortuosity. In the context of a porous medium the tortuosity τ causes both a longer path length as well as a narrower effective pore cross-section for diffusing gas molecules leading to a higher velocity for a given flux. Thus its effect on effective transport properties is quadratic [38]. The effective M-S diffusivities are thus obtained by

$$\mathcal{D}_{ij}^{\text{eff}} = \gamma / \tau^2 \mathcal{D}_{ij}. \quad (2.40)$$

In general γ / τ^2 is found experimentally, while a first approximation can be obtained from $\gamma / \tau^2 = \phi^{1.5}$ [38] which is used throughout this study.

Knudsen diffusivities. In the case of micro-porous structures the flow regime can deviate from continuum flow indicated by the Knudsen number $\text{Kn} = \ell / L$, with ℓ the mean free path length of the gas and L the characteristic length, corresponding to an average pore diameter in the case of porous media. For $\text{Kn} > 1 \times 10^{-2}$ the gas-wall interactions cannot be described by thermodynamic equilibrium assumption and Knudsen diffusion must be considered. The porous material considered in this work [36] is characterized by porosity class 0 with a pore size distribution in the range 160 μm to 250 μm . When considering typical gas phase conditions that apply in the relevant application presented in this work of ca. 600 $^\circ\text{C}$ and 1 bar_a, Knudsen numbers $\text{Kn} \approx 2 \times 10^{-3}$ are obtained which are one order of magnitude below the limit for the continuum flow regime. Therefore, Knudsen diffusion is not considered.

3. Implementation

Both the isothermal model (2.22), (2.24) and the non-isothermal model (2.22), (2.24), (2.29) with their respective boundary conditions comprise a coupled nonlinear system of partial differential equations. For stability reasons, we chose an implicit Euler time discretization. The space discretization is performed using the Voronoi box based finite volume method which we describe here in a cursory way, more on this approach one can find e.g. in [39]. This method starts from a boundary conforming Delaunay triangulation resp. tetrahedralization [40] of the computational

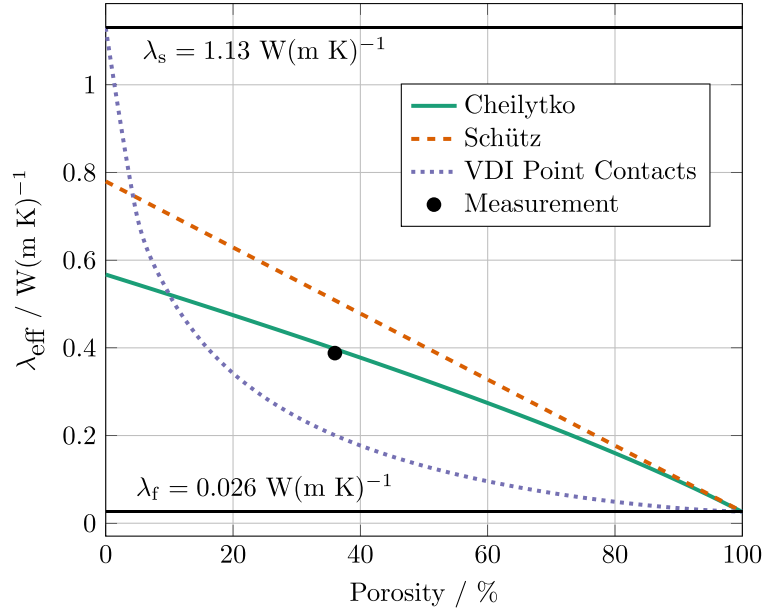


Fig. 1. Comparison of calculation approaches for effective thermal conductivity in porous media, where Cheilytko corresponds to [35], Schütz to [37] and VDI to [34].

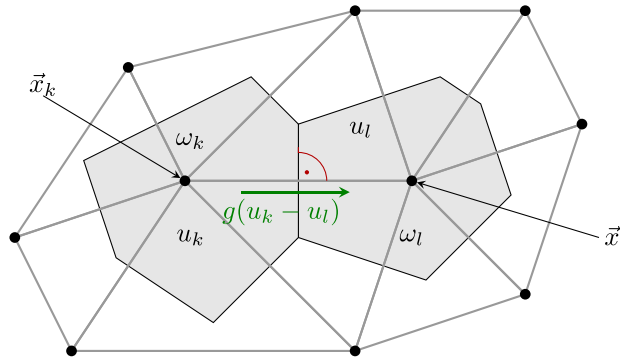


Fig. 2. Two neighboring Voronoi cells and the background triangulation.

domain Ω and constructs its dual, the Voronoi tessellation and intersects it with the computational domain. This results in a subdivision $\bar{\Omega} = \bigcup_{k=1}^K \omega_k$ into K closed convex polygonal control volumes ω_k with collocation points $\vec{x}_k \in \omega_k$ coinciding with the nodes of the initial triangulation. For two neighboring control volumes, the line $\vec{x}_k \vec{x}_l$ of length h_{kl} connecting their respective collocation points is collinear with the normal vector \vec{n}_{kl} to the interface $\sigma_{kl} = \omega_k \cap \omega_l$, thus allowing to approximate the normal derivative of a function u defined on Ω by $\nabla u \cdot \vec{n}_{kl} \approx \frac{u(\vec{x}_k) - u(\vec{x}_l)}{h_{kl}}$ in a consistent manner (see Fig. 2).

Consider a system of N coupled partial differential equations in a d dimensional domain $\Omega \subset \mathbb{R}^d$ and time interval $(0, T)$ written in vector form as

$$\partial_t \mathbf{s}(\mathbf{u}) + \nabla \cdot \vec{\mathbf{j}}(\mathbf{u}, \vec{\nabla} \mathbf{u}) + \mathbf{r}(\mathbf{u}) = 0, \quad (3.1)$$

where $\mathbf{u}(\vec{x}, t) = (u_1(\vec{x}, t) \dots u_N(\vec{x}, t)) : \Omega \times (0, T) \rightarrow \mathbb{R}^N$ is the basic unknown, $\mathbf{s} : \mathbb{R}^N \rightarrow \mathbb{R}^N$ is the local amount of species, $\mathbf{r} : \mathbb{R}^N \rightarrow \mathbb{R}^N$ is the reaction term, and $\vec{\mathbf{j}} : \mathbb{R}^N \times \mathbb{R}^{Nd} \rightarrow \mathbb{R}^{Nd}$ is the species flux.

Integration of (3.1) over a space-time control volume $\omega_k \subset \bar{\Omega}$, $[t^{m-1}, t^m] \in [0, T]$, m being the time-step index, applying Newton-Leibniz rule and Gauss' law yields the identity

$$\begin{aligned} & \int_{\omega_k} \mathbf{s}(\mathbf{u}(\vec{x}, t^m)) d\vec{x} - \int_{\omega_k} \mathbf{s}(\mathbf{u}(\vec{x}, t^{m-1})) d\vec{x} + \\ & + \int_{t^{m-1}}^{t^m} \left(\int_{\partial \omega_k} \vec{\mathbf{j}} \cdot \vec{\mathbf{n}} ds + \int_{\omega_k} \mathbf{r}(\mathbf{u}) d\vec{x} \right) dt = 0 \end{aligned}$$

which is approximated by

$$\begin{aligned} & |\omega_k| (\mathbf{s}(\mathbf{u}_k^m) - \mathbf{s}(\mathbf{u}_k^{m-1})) + \\ & + (t^m - t^{m-1}) \left(\sum_{\omega_l \text{ neighbor of } \omega_k} \frac{|\sigma_{kl}|}{h_{kl}} \mathbf{g}(\mathbf{u}_k^m, \mathbf{u}_l^m) + |\omega_k| \mathbf{r}(\mathbf{u}_k^m) \right) = 0 \end{aligned} \quad (3.2)$$

As we see, the functions s and r directly enter the discrete description; the same is true for nonlinear terms characterizing Robin boundary conditions, which we omit here for brevity. The vector valued flux function $\mathbf{g}(\mathbf{u}_k, \mathbf{u}_l) \approx h_{kl} \vec{\mathbf{j}} \cdot \vec{\mathbf{n}}_{kl}$ approximates the nonlinearly coupled continuous fluxes.

With properly chosen flux terms, this finite volume approach has the potential to provide a discrete thermodynamic structure, see e.g. [41,42]. For the present model, a pragmatic approach is presented. The refinement of the discretization scheme as well as the investigation of discrete entropy principles are possible directions of further work.

Considering that the basic unknowns are $\mathbf{u} = (x_1, \dots, x_n, p, T)$, the flux function \mathbf{g} can be written as $\mathbf{g}(\mathbf{u}_k, \mathbf{u}_l) = (g_{kl}^\rho, g_{kl}^{\rho_1} \dots g_{kl}^{\rho_{n-1}}, g_{kl}^h)$ and $\bar{\mathbf{u}}_{kl} = (\mathbf{u}_k + \mathbf{u}_l)/2$. Given the Darcy velocity approximation

$$v_{kl} = (K/\eta) (\bar{\mathbf{u}}_{kl}) (p_k - p_l),$$

the components are:

- the total mass flux g_{kl}^ρ :

$$g_{kl}^\rho = \rho (\bar{\mathbf{u}}_{kl}) v_{kl}$$

- the species mass fluxes $g_{kl}^{\rho_i}$:

$$g_{kl}^{\rho_i} = J_{kl}^i + \rho^i (\bar{\mathbf{u}}_{kl}) v_{kl}, \quad i = 1, \dots, n-1,$$

where the calculation of the diffusive species mass fluxes J_{kl}^i corresponding to \vec{J}_i in (2.7) requires the solution of a $(n-1) \times (n-1)$ linear system [43,44]:

$$\begin{aligned} -\mathbf{H}_{kl} \mathbf{J}_{kl} &= \mathbf{F}_{kl} \\ F_{kl}^i &= (x_k^i - x_l^i) + D_p^i (\bar{\mathbf{u}}_{kl}) \left(\frac{p_k - p_l}{(p_k + p_l)/2} \right) \\ &\quad + \text{So}^i (\bar{\mathbf{u}}_{kl}) \left(\frac{T_k - T_l}{(T_k + T_l)/2} \right), \quad i = 1, \dots, n-1, \\ H_{kl}^{ii} &= \frac{w^i}{M^i M^n \mathfrak{D}^{in}} + \sum_{\substack{o=1 \\ o \neq i}}^n \frac{w^o}{M^i M^o \mathfrak{D}^{io}}, \quad i = 1, \dots, n-1, \\ H_{kl}^{ij} &= -w^i \left(\frac{1}{M^i M^j \mathfrak{D}^{ij}} - \frac{1}{M^i M^n \mathfrak{D}^{in}} \right), \quad (i, j) = 1, \dots, n-1, i \neq j, \end{aligned}$$

where D_p^i are the pressure-diffusion coefficients corresponding to $x_i - w_i$ in (2.11), So^i are the Soret thermal diffusion coefficients corresponding to $x_i \tilde{\chi}_i$ in (2.11),

- the enthalpy flux g_{kl}^h :

$$g_{kl}^h = \lambda_{\text{eff}} (\bar{\mathbf{u}}_{kl}) (T_k - T_l) + \sum_{i=1}^n h^i (\bar{\mathbf{u}}_{kl}) g_{kl}^i + \text{Du}^i (\bar{\mathbf{u}}_{kl}) J_{kl}^i$$

where Du^i are the Dufour coefficients corresponding to $RT \tilde{\chi}_i / M_i$ in (2.13).

Omitting further details, we just state that (3.2) leads to a nonlinear system of $K \cdot N$ equations which needs to be solved in each time step. This is achieved by Newton's iterative method, which requires the calculation of the Jacobi matrix of partial derivatives with respect to the current iterate and the solution of the resulting sparse linear system for the iteration updates.

The possibility to characterize the discretized problem by the flux, reaction, storage and boundary functions and the one, two- or three-dimensional discretization grid leads to a convenient software API which has been realized in the Julia package `VoronoiFVM.jl` [12]. This package leverages forward mode automatic differentiation [45] to calculate the partial derivatives of the constitutive functions for the subsequent assembly of the Jacobi matrices. It can use various direct and iterative solvers for sparse linear systems; the calculations presented in this paper used a GMRES iterative solver [46] with an equation-wise block diagonal preconditioner built from sparse LU factorizations performed with `oneMKL PARDISO` [47] for the 3D example in Section 4.1 and the `Sparspak.jl` direct solver [48] for the 2D example in Section 4.2.

4. Simulations

4.1. Photo-thermal catalytic reactor

The model is applied to a directly irradiated PTR that was experimentally investigated by the authors [49] of which a schematic cross-section is illustrated in Fig. 3. As was noted in Section 2.2.2, Soret and Dufour cross-diffusion effects were not considered in this simulation. The reactor consists of an upper and lower chamber separated by a porous support, a sintered structure of Borosilicate glass [36]. The upper chamber is bounded by the quartz glass window from above and by the porous support from below. The gaseous reactants enter the upper chamber from the side. Irradiation enters the reactor via the quartz window and hits the photo-thermal catalyst that is deposited on top of the porous support. The bottom chamber is bounded by the porous support and a bottom plate. The modeling domain of the PTR is a three-dimensional, square prismatic geometry of 16 cm side length and a height of 0.5 cm. The domain consists of the catalyst layer of 0.5 mm thickness and supporting porous structure as indicated in Fig. 3 and in more detail with information on domain boundaries in Fig. D.11.

4.1.1. Boundary conditions

The simulation should reflect the boundary conditions of the physical experiment. In the experimental setup the total mass flow as well as the species mass flows into the reactor were controlled via mass flow controllers upstream of the reactor. The pressure at the outlet can be regulated via

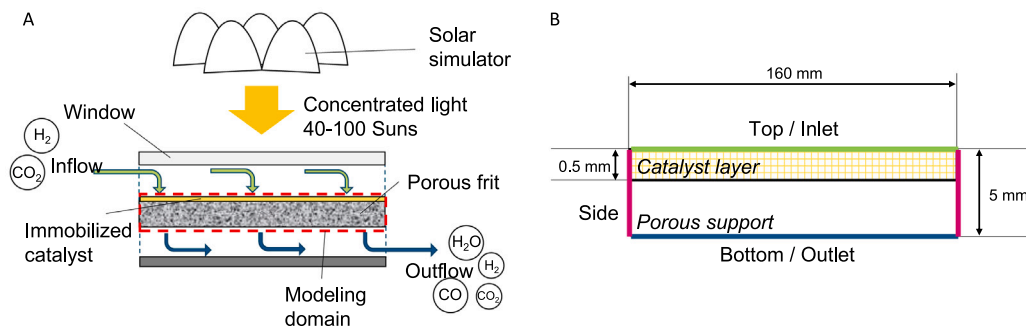


Fig. 3. (A) Schematic cross-section of the photo-thermal reactor with in- and outflows and (B) cross-section of square prismatic modeling domain with internal regions (italic font) and outer boundaries with geometric dimensions.

Table 1
Boundary conditions for the simulation of the photo-thermal catalytic reactor.

Boundary	Transport process		
	Total mass	Species mass ($i = 1, \dots, n$)	Thermal energy
Top/Inlet	$\rho \vec{v} \cdot \vec{n} = [\Psi^\rho]_{r_{in}}$	$(\vec{J}_i + \rho_i \vec{v}) \cdot \vec{n} = [\Psi^{\rho_i}]_{r_{in}}$	Inflow (4.3), Appendix B
Side	$\vec{v} \cdot \vec{n} = 0$	$(\vec{J}_i + \rho_i \vec{v}) \cdot \vec{n} = 0$	Appendix C
Bottom/Outlet	$p = p_{out}$	Outflow (4.1)	Outflow (4.2), Appendix B

back pressure regulator downstream of the reactor [49]. The corresponding boundary conditions applied in the simulation are summarized in Table 1 where $[\Psi^\rho]_{r_{in}}$ and $[\Psi^{\rho_i}]_{r_{in}}$ correspond to the specified total and species mass fluxes at the inlet, respectively. To simplify notation throughout this section, the averaged volume and diffusive species mass fluxes $\langle \vec{v} \rangle$ and $\langle \vec{J}_i \rangle$ are written as \bar{v} and \bar{J}_i as in the context of the effective medium equations all fluxes are averaged fluxes and there is no danger of confusing the notations.

A merit of the explicit calculation of the convective velocity field via (2.22) is the high degree of control over the convective flux over the boundaries: as can be seen in Fig. D.11 the outermost part of the inlet boundary is not permeable for gas flow reflecting the construction of the physical reactor. For these parts of the boundary the total mass flux and thus the normal convective flow velocity vanishes.

Regarding the boundary condition for species transport at the outlet, the gas phase composition at the outlet is not known beforehand but instead is a result of the chemical reactions occurring in the catalyst layer. Thus, for the species transport, an outflow boundary condition is specified at the outlet. In particular, the normal species mass flux through the outlet boundary from convective flow with its velocity field computed with (2.22) as described in Eq. (4.1):

$$\vec{n} \cdot (\langle \vec{J}_i \rangle + \rho_i \langle \vec{v} \rangle) = [\vec{n} \cdot (\rho_i \langle \vec{v} \rangle)]_{r_{out}} \quad (4.1)$$

Analogously, the outlet heat flux where the product gas mixture exits the modeling domain is given by

$$\vec{n} \cdot (c \rho T \langle \vec{v} \rangle - \lambda_{eff} \nabla T) = [\vec{n} \cdot (c \rho T \langle \vec{v} \rangle)]_{r_{out}} + [\Psi^{T,rad}]_{r_{out}} \quad (4.2)$$

where all quantities c , ρ , $\langle \vec{v} \rangle$ are taken at outlet conditions and where $[\Psi^{T,rad}]_{r_{out}}$ is a radiative heat flux term originating from irradiation exchange described in Appendix B.

At the inlet boundary the normal enthalpy flux is specified via a Neumann boundary condition as:

$$\vec{n} \cdot (c \rho T \langle \vec{v} \rangle - \lambda_{eff} \nabla T) = [\Psi^T]_{r_{in}} \quad (4.3)$$

where the total heat flux specified at the inlet $[\Psi^T]_{r_{in}}$ is the sum of the convective and radiative heat fluxes $[\Psi^{T,conv} + \Psi^{T,rad}]_{r_{in}}$, respectively, defined as

$$[\Psi^{T,conv}]_{r_{in}} = [c T \Psi^\rho]_{r_{in}} \quad (4.4)$$

and $[\Psi^{T,rad}]_{r_{in}}$ defined as shown in Appendix B.

The irradiation boundary condition for the thermal energy equation at the inlet of the photo-thermal catalytic reactor is defined by the grid interpolated irradiation flux density profile shown in Fig. 4: Irradiation enters the reactor via the 12 cm × 12 cm window (thick line in Fig. 4) at a nominal flux density of 70 kW/m² corresponding to the average value for the 10 cm × 10 cm core area (thin line in Fig. 4).

4.1.2. Chemical conversion

The aim of the photo-thermal catalytic reactor is the conversion of CO₂ with H₂ to CO and the side product H₂O via the endothermic rWGS reaction (4.5), effectively storing the solar energy provided by the irradiation in the chemical bonds of the products. Since both CO₂ and H₂ are present in the feed stream, the methanation reaction of CO₂ (Sabatier reaction) as well as the further methanation of the in-situ formed CO could also occur as unintended side reactions:



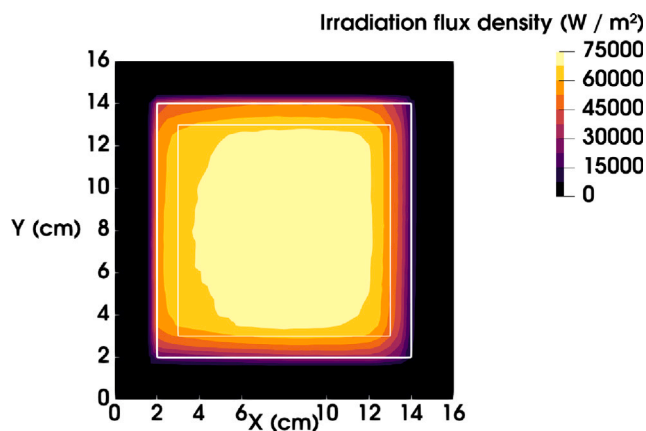


Fig. 4. Grid interpolated irradiation flux density profile corresponding to a nominal flux density of 70 kW/m^2 in the $10\text{ cm} \times 10\text{ cm}$ core area from flux measurements in [49]. It is used as input to the boundary condition for thermal energy transport (B.1) at the inlet boundary of the photo-thermal catalytic reactor.



In the photo-thermal reactor chemical conversion of reactants into products occurs through heterogeneous catalytic reactions between the gas phase and the solid immobilized catalyst that is deposited in the catalyst layer (Fig. 3 B). In accordance with the quasi-homogeneous approach, the catalyst is not treated as a separate phase but instead is assumed to be dispersed evenly inside the porous structure and is quantified via the volumetric catalyst mass loading. Chemical conversion in the reactor is expressed mathematically via rates of reaction as functions of the local conditions of temperature, total pressure and chemical composition that after applying the corresponding stoichiometric factors result in the species source terms in (2.24). Based on the assumption that the catalyst activity is determined by the temperature, the kinetics of the photo-thermal catalyst can be treated like ordinary thermal catalysts [50] with reaction rate equations for the rWGS and methanation reactions from [51].

4.1.3. Results and discussion

The most important operating conditions for the PTR are the irradiation flux density, the feed gas flow and feed chemical composition. In the following the PTR is simulated with a nominal irradiation flux density of 70 kW/m^2 where the corresponding flux density distribution used as model input is shown in Fig. 4. A total feed gas flow of $3\text{ L}_s/\text{min}$ ($p_s = 1.01325\text{ bar}_a$, $T_s = 293.15\text{ K}$) with molar composition of $\text{H}_2/\text{CO}_2 = 1/1$ and a total catalyst mass loading of 500 mg are applied. This corresponds to the nominal operating point as defined in [49]. The optical properties of the catalyst layer and surrounding surfaces describe the radiation heat transport and consequently have a large impact on the temperature distribution in the reactor which in turn strongly influences the chemical conversion. Typical values for the optical properties that are used for the simulation were obtained in [49] and are shown in Table B.2. The computational domain corresponds to the catalyst layer and porous support structure with dimensions of $16\text{ cm} \times 16\text{ cm} \times 0.5\text{ cm}$ shown in Fig. D.11. The domain was discretized on a uniform, Cartesian grid with 33 grid points in the X and Y dimensions and 21 grid points in the Z dimension, leading to grid edge lengths of 5 mm and 0.25 mm , respectively.

For these conditions the simulation completed in 17 min on a laptop computer with Intel® i7-1365U CPU. Selected simulation results for stationary operation are shown in Fig. 5. The simulation code for this numerical example together with instructions on how to reproduce Fig. 5 is available online [52]. A maximum temperature of $610\text{ }^\circ\text{C}$ is reached on the top surface in the center of the domain while the underside of the domain in the central region is at ca. $500\text{ }^\circ\text{C}$. The temperature drops rapidly towards the outer edges to values below $200\text{ }^\circ\text{C}$ with the minimum reached in the corners at ca. $110\text{ }^\circ\text{C}$.

Regarding the pressure field it is mentioned in Section 4.1.1 and illustrated in Fig. D.11 that parts of the inlet and outlet boundaries are impermeable for gas flow. This explains the regions of constant pressure at the outer rim of the domain. In the permeable central region a pressure drop of ca. 12 Pa is observed for the given combination of feed flow and porous medium. This low value is a likely result of the large pore size of ca. $200\text{ }\mu\text{m}$ (porosity class 0) and the corresponding high permeability [28].

With respect to the chemical conversion towards the target product CO, the maximum molar fraction of ca. 16% is observed in the center corresponding to the region of highest temperature as the thermochemical equilibrium favors the endothermic rWGS reaction at increasingly high temperatures [53]. The maximum is not located on the domain surface but in the interior of the catalyst region. The CO molar fraction quickly drops towards the outer edges while a CO molar fraction of ca. 10% is maintained in a core area of $10\text{ cm} \times 10\text{ cm}$.

The molar fraction of the undesired side product CH_4 shows an interesting spatial distribution where in contrast to CO the region of maximal CH_4 at 3.5% does not lie in the center but instead forms a ring around it corresponding to the intermediate temperature range of ca. $400\text{ }^\circ\text{C}$ to $500\text{ }^\circ\text{C}$ where the thermochemical equilibrium shifts towards the exothermic Sabatier reaction. For regions with temperatures below ca. $350\text{ }^\circ\text{C}$ the CH_4 molar fraction drops quickly as the reaction rates become kinetically limited.

Summarizing, for the stated operating conditions of $3\text{ L}_s/\text{min}$ of $\text{H}_2/\text{CO}_2 = 1/1$ feed flow corresponding to a total molar flow 7.4 mol/h , molar outflows of CO and CH_4 of 0.55 mol/h and 0.13 mol/h respectively, are obtained. This results in a CO_2 based conversion of 18% (29% H_2 based) and a selectivity towards CO of 81% with the remaining 19% towards CH_4 when based on CO_2 .

The simulation conditions were chosen in accordance with a set of experimental operating conditions reported in [49] allowing for a comparison of simulated and experimental results. The temperature on the surface of the catalyst layer will be compared as shown in Fig. 6 where the placement of the thermocouples is shown alongside a parity plot of experimental and calculated results. Therein the data points labeled “TC” correspond to the

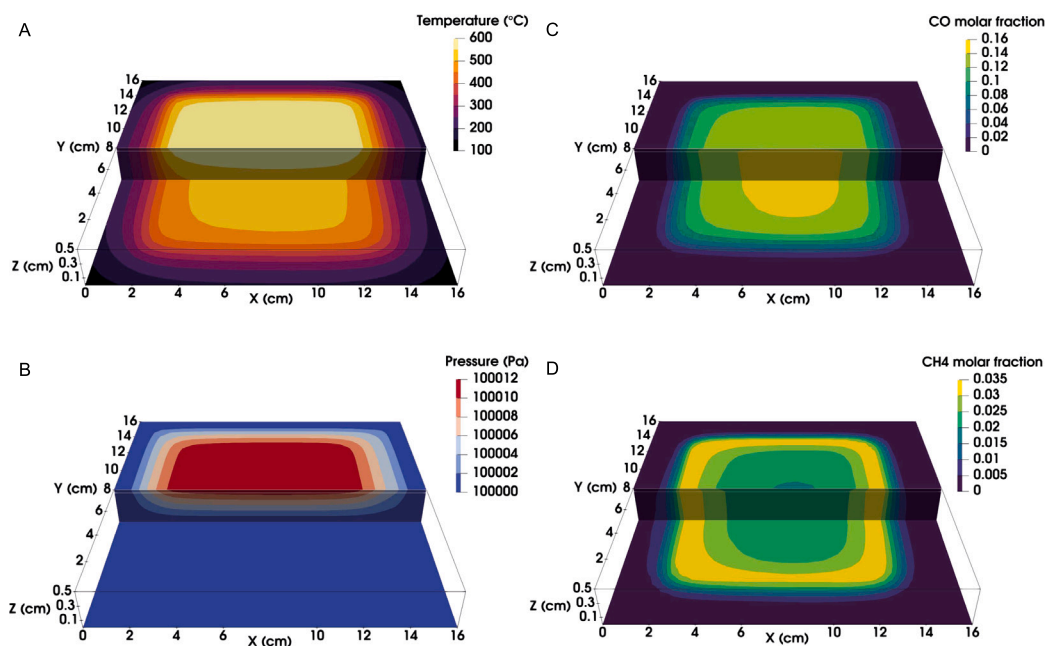


Fig. 5. Combined top- and cross-section views of stationary simulation results of photo-thermal catalytic reactor operated at a nominal irradiation flux density of 70 kW/m^2 and feed flow of $3 \text{ L}_s/\text{min}$ of $\text{H}_2/\text{CO}_2 = 1/1$: (A) temperature, (B) total pressure, (C) molar fraction of CO, (D) molar fraction of CH_4 . The catalyst layer region is outlined by a thin white line, the aspect ratio is increased in the Z-axis by a factor of 4 to increase readability.

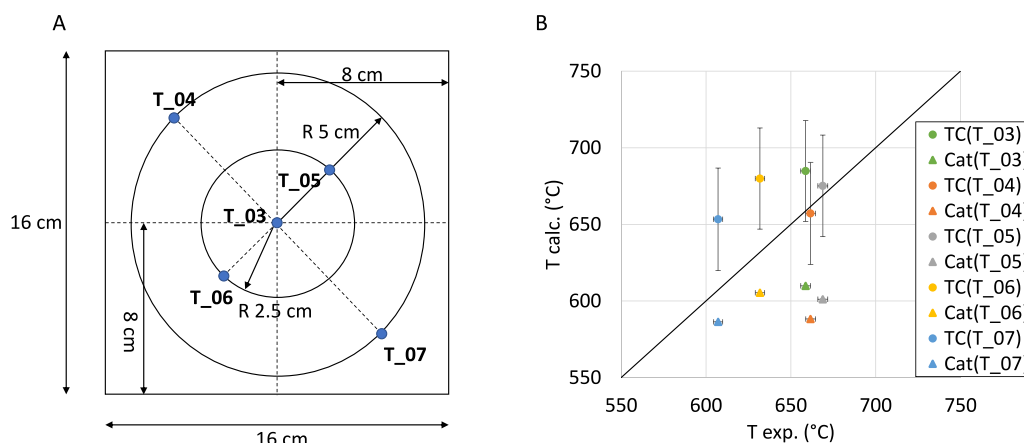


Fig. 6. Comparison of experimental and simulated results for temperature with (A) measurement positions for temperature on top of the catalyst layer in the experimental reactor and (B) parity plot of calculated thermocouple (TC) and catalyst surface (Cat) temperatures including error bars.

calculated thermocouple temperatures following the procedure outlined in [49] and the data points labeled “Cat” correspond to simulation results obtained with the model presented in this work. One complication arises, when attempting to compare the results because in the experimental setup it is difficult to measure the actual temperature of the catalyst layer. As is discussed in [49], the thermocouples are directly irradiated and will consequently overestimate the catalyst layer temperature. This becomes evident by the fact that the data points corresponding to simulation results (“Cat”) all lie under the line through the origin. Thus, a procedure was derived in [49] to account for this effect by recalculating the thermocouple temperatures under irradiation based on the catalyst temperature and further model parameters. This results in the data points labeled “TC” with respective uncertainty indicators that originate from uncertain model parameters and that correspond to standard uncertainty. The experimental temperature values are associated with a standard uncertainty of 0.75% in the relevant temperature range. It can be seen that for the measurement positions T₀₃, T₀₄ and T₀₅ the calculated and experimental thermocouple temperatures agree within the margin of uncertainty, while for the remaining measurement points there is an overprediction. Overall, given the large number of model parameters which cannot be determined with certainty the agreement can be considered as good. Nevertheless, further improvement in this direction is expected from performing a sensitivity analysis of the model presented in this work with respect to the model parameters which is planned in the future.

Regarding improvement options to maximize the yield of CO it is apparent that the outer, cold regions comprise a significant part of the domain where no chemical conversion occurs. As an optimization measure it is thus suggested to block the outer regions and leave accessible for gas flow a core area of $10 \text{ cm} \times 10 \text{ cm}$ so that the gas flow is forced through the hot center. At the same time this measure might reduce the rate of CH_4 formation by limiting the available catalytically active area in the intermediate temperature range. In addition, an updated version of the PTR

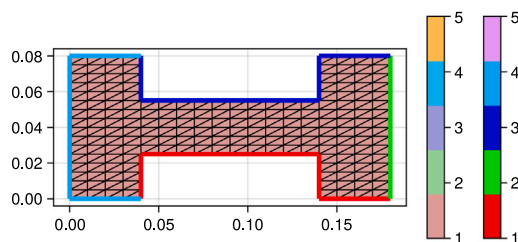


Fig. 7. Two-dimensional modeling domain of a separation chamber used in [13] to simulate the Soret effect through temperature induced gas separation in a ternary mixture of noble gases. Spatial coordinates in m.

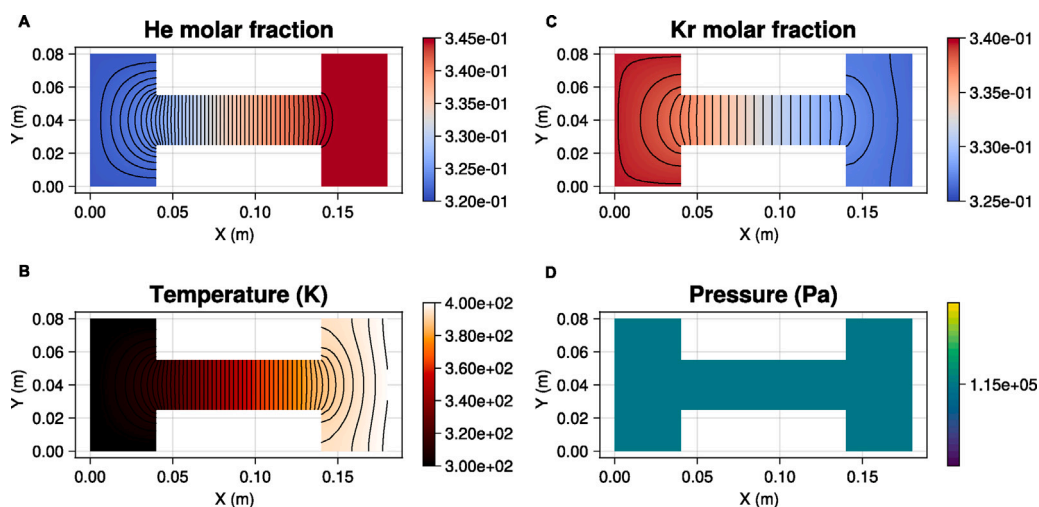


Fig. 8. Simulation results obtained with the model presented in this work for (A) He molar fraction, (B) temperature, (C) Kr molar fraction and (D) pressure to compare against the results from [13] to demonstrate the Soret effect through temperature induced gas separation in a ternary mixture of noble gases.

could comprise a catalyst layer of increased thickness from the current value of ca. 500 μm as the temperature in the core area is greater than 550 $^{\circ}\text{C}$ for more than half of the total thickness of the porous structure of 5 mm. This holds the potential to further increase CO formation under the condition that a sufficiently high, homogeneous temperature field prevails in the reactive zone.

4.2. Thermodiffusion

To demonstrate the model and numerical method with respect to thermodiffusion induced by Dufour and Soret cross diffusion effects as described in (2.10), the separation of an equimolar ternary gas mixture of Helium, Argon and Krypton driven by a temperature gradient as presented in [13] is reproduced. The two-dimensional modeling domain corresponding to the separation chamber of 18 cm total length consisting of two chambers of 8 cm height and 2 cm width that are connected by a pipe of 3 cm height and 10 cm length is shown in Fig. 7. All boundaries are impermeable for gas species transport. With respect to heat transport the boundaries labeled 1 and 3 are insulating while the temperature is fixed at boundary 4 at 300 K and an appropriate heat flux through boundary 2 specified such that a temperature of ca. 400 K is obtained at that boundary [13]. The initial state is characterized by a uniform temperature of 300 K and a uniform, equimolar mixture composition at a pressure of 1 bar_a. The stationary state that established upon application the heat flux is shown in Fig. 5 where a temperature difference of ca. 100 K is observed over the length of the domain with a separation for helium defined by $(x_{\text{He,max}}^{\text{after}} - x_{\text{He,min}}^{\text{after}}) / x_{\text{He}}^{\text{before}}$ of 7.5% is induced by the temperature difference at a uniform pressure of 1.15 bar_a in agreement with results obtained in [13]. The simulation code for this numerical example reproducing Fig. 8 can be run in the computational notebook ‘Thermodiffusion.jl’ from [52].

5. Summary and outlook

A modeling approach for multi-component heat and mass transport of reactive gas mixtures in porous media was developed motivated by the desire to accurately reflect boundary conditions prevalent in the experimental setting of continuous-flow chemical reactors involving porous media. Analysis of the model structure based on the approach of the minimization of free energy revealed thermodynamic consistency of the isothermal model equations.

Further, starting from pore scale equations for gas and rigid solid phases, effective medium equations for the porous medium were derived via the homogenization method with two-scale asymptotic expansions. Effective transport parameters are introduced that take into account the presence of the porous medium on the flow, transport of species mass and thermal energy. In this context a recently presented equation for the effective thermal conductivity was implemented and compared with existing correlations. The model implementation which is based on the Finite volume discretization and open-source software is then applied to a photo-thermal catalytic reactor PTR that was previously investigated experimentally. Simulation results are discussed and compared with experimentally observed results. Qualitative agreement with experimental

temperature measurements is achieved which must be seen in the light of the large number of model parameters that are subject to varying degrees of uncertainty and that influence the simulation results. Despite this, the developed model in combination with the numerical implementation is a very valuable tool in guiding reactor development as it gives insights that are difficult to obtain via measurements and allows deriving optimization measures. Specifically, in order to maximize the CO productivity from the investigated PTR the catalyst placement in the porous domain should correspond to the regions of homogeneously high temperatures while no catalyst should be deposited in colder regions to prevent back or side reactions. Further, the gas flow path can be optimized such that the gas flow is restricted to regions of high temperatures by blocking the pores of colder regions of the domain. Generally, the implementation based on open-source code is accessible and permits the adaptation of the modeling framework to other applications as is demonstrated via the thermodiffusion problem of a ternary gas mixture where good agreement is achieved with published literature. Finally, the implementation of the Finite Volume discretization and solution algorithm including the possibility to choose the linear system solver permits simulation of three-dimensional geometries on a personal computer in reasonable time.

With respect to future work, symmetry assumptions on the pore structure will be dropped, and effective transport parameters will be obtained based on the actual pore structure following from homogenization. Further, the numerical analysis of the convergence and thermodynamic properties of the finite volume scheme could be investigated. Impact of uncertain model parameters on the simulation could be better understood via a sensitivity analysis with respect to model parameters where a focus would be placed on the optical parameters governing the light interaction of the irradiated surfaces as radiation is the dominant mode of heat transfer in the investigated application. Alongside, the model could be further validated by comparison with experiments at varying operating conditions.

Symbols

Roman

c	Molar density of gas phase
c_i	Molar density of gas species i
$c_{p,i}$	Mass specific isobaric heat capacity of gas species i
c_p	Mass specific isobaric heat capacity of gas mixture
c_s	Heat capacity of solid phase
d_p	Mean pore size
\bar{d}_i	Diffusive driving force (isothermal) of gas species i
\bar{d}'_i	Adjusted diffusive driving force (non-isothermal) of gas species i
\mathcal{D}_{ij}	Maxwell–Stefan diffusivities of gas phase species i, j
$\mathcal{D}_{ij}^{\text{eff}}$	Effective Maxwell–Stefan diffusivities
D_i^T	Barycentric coefficients of thermal diffusion of gas species i
e	Mass specific internal energy of gas phase
h	Mass specific enthalpy of gas phase
h_i	Mass specific enthalpy of gas species i
h_i^{th}	Mass specific thermal enthalpy of gas species i
h_i^0	Mass specific enthalpy of formation of gas species i
\vec{J}_i	Diffusive mass flux of gas species i
\mathbf{K}	Permeability tensor
M_i	Molar mass of gas species i
M_{mix}	Molar mass of gas mixture
p	Pressure
q	Heat source term from gas phase chemical reactions
\vec{Q}	Heat flux vector in gas phase
r_i	Formation rate from chemical reactions of gas species i
R	Ideal gas constant
t	Time
T	Temperature
\vec{v}	Mass-averaged gas phase velocity
w_i	Mass fraction of gas species i
x_i	Molar fraction of gas species i
$\bar{\mathcal{X}}_i$	Rescaled thermal diffusion ratio of gas species i

Greek

η	Dynamic viscosity of gas phase mixture
λ	Thermal conductivity of gas phase mixture
λ_f	Thermal conductivity of fluid phase
λ_s	Thermal conductivity of solid phase
λ^{eff}	Effective thermal conductivity tensor
ρ	Mass density of gas phase
ρ_i	Mass density of gas species i
ρ_s	Mass density of solid phase
ϕ	Porosity of porous medium

Ψ^ρ	boundary total gas phase mass flux
Ψ^{ρ_i}	boundary mass flux of gas species i
Ψ^T	boundary heat flux
Ω	Representative elementary volume of the porous medium
Operator	
$\langle \cdot \rangle$	Volumetric averaging operator
Acronyms	
M-S	Maxwell–Stefan
DGM	Dusty Gas Model
MTPM	Mean Transport Pore Model
BTM	Binary Transport Model
CFD	Computational fluid dynamics
PTR	Photo-thermal catalytic reactor
LBM	Lattice Boltzmann Method

CRedit authorship contribution statement

David Brust: Writing – original draft, Visualization, Software, Methodology, Investigation. **Katharina Hopf:** Writing – original draft, Methodology, Formal analysis. **Jürgen Fuhrmann:** Writing – original draft, Visualization, Software, Methodology. **Andrii Cheilytko:** Writing – review & editing, Writing – original draft. **Michael Wullenkord:** Writing – review & editing, Supervision, Resources, Project administration, Methodology, Funding acquisition. **Christian Sattler:** Writing – review & editing, Supervision, Resources.

Declaration of competing interest

The authors declare that they have no known competing financial interests or personal relationships that could have appeared to influence the work reported in this paper.

Acknowledgments

D.B. and M.W. acknowledge funding from the European Union’s Horizon 2020 research and innovation programme under grant agreement No 862453 (FlowPhotoChem). The material presented and views expressed here are the responsibility of the authors only. The EU Commission takes no responsibility for any use made of the information set out.

Appendix A. Alternative formulation of enthalpy balance

In the following it is shown how to obtain the “separated formulation” of enthalpy balance equation from the formulation based on the absolute enthalpy of the gas phase mixture. The absolute gas species enthalpy h_i consists of the contributions via the reference enthalpy h_i^0 (“formation enthalpy” at reference conditions, typically 298.15 K, 1 bar) and thermal enthalpy $h_i^{\text{th}}(T)$ due to the species temperature deviating from the reference temperature:

$$\begin{aligned} h_i &= h_i^0 + \int_{T_{\text{ref}}}^T c_{p,i}(\tilde{T}) d\tilde{T} \\ &= h_i^0 + h_i^{\text{th}}(T) \end{aligned} \quad (\text{A.1})$$

The species reference enthalpies (enthalpies of formation) must be considered when species transformations through chemical reactions occur. The difference in reference enthalpies between reactant and product species makes up the enthalpy of reaction.

Starting from the enthalpy equation in terms of absolute enthalpy (2.14) we first use $\rho h = \sum_{i=1}^n \rho_i h_i$ and (A.1):

$$\begin{aligned} \frac{\partial(\sum \rho_i h_i^0)}{\partial t} + \frac{\partial(\sum \rho_i h_i^{\text{th}}(T))}{\partial t} + \nabla \cdot (\sum \rho_i h_i^0 \vec{v}) + \nabla \cdot (\sum \rho_i h_i^{\text{th}}(T) \vec{v}) \\ + \nabla \cdot (\sum h_i^0 \vec{J}_i) + \nabla \cdot (\sum h_i^{\text{th}}(T) \vec{J}_i) + \nabla \cdot \vec{Q} - \frac{\partial p}{\partial t} = 0 \end{aligned} \quad (\text{A.2})$$

For the remainder of the derivation in Appendix A we have:

$$\vec{Q} = -\lambda \nabla T + \sum_{i=1}^n \left(RT \tilde{\chi}_i / M_i \right) \vec{J}_i$$

We can group the terms belonging to the reference and thermal enthalpies, respectively:

$$\begin{aligned} \sum \left(\frac{\partial(\rho_i h_i^0)}{\partial t} + \nabla \cdot (\rho_i h_i^0 \vec{v}) + \nabla \cdot (h_i^0 \vec{J}_i) \right) \\ + \frac{\partial(\sum \rho_i h_i^{\text{th}}(T))}{\partial t} + \nabla \cdot (\sum \rho_i h_i^{\text{th}}(T) \vec{v}) + \nabla \cdot (\sum h_i^{\text{th}}(T) \vec{J}_i) + \nabla \cdot \vec{Q} - \frac{\partial p}{\partial t} = 0 \end{aligned} \quad (\text{A.3})$$

Consider the gas phase species mass balance (2.3) and multiply by the reference enthalpy for each species $i = 1 \dots n$:

$$h_i^0 \frac{\partial \rho_i}{\partial t} + h_i^0 (\nabla \cdot (\rho_i \vec{v})) + h_i^0 (\nabla \cdot \vec{J}_i) = h_i^0 r_i \quad (\text{A.4})$$

The reference enthalpy is defined at a reference temperature T_{ref} , so $h_i^0 = h_i^0(T_{\text{ref}})$ are constant:

$$\frac{\partial(\rho_i h_i^0)}{\partial t} + \nabla \cdot (\rho_i h_i^0 \vec{v}) + \nabla \cdot (h_i^0 \vec{J}_i) = h_i^0 r_i \quad (\text{A.5})$$

Table B.2

Effective values of optical surface properties for the visible (vis) and infra-red (IR) spectral ranges as defined in Appendix B for the surfaces participating in radiative energy exchange in the reactor photo-thermal reactor.

	Quartz window (1)		Catalyst layer (2)		Porous support (3)		Reactor wall (4)	
	vis	IR	vis	IR	vis	IR	vis	IR
τ	0.93	0.33	0	0	0	0	–	0
α	0	0.67 ^a	0.39	0.56 ^a	0.15	0.55 ^a	–	0.8 ^a
ρ	0.07	0	0.61	0.44	0.85	0.45	–	0.2

^a $\alpha^{\text{IR}} = \epsilon$ for the respective surfaces.

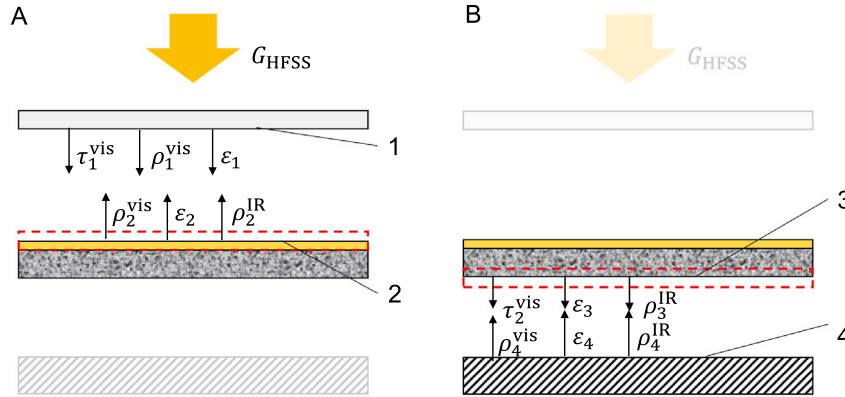


Fig. B.9. Schematic cross-section of photo-thermal reactor illustrating the radiative energy exchange among the surfaces in (A) the upper chamber and (B) the lower chamber.

Summing (A.5) over all gas phase species $i = 1 \dots n$ and inserting into (A.3) yields the “separated” form of the enthalpy equation in the gas phase:

$$\begin{aligned} & \frac{\partial(\sum_{i=1}^n \rho_i h_i^{\text{th}}(T))}{\partial t} + \nabla \cdot \left(\sum_{i=1}^n \rho_i h_i^{\text{th}}(T) \vec{v} \right) + \nabla \cdot \left(\sum_{i=1}^n h_i^{\text{th}}(T) \vec{J}_i \right) \\ & + \nabla \cdot \vec{Q} + \sum_{i=1}^n h_i^0 r_i - \frac{\partial p}{\partial t} = 0 \end{aligned} \quad (\text{A.6})$$

Appendix B. Radiation heat transport

In this work radiation heat transport is treated in a simplified manner by geometrical optics while assuming, that the radiation exchange processes can be described as surface phenomena on the solid surfaces. To this end the optical parameters transmittance τ , absorptance α and reflectance ρ of the participating surfaces are introduced, measuring the ratio of transmitted, absorbed and reflected light radiation intensity to incident light radiation intensity at a specified wavelength [54], respectively. As a simplification, effective values for the optical properties are introduced within this work: the light intensity spectrum of the Xe-short arc lamps used as the artificial light source emulating the sun to operate the photo-thermal reactor is applied as a weighting function to the wavelength dependent optical parameters τ , α and ρ to yield a single effective value for each of the parameters via integration termed “vis” used for light coming from the solar simulator. Analogously, the emissive intensity spectrum of a black-body at 600 °C is used as a weighting function to yield effective values for τ , α and ρ in the infrared wavelength range termed “IR” which are used for light that is emitted from the hot surfaces. The emissivities of the hot surfaces are taken to be $\epsilon = \alpha^{\text{IR}}$ via the application of Kirchhoff’s law [54]. Table B.2 lists the values of the effective optical properties used in this study.

Heat transport via radiation at both the upper and lower boundaries of the photo-thermal reactor is considered in detail in the following. Fig. B.9 illustrates the irradiation exchange in the top and bottom chambers of the reactor: in the upper chamber the irradiation exchange between the quartz glass window (surface 1) and the catalyst layer (surface 2) contributes to the boundary condition for the thermal energy equation at the top boundary (4.3) in form of the radiation energy flux density term $[\psi^{T,\text{rad}}]_{T_{\text{in}}}$ and in the lower chamber the irradiation exchange between the porous support (surface 3) and the reactor wall (surface 4) contributes to the boundary condition for the thermal energy equation at the bottom boundary (4.2) in the form of $[\psi^{T,\text{rad}}]_{T_{\text{out}}}$. Expressions for the radiation energy flux densities at the top and bottom boundaries are obtained from radiation balances for the surfaces marked by red dashed lines in Fig. B.9.

Considering black-body radiation via the Stefan–Boltzmann law [54] and absorption of radiation coming from the quartz window (surface 1) we obtain for the top/inlet boundary:

$$[\psi^{T,\text{rad}}]_{T_{\text{in}}} = -\epsilon_2 \sigma T_2^4 + \alpha_2^{\text{vis}} G_1^{\text{vis}} + \alpha_2^{\text{IR}} G_1^{\text{IR}} \quad (\text{B.1})$$

where G_1^{vis} corresponds to the effective radiation flux density profile incident in the catalyst surface shown in Fig. 4 and $G_1^{\text{IR}} = \epsilon_1 \sigma T_1^4$.

Because the catalyst layer and porous support are treated as opaque there is no radiation in the visible spectrum in the lower chamber so radiation exchange originates from black-body radiation emitted from the hot surfaces. Analogously, considering black-body radiation, absorption and reflection we obtain for the bottom/outlet boundary:

$$[\psi^{T,\text{rad}}]_{T_{\text{out}}} = -\epsilon_3 \sigma T_3^4 + \frac{\alpha_3^{\text{IR}}}{1 - \rho_3^{\text{IR}} \rho_4^{\text{IR}}} (\epsilon_4 \sigma T_4^4 + \rho_4^{\text{IR}} \epsilon_3 \sigma T_3^4) \quad (\text{B.2})$$

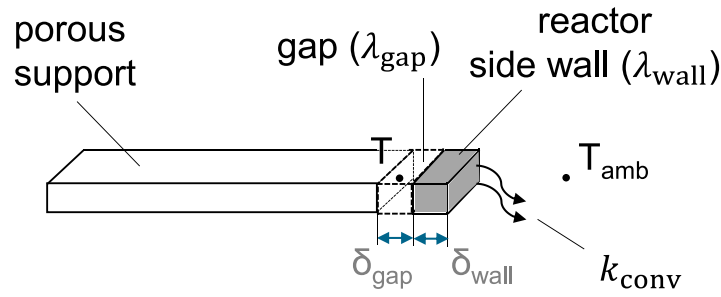


Fig. C.10. Geometry at the side wall boundary of the modeling domain and heat flux at reactor side walls.

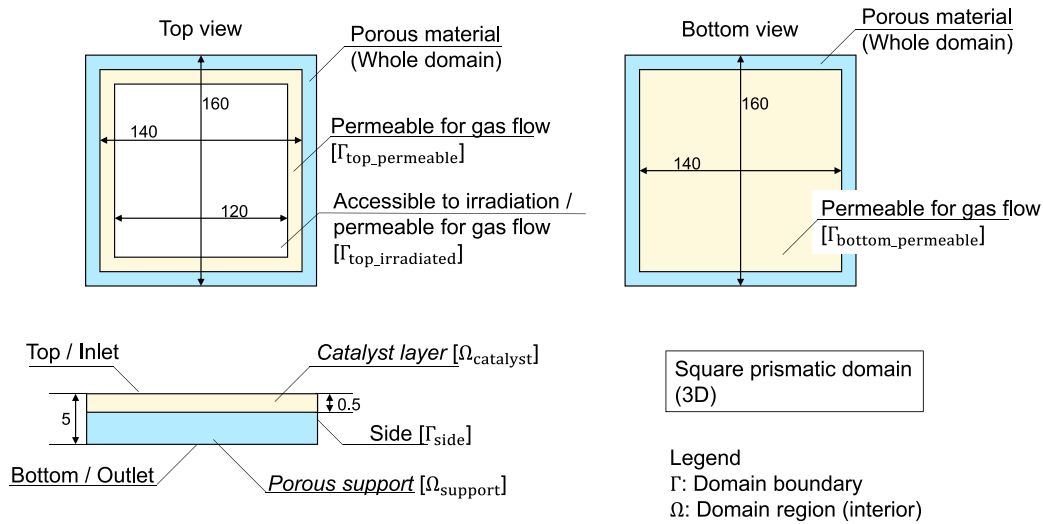


Fig. D.11. Schematic views on square prismatic modeling domain of the photo-thermal catalytic reactor with associated boundaries. (Drawings are not to scale, all dimensions in mm.).

Appendix C. Convection at reactor side walls

The geometry and thermal boundary condition at the side walls of the modeling domain are detailed in Fig. C.10. The heat flux through the side walls \dot{q}_{side} is a function of the convective heat transfer coefficient on the outside of the reactor. For this study, a natural convection heat transfer coefficient $k_{conv} = 10 \text{ W}/(\text{m}^2\text{K})$ [55] is applied. The temperature drop over the thickness of the reactor wall is neglected due to the high thermal conductivity of Aluminum and wall thickness of around 2 cm.

$$\vec{n} \cdot (c\rho T\langle\vec{v}\rangle - \lambda_{eff}\nabla T) = (T - T_{amb}) \left(\frac{\delta_{gap}}{\lambda_{gap}} + \frac{\delta_{wall}}{\lambda_{wall}} + \frac{1}{k_{conv}} \right)^{-1} \quad (\text{C.1})$$

$$\approx (T - T_{amb}) \left(\frac{\delta_{gap}}{\lambda_{gap}} + \frac{1}{k_{conv}} \right)^{-1} \quad (\text{C.2})$$

where the resistance to heat transfer posed by the conduction through the reactor wall is neglected due to

$$\frac{\delta_{wall}}{\lambda_{wall}} \ll \frac{\delta_{gap}}{\lambda_{gap}}.$$

Appendix D. Domain and boundaries

Fig. D.11 shows schematic views illustrating the dimensions of 3D prismatic modeling domain and associated boundaries used in the simulation of the photo-thermal catalytic reactor.

Appendix E. Homogenization

The homogenization method can be used in the context of porous media exhibiting complex geometry on multiple scales to obtain a macroscopic description from the microscopic or pore scale description. In the following, the two-scale homogenization method [25,26] is applied in order

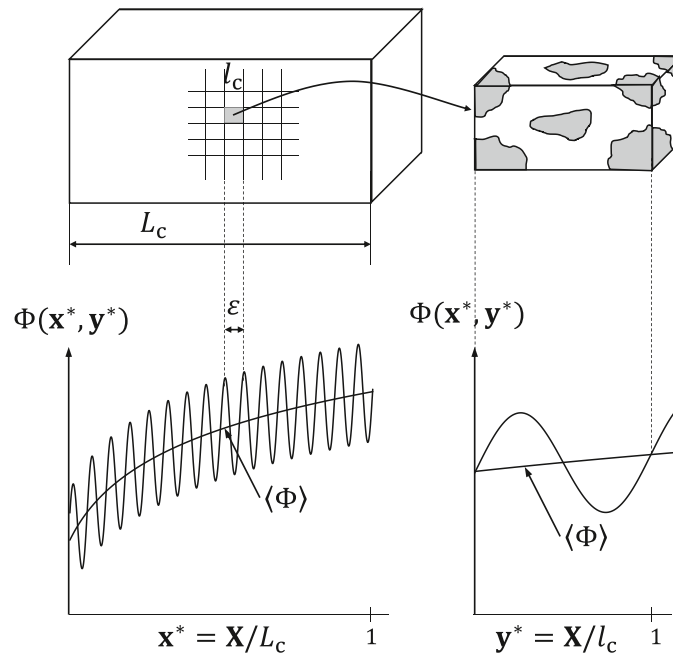


Fig. E.12. Macroscopic and microscopic (local) variation of Φ and corresponding variables x^*, y^* . Source: Reproduced from [26].

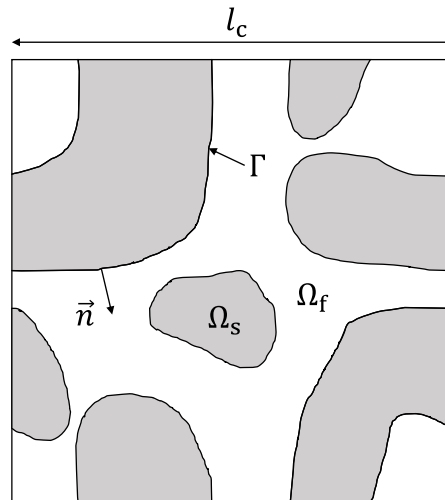


Fig. E.13. Period of porous domain. Source: Reproduced from [26].

to derive macroscopic equations from the microscopic descriptions of non-isothermal, compressible flow, multi-component species mass transfer including chemical reactions and thermal energy transport through rigid porous media.

The two-scale homogenization method is based on the macroscopic and microscopic (local) dimensionless coordinates (x^*, y^*) . The following relations will hold throughout the derivation:

$$x^* = X/L_c, \quad y^* = X/l_c, \quad \varepsilon = l_c/L_c, \quad dx^* = \varepsilon dy^*, \tag{E.1}$$

where X is the dimensional spatial variable and l_c and L_c are the characteristic length scales of the microscopic features e.g. pore size and the macroscopic features e.g. domain size, respectively. For the scale separation parameter ε it holds that $0 < \varepsilon \ll 1$.

This two-scale behavior is illustrated in Fig. E.12 by a quantity Φ that oscillates rapidly on the local scale described by the dimensionless coordinates (x^*, y^*) :

E.1. Non-isothermal flow in rigid, porous media

Homogenized equations for the single phase, compressible flow of gas in non-isothermal conditions through a porous medium consisting of a porous solid phase Ω_s saturated by the fluid (gas) phase Ω_f are derived. For an illustration of the fluid- and solid domains and their interface see Fig. E.13. Similar treatments are shown in [26,27] while in [56] variable porosity porous media are considered.

The pore scale equations consist of the momentum conservation (Navier–Stokes) and mass continuity equations in the pore space Ω_f occupied by the fluid phase combined with the no-slip boundary condition on the fluid–solid boundary Γ and the equation of state:

$$\left. \begin{aligned} \eta \Delta_{\mathbf{x}} \bar{v} - \nabla_{\mathbf{x}} p &= \rho \left(\frac{\partial \bar{v}}{\partial t} + (\bar{v} \cdot \nabla_{\mathbf{x}}) \bar{v} \right) && \text{in } \Omega_f \\ \frac{\partial \rho}{\partial t} + \nabla_{\mathbf{x}} \cdot (\rho \bar{v}) &= 0 && \text{in } \Omega_f \\ \bar{v} &= 0 && \text{on } \Gamma \\ f(p, T, \rho) &= 0 && \end{aligned} \right\} \quad (\text{PS})$$

It should be noted that (PS) only describes compressible gas flow through porous media while the other model components, species mass transport and heat transport, are considered in Appendices E.2 and E.3, respectively. Introduce the non-dimensional variables of order $\mathcal{O}(1)$ with superscript * by scaling the dimensional variables with characteristic values:

$$\begin{aligned} \eta &= \eta_c \eta^*, & \rho &= \rho_c \rho^*, & T &= T_c T^* \\ \bar{v} &= v_c \bar{v}^* & p &= p_c p^*, & t &= t^* / \omega_c = t^* L_c / v_c \end{aligned} \quad (\text{E.2})$$

Physical arguments and equation scaling

With the characteristic quantities from (E.2) we can define the following dimensionless numbers and assess their magnitude based on physical considerations starting with the Reynolds number in terms of the macroscopic length scale Re_L :

$$\text{Re}_L = \frac{\rho_c v_c L_c}{\eta_c}$$

In our application, slow flow prevails resulting in $\text{Re}_L = \mathcal{O}(1)$ and $\text{Re}_l = \mathcal{O}(\varepsilon)$, respectively. For slow flow conditions, the inertial terms in the momentum equation become small compared to the remaining terms.

In filtration experiments a pressure drop of order $\mathcal{O}(p_c)$ occurs over the flow distance $\mathcal{O}(L_c)$ corresponding to the macroscopic domain length. Thus, the magnitude of the pressure gradient can be estimated by: $|\nabla_{\mathbf{x}} p| = \mathcal{O}(p_c / L_c)$. Viscous drag in flows through porous media at low Reynolds numbers predominantly occurs due to the no-slip condition on the gas–solid boundaries. The deciding length scale for viscous drag is thus the pore scale of order $\mathcal{O}(l_c)$ leading to $|\eta \Delta_{\mathbf{x}} \bar{v}| = \mathcal{O}(\eta_c v_c / l_c^2)$. In mechanical equilibrium, the viscous drag in the pores balances out the macroscopic pressure gradient:

$$\mathcal{O}(|\nabla_{\mathbf{x}} p|) = \mathcal{O}(|\eta \Delta_{\mathbf{x}} \bar{v}|)$$

$$\mathcal{O}(p_c / L_c) = \mathcal{O}(\eta_c v_c / l_c^2)$$

This leads to the scaling of the dimensionless number Q_l :

$$Q_l = \frac{p_c}{L_c} \frac{l_c^2}{\eta_c v_c} = \mathcal{O}(1)$$

Recalling (E.1) we have:

$$Q_l = \frac{p_c}{L_c} \frac{\varepsilon^2 L_c^2}{\eta_c v_c} = \varepsilon^2 Q_L$$

$$Q_L = \mathcal{O}(\varepsilon^{-2})$$

which is consistent with a definition for the characteristic pressure $p_c = \eta_c v_c L_c / l_c^2$. The transient Reynolds number R_t can also be written as $R_t = (\omega_c \tau_d)^2$ where ω_c is the frequency of the transient process and $\tau_d = l_c \sqrt{\rho_c / (\omega_c \eta_c)}$ is the time duration taken by diffusive shear wave carrying momentum across the microscopic spatial-period. By considering transient processes that are slow compared to diffusive momentum transfer within the pore space, we obtain $\omega_c \tau_d = \mathcal{O}(\varepsilon)$ and thus $R_{t,l} = \mathcal{O}(\varepsilon^2)$ and $R_{t,L} = \mathcal{O}(1)$. Further, we obtain for the Strouhal number $S = R_{t,L} / \text{Re}_L = \mathcal{O}(1)$.

The governing equations at the pore scale can then be written in dimensionless form:

$$\left. \begin{aligned} \eta^* \Delta_{\mathbf{x}^*} \bar{v}^* - \underbrace{\frac{p_c}{L_c} \frac{L_c^2}{\eta_c v_c}}_{Q_L = \mathcal{O}(\varepsilon^{-2})} \nabla_{\mathbf{x}^*} p^* &= \underbrace{\frac{\rho_c v_c L_c}{\eta_c}}_{\text{Re}_L = \mathcal{O}(1)} \rho^* \left(\underbrace{\frac{L_c \omega_c}{v_c}}_{S = \mathcal{O}(1)} \frac{\partial \bar{v}^*}{\partial t^*} + (\bar{v}^* \cdot \nabla_{\mathbf{x}^*}) \bar{v}^* \right) && \text{in } \Omega_f^* \\ \underbrace{\frac{L_c \omega_c}{v_c}}_{S = \mathcal{O}(1)} \frac{\partial \rho^*}{\partial t^*} + \nabla_{\mathbf{x}^*} \cdot (\rho^* \bar{v}^*) &= 0 && \text{in } \Omega_f^* \\ \bar{v}^* &= 0 && \text{on } \Gamma^* \\ f(p^*, T^*, \rho^*) &= 0 && \end{aligned} \right\} \quad (\text{PS}^*)$$

Homogenization ansatz

We introduce the homogenization ansatz using asymptotic expansions with different orders of the scale separation parameter written in the two-scale coordinates $(\mathbf{x}^*, \mathbf{y}^*)$ with $\mathbf{y}^* = \varepsilon^{-1} \mathbf{x}^*$ for the dimensionless quantities $\bar{v}^*, p^*, \rho^*, T^*$ where we show here only $\bar{v}^*(\mathbf{x}^*, \mathbf{y}^*)$ with the full set of quantities in [25,26]:

$$\bar{v}^*(\mathbf{x}^*, \mathbf{y}^*) = \bar{v}_0^*(\mathbf{x}^*, \mathbf{y}^*) + \varepsilon \bar{v}_1^*(\mathbf{x}^*, \mathbf{y}^*) + \varepsilon^2 \bar{v}_2^*(\mathbf{x}^*, \mathbf{y}^*) + \dots$$

where functions $\bar{v}_i^*, p_i^*, \rho_i^*, T_i^*$ are periodic in \mathbf{y}^* in the sense that

$$\bar{v}_i^*(\mathbf{x}^*, \mathbf{y}^* + k) = \bar{v}_i^*(\mathbf{x}^*, \mathbf{y}^*), \quad k \in \mathbb{Z} \quad (\text{E.3})$$

with period of size 1 as the scaling variable l_c was chosen accordingly. The dimensionless viscosity η^* is approximated to the first order $\eta^* = \eta_0^*(p_0^*, T_0^*)$. The Taylor series expansion of the dimensionless equation of state $f^*(p^*, T^*, \rho^*)$ around the support point p_0^*, T_0^*, ρ_0^* truncated after the first term will be used in the following. Assuming f is at least once differentiable in the neighborhood of the support point, the total differential of f^* , df^* evaluated at (p^*, T^*, ρ^*) can be written as:

$$df^*(p^*, T^*, \rho^*) = \frac{\partial f^*}{\partial p^*} dp^* + \frac{\partial f^*}{\partial T^*} dT^* + \frac{\partial f^*}{\partial \rho^*} d\rho^*$$

The Taylor series approximation truncated after the first term with $dp^* = p^* - p_0^*$, $dT^* = T^* - T_0^*$, $d\rho^* = \rho^* - \rho_0^*$ thus takes the form:

$$\begin{aligned} f^*(p^*, T^*, \rho^*) &= f^*(p_0^*, T_0^*, \rho_0^*) + df^*(p_0^*, T_0^*, \rho_0^*) + \mathcal{O}(\varepsilon^2) \\ &= f^*(p_0^*, T_0^*, \rho_0^*) + \varepsilon \left(\frac{\partial f^*}{\partial p_0^*} p_1^* + \frac{\partial f^*}{\partial T_0^*} T_1^* + \frac{\partial f^*}{\partial \rho_0^*} \rho_1^* \right) + \mathcal{O}(\varepsilon^2) \end{aligned}$$

As part of the two-scale expansion method we perform a change of independent variables $\mathbf{X} \rightarrow (\mathbf{x}^*, \mathbf{y}^*)$ and thus transform the derivative operator using (E.1): $\nabla_{\mathbf{X}} \rightarrow \nabla_{\mathbf{x}^*} + \varepsilon^{-1} \nabla_{\mathbf{y}^*}$. The transformed Laplace operator thus becomes:

$$\begin{aligned} \Delta_{\mathbf{X}} &= \nabla_{\mathbf{X}} \cdot \nabla_{\mathbf{X}} \rightarrow (\nabla_{\mathbf{x}^*} + \varepsilon^{-1} \nabla_{\mathbf{y}^*}) \cdot (\nabla_{\mathbf{x}^*} + \varepsilon^{-1} \nabla_{\mathbf{y}^*}) \\ &= \Delta_{\mathbf{x}^*} + \frac{1}{\varepsilon} (\nabla_{\mathbf{x}^*} \cdot \nabla_{\mathbf{y}^*} + \nabla_{\mathbf{y}^*} \cdot \nabla_{\mathbf{x}^*}) + \frac{1}{\varepsilon^2} \Delta_{\mathbf{y}^*} \end{aligned}$$

Using the homogenization ansatz and the transformed differential operators we obtain for (PS*):

$$\begin{aligned} &\varepsilon^2 \eta_0^* (\Delta_{\mathbf{x}^*} + \varepsilon^{-1} (\nabla_{\mathbf{x}^*} \cdot \nabla_{\mathbf{y}^*} + \nabla_{\mathbf{y}^*} \cdot \nabla_{\mathbf{x}^*}) + \varepsilon^{-2} \Delta_{\mathbf{y}^*}) (\bar{v}_0^* + \varepsilon \bar{v}_1^* + \varepsilon^2 \bar{v}_2^*) \\ &- (\nabla_{\mathbf{x}^*} + \varepsilon^{-1} \nabla_{\mathbf{y}^*}) (\rho_0^* + \varepsilon \rho_1^* + \varepsilon^2 \rho_2^*) \\ &= \varepsilon^2 (\rho_0^* + \varepsilon \rho_1^* + \varepsilon^2 \rho_2^*) \left(\frac{\partial}{\partial t^*} (\bar{v}_0^* + \varepsilon \bar{v}_1^* + \varepsilon^2 \bar{v}_2^*) \right. \\ &+ (\bar{v}_0^* + \varepsilon \bar{v}_1^* + \varepsilon^2 \bar{v}_2^*) \cdot (\nabla_{\mathbf{x}^*} + \varepsilon^{-1} \nabla_{\mathbf{y}^*}) (\bar{v}_0^* + \varepsilon \bar{v}_1^* + \varepsilon^2 \bar{v}_2^*) \left. \right) \quad \text{in } \Omega_f^* \\ &\frac{\partial}{\partial t^*} (\rho_0^* + \varepsilon \rho_1^* + \varepsilon^2 \rho_2^*) \\ &+ (\nabla_{\mathbf{x}^*} + \varepsilon^{-1} \nabla_{\mathbf{y}^*}) \cdot ((\rho_0^* + \varepsilon \rho_1^* + \varepsilon^2 \rho_2^*) (\bar{v}_0^* + \varepsilon \bar{v}_1^* + \varepsilon^2 \bar{v}_2^*)) = 0 \quad \text{in } \Omega_f^* \\ &\bar{v}_0^* + \varepsilon \bar{v}_1^* + \varepsilon^2 \bar{v}_2^* = 0 \quad \text{on } \Gamma^* \\ &f^*(p_0^*, T_0^*, \rho_0^*) + \varepsilon \left(\frac{\partial f^*}{\partial p_0^*} p_1^* + \frac{\partial f^*}{\partial T_0^*} T_1^* + \frac{\partial f^*}{\partial \rho_0^*} \rho_1^* \right) + \mathcal{O}(\varepsilon^2) = 0 \end{aligned} \quad (\text{E.4})$$

Proceeding, we replace (E.4)₂ by its equivalent scaled version (E.4)₂ $\Leftrightarrow \varepsilon \cdot$ (E.4)₂ to yield the equivalent system:

$$\widetilde{(\text{E.4})} = \begin{matrix} (\text{E.4})_1 \\ \varepsilon \cdot (\text{E.4})_2 \\ (\text{E.4})_3 \\ (\text{E.4})_4 \end{matrix} \quad (\widetilde{\text{E.4}})$$

Equating the terms in increasing order of ε we obtain for the order of ε^{-1} :

$$\nabla_{\mathbf{y}^*} p_0^* = 0 \quad \text{in } \Omega^* \quad (\varepsilon^{-1})$$

From (E-1)₁ we can conclude that $p_0^*(\mathbf{x}^*, \mathbf{y}^*) = p_0^*(\mathbf{x}^*)$.

The terms of order ε^0 are:

$$\begin{aligned} \eta_0^* \Delta_{\mathbf{y}^*} \bar{v}_0^* - \nabla_{\mathbf{x}^*} p_0^* - \nabla_{\mathbf{y}^*} p_1^* &= 0 \quad \text{in } \Omega_f^* \\ \nabla_{\mathbf{y}^*} \cdot (\rho_0^* \bar{v}_0^*) &= 0 \quad \text{in } \Omega_f^* \\ \bar{v}_0^* &= 0 \quad \text{on } \Gamma^* \\ f^*(p_0^*, T_0^*, \rho_0^*) &= 0 \end{aligned} \quad (\varepsilon^0)$$

For the construction of the Darcy-scale velocity \bar{v}_0^* , we use the linearity of (E⁰) and obtain \bar{v}_0^* as a linear combination of the partial derivatives of p_0^* , $\frac{\partial p_0^*}{\partial x_k^*}(\mathbf{x}^*) = \bar{e}_k \partial p_0^* / \partial x_k^*$ where \bar{e}_k are the Cartesian unit vectors:

$$\begin{aligned} \bar{v}_0^*(\mathbf{x}^*, \mathbf{y}^*) &= -\frac{1}{\eta_0^*} \sum_{k=1}^d \frac{\partial p_0^*}{\partial x_k^*}(\mathbf{x}^*) \bar{e}_k(\mathbf{y}^*) \\ p_1^*(\mathbf{x}^*, \mathbf{y}^*) &= \sum_{k=1}^d \frac{\partial p_0^*}{\partial x_k^*}(\mathbf{x}^*) \Pi_k(\mathbf{y}^*) \end{aligned} \quad (\text{E.5})$$

with $\bar{\kappa}_k(\mathbf{y}^*)$ and $\Pi_k(\mathbf{y}^*)$ being \mathbf{y}^* -periodic functions and $\int_{\mathbf{y}^*} \Pi_j d\mathbf{y}^* = 0$. Then, with v_0^* and p_1^* from (E.5) we equate terms in ε in $(\tilde{\varepsilon}^0)_1$, $(\tilde{\varepsilon}^0)_2$ and $(\tilde{\varepsilon}^0)_3$ and we obtain:

$$\begin{aligned} \eta_0^* \Delta_{\mathbf{y}^*} \left(-\frac{1}{\eta_0^*} \sum_{k=1}^d \frac{\partial p_0^*}{\partial x_k^*}(\mathbf{x}^*) \bar{\kappa}_k(\mathbf{y}^*) \right) &= \sum_{k=1}^d \frac{\partial p_0^*}{\partial x_k^*}(\mathbf{x}^*) \bar{e}_k \\ &+ \nabla_{\mathbf{y}^*} \cdot \left(\sum_{k=1}^d \frac{\partial p_0^*}{\partial x_k^*}(\mathbf{x}^*) \Pi_k(\mathbf{y}^*) \right) \quad \text{in } \Omega_f^* \\ \nabla_{\mathbf{y}^*} \cdot \left(\rho_0^* \left(-\frac{1}{\eta_0^*} \sum_{k=1}^d \frac{\partial p_0^*}{\partial x_k^*}(\mathbf{x}^*) \bar{\kappa}_k(\mathbf{y}^*) \right) \right) &= 0 \quad \text{in } \Omega_f^* \\ -\frac{1}{\eta_0^*} \sum_{k=1}^d \frac{\partial p_0^*}{\partial x_k^*}(\mathbf{x}^*) \bar{\kappa}_k(\mathbf{y}^*) &= 0 \quad \text{on } \Gamma^* \end{aligned} \quad (\tilde{P}_k)$$

The functions $\bar{\kappa}_k$ and $\Pi_k(\mathbf{y}^*)$ should solve (\tilde{P}_k) for all $\nabla_{\mathbf{x}^*} p_0^*$. One way to achieve this is to consider each coordinate k individually and to separate the derivatives with respect to \mathbf{x}^* and \mathbf{y}^* due to the linearity of (\tilde{P}_k) . Considering that $p_0^*(\mathbf{x}^*, \mathbf{y}^*) = p_0^*(\mathbf{x}^*)$ from $(\tilde{\varepsilon}^{-1})$ and that $T_0^*(\mathbf{x}^*, \mathbf{y}^*) = T_0^*(\mathbf{x}^*)$ from (E.50) in Appendix E.3, we also see that

$$\rho_0^*(\mathbf{x}^*, \mathbf{y}^*) = \rho_0^*(\mathbf{x}^*) \quad (\text{E.6})$$

from $(\text{PS}^*)_4$.

Thus, we obtain the so-called ‘‘cell’’ or ‘‘canonical’’ problems [25,26] for each $k = 1 \dots d$:

$$\left. \begin{aligned} -A_{\mathbf{y}^*} \bar{\kappa}_k(\mathbf{y}^*) &= \bar{e}_j + \nabla_{\mathbf{y}^*} \Pi_j(\mathbf{y}^*) && \text{in } \Omega_f^* \\ \nabla_{\mathbf{y}^*} \cdot \bar{\kappa}_k(\mathbf{y}^*) &= 0 && \text{in } \Omega_f^* \\ \bar{\kappa}_k(\mathbf{y}^*) &= 0 && \text{on } \Gamma^* \end{aligned} \right\} \quad (\text{P}_j)$$

Before deriving the homogenized equations and effective quantities on the Darcy or macroscopic scale, the functions expressed in the two-scale coordinates must be spatially averaged. For this, a period of the porous domain is shown in Fig. E.13 illustrating the fluid and solid domains Ω_f and Ω_s , respectively with $\Omega = \Omega_f \cup \Omega_s$, the interface Γ and normal vector \bar{n} : We introduce the dimensionless volumetric averaging operator that integrates over the dimensionless period corresponding to a representative elementary volume Ω^* :

$$\langle \cdot \rangle = \frac{1}{|\Omega^*|} \int_{\Omega^*} \cdot d\tilde{\Omega}^* \quad (\text{E.7})$$

The sections on the boundary of the period belonging to either the fluid or solid phase, S_f or S_s are defined as $S_f = \Omega_f \cap \partial\Omega$ and $S_s = \Omega_s \cap \partial\Omega$, respectively.

With the solutions to the cell problem $\bar{\kappa}_k$ we can write $\bar{v}_0^*(\mathbf{x}^*, \mathbf{y}^*)$ as:

$$\bar{v}_0^*(\mathbf{x}^*, \mathbf{y}^*) = -\frac{1}{\eta_0^*} \mathbf{k}^* \nabla_{\mathbf{x}^*} p_0^*(\mathbf{x}^*) \quad (\text{E.8})$$

which is the Darcy equation where \mathbf{k}^* is the permeability tensor corresponding to the solutions of the cell problems $\bar{\kappa}_k$ as column vectors:

$$\mathbf{k}^* = \left(\begin{array}{ccc} \langle \bar{\kappa}_1 \rangle & \dots & \langle \bar{\kappa}_d \rangle \end{array} \right) \quad (\text{E.9})$$

For leading order ε we get for Eqs. $(\tilde{\varepsilon}^0)_2$ and $(\tilde{\varepsilon}^0)_3$:

$$\begin{aligned} \frac{\partial \rho_0^*}{\partial t^*} + \nabla_{\mathbf{x}^*} \cdot (\rho_0^* \bar{v}_0^*) + \nabla_{\mathbf{y}^*} \cdot (\rho_0^* \bar{v}_1^* + \rho_1^* \bar{v}_0^*) &= 0 \quad \text{in } \Omega_f^* \\ \bar{v}_1^* &= 0 \quad \text{on } \Gamma^* \end{aligned} \quad (\tilde{\varepsilon}^1)$$

To obtain a macroscopic description of mass continuity, we apply the volumetric averaging operator to $(\tilde{\varepsilon}^1)_1$ and apply the Gaußtheorem and considering that $\rho_0^* = \rho_0^*(\mathbf{x}^*)$:

$$\begin{aligned} \langle \frac{\partial \rho_0^*}{\partial t^*} \rangle + \langle \nabla_{\mathbf{x}^*} \cdot (\rho_0^* \bar{v}_0^*) \rangle + \frac{1}{|\Omega^*|} \int_{\Omega_f^*} \nabla_{\mathbf{y}^*} \cdot (\rho_0^* \bar{v}_1^* + \rho_1^* \bar{v}_0^*) d\Omega^* &= 0 \\ \phi \frac{\partial \rho_0^*}{\partial t^*} + \nabla_{\mathbf{x}^*} \cdot (\rho_0^* \langle \bar{v}_0^* \rangle) + \frac{1}{|\Omega^*|} \int_{\partial\Omega_f^*} (\rho_0^* \bar{v}_1^* + \rho_1^* \bar{v}_0^*) \cdot \bar{n} dS^* &= 0 \end{aligned}$$

Here we introduce the porosity or void fraction $\phi = |\Omega_f^*|/|\Omega^*|$ which is the volume occupied by the fluid phase $|\Omega_f^*|$ divided by the total volume $|\Omega^*|$.

The boundary of the fluid occupied pore domain consists of two parts: $\partial\Omega_f^* = \Gamma \cup S_f^*$ and thus the flux integral over the boundaries becomes:

$$\begin{aligned} \int_{\partial\Omega_f^*} (\rho_0^* \bar{v}_1^* + \rho_1^* \bar{v}_0^*) \cdot \bar{n} dS^* &= \int_{S_f^*} (\rho_0^* \bar{v}_1^* + \rho_1^* \bar{v}_0^*) \cdot \bar{n} dS^* \\ &+ \int_{\Gamma^*} (\rho_0^* \bar{v}_1^* + \rho_1^* \bar{v}_0^*) \cdot \bar{n} dS^* \end{aligned} \quad (\text{E.10})$$

The first integral on the right-hand side of (E.10) vanishes due to the \mathbf{y}^* -periodicity over the unit cell of the functions \vec{v}_0^* , \vec{v}_1^* , ρ_0^* , ρ_1^* while the second integral vanishes due to the no-slip boundary condition on Γ^* , $(\vec{\epsilon}^0)_3$ and for leading order ϵ from $(\vec{\epsilon}^1)_2$.

To first order of approximation, the macroscopic description for non-isothermal, compressible flow through rigid porous media at low Reynolds number is given by:

$$\begin{aligned} \langle \vec{v}_0^* \rangle &= -1/\eta_0^* \mathbf{K}^* \nabla_{\mathbf{x}^*} p_0^* && \text{in } \Omega^* \\ \phi \frac{\partial \rho_0^*}{\partial t^*} + \nabla_{\mathbf{x}^*} \cdot (\rho_0^* \langle \vec{v}_0^* \rangle) &= 0 && \text{in } \Omega^* \\ f^*(p_0^*, T_0^*, \rho_0^*) &= 0 \end{aligned} \quad (\text{E.11})$$

With (E.7) the permeability tensor can be written as $\mathbf{K}^* = \langle \mathbf{k}^* \rangle$. In dimensional variables we have:

$$\begin{aligned} \langle \vec{v} \rangle &= -1/\eta \mathbf{K} \nabla_{\mathbf{x}} p && \text{in } \Omega \\ \phi \frac{\partial \rho}{\partial t} + \nabla_{\mathbf{x}} \cdot (\rho \langle \vec{v} \rangle) &= 0 && \text{in } \Omega \\ f(p, T, \rho) &= 0 \end{aligned} \quad (\text{E.12})$$

With the dimensional permeability tensor $\mathbf{K} = l_c^2 \mathbf{K}^*$.

E.2. Species mass transport

In the following, species mass transport in a porous medium consisting of a porous solid phase Ω_s and a fluid phase Ω_f (i.e. gas phase in this case) that saturates the pore space as shown in Fig. E.13 is described. The phase boundary is denoted as Γ . On the pore scale (PS), species mass transport occurs in the gas phase via diffusion superimposed by advection. Chemical reactions physically occur via the catalyst deposited on the walls of the porous solid. Calculations of mass transfer resistance from the bulk gas phase to the solid wall interface performed for typical reaction conditions in the computational notebook 'PTReactorDemo.jl' revealed, that mass transfer resistance is negligible. Therefore, the species concentrations on the surface of the solid catalyst which is deposited as a thin layer onto the walls of the porous solid phase are approximately equal to the bulk gas phase concentrations. Further, it is assumed that the deposited catalyst is fully accessible to the gas phase and therefore the heterogeneous gas–solid reactions are considered as homogeneous or bulk phase reactions with the volume averaged catalyst mass loading. Similar treatments can be found in [29,57] while both do not treat chemical reactions and the latter also includes a slip velocity on the pore walls. In [58] the reaction–diffusion–advection processes are treated for an evolving porous medium.

The equations for gas phase species mass conservation with reaction, diffusion and advection terms for n gas species where the Maxwell–Stefan formulation was chosen for the diffusive fluxes can be expressed together with the no-flux boundary condition on the impermeable boundary Γ for $i = 1, \dots, n$ as:

$$\left. \begin{aligned} \frac{\partial \rho_i}{\partial t} + \nabla_{\mathbf{x}} \cdot (\rho_i \vec{v} + \vec{J}_i) &= r_i(\phi), & i = 1 \dots n & \quad \text{in } \Omega_f \\ \vec{n} \cdot \vec{J}_i &= 0 & & \quad \text{on } \Gamma \\ - \sum_{\substack{j=1 \\ j \neq i}}^n \frac{x_j x_j}{D_{ij}} \left(\frac{\vec{J}_i}{\rho_i} - \frac{\vec{J}_j}{\rho_j} \right) &= \nabla_{\mathbf{x}} x_i & i = 1 \dots n-1 & \\ \sum_{i=1}^n \vec{J}_i &= 0 \end{aligned} \right\} \quad (\text{MT-PS})$$

where we recall from (PS) that $\vec{v} = 0$ on Γ . Because only $n-1$ of Maxwell–Stefan relations are linearly independent, the system is complemented by $\sum_{i=1}^n \vec{J}_i = 0$. To simplify the derivation of the upscaled equation for species mass transport, only the concentration gradients $\vec{d}_i = \nabla_{\mathbf{x}} x_i$ are considered as diffusive driving forces. Including other diffusive driving forces as pressure gradients (pressure diffusion) or temperature gradients (thermodiffusion) is straight forward, an upscaling procedure including pressure gradients is shown in [29].

Considering (MT-PS)₃ and (MT-PS)₄ which form a well-posed problem ensuring the unique solvability for $(\vec{J}_i)_{i=1}^n$ [15], we can explicitly write

$$\vec{J}_i = \sum_{j=1}^{n-1} B_{ij} \nabla_{\mathbf{x}} x_j \quad i = 1 \dots n-1 \quad (\text{E.13})$$

with $B_{ij} \neq 0$ which is convenient for the derivation of the upscaled equations with the homogenization method.

Introduce the non-dimensional variables of order $\mathcal{O}(1)$ with superscript * by scaling the dimensional variables with characteristic values:

$$\begin{aligned} \vec{v} &= v_c \vec{v}^*, & \mathbf{X} &= L_c \mathbf{x}^*, & \rho_i &= \rho_c \rho_i^*, & x_i &= x_c x_i^*, \\ v_c &= D_c / L_c, & t &= t_c t^*, & \vec{J}_i &= J_c \vec{J}_i^*, & w_i &= w_c w_i^*, \\ D_{ij} &= D_c D_{ij}^*, & t_c &= L_c^2 / D_c, & J_c &= \rho_c D_c / L_c, & r_i &= \rho_c / t_{c,r} r_i^*, \end{aligned}$$

where t_c and $t_{c,r}$ are the characteristic timescales of diffusive transport and chemical reaction, respectively.

Based on the characteristic quantities the following dimensionless numbers can be defined that indicate the relative magnitude of the different terms:

$$\text{Pe}_L = \frac{L_c v_c}{D_c}, \quad \text{Da} = \frac{t_c}{t_{c,r}}$$

The boundary value problem (MT-PS) can thus be rewritten with dimensionless variables in terms of the dimensionless numbers:

$$\left. \begin{aligned} \frac{\partial \rho_i^*}{\partial t^*} + \nabla_{\mathbf{x}^*} \cdot (\text{Pe}_L \rho_i^* \vec{v}^* + \vec{J}_i^*) &= \text{Da} r_i^*, \quad i = 1 \dots n && \text{in } \Omega_f^* \\ \vec{n} \cdot \vec{J}_i^* &= 0, \quad i = 1 \dots n && \text{on } \Gamma \\ - \sum_{\substack{j=1 \\ j \neq i}}^n \frac{x_i^* x_j^*}{D_{ij}^*} \left(\frac{\vec{J}_i^*}{\rho_i^*} - \frac{\vec{J}_j^*}{\rho_j^*} \right) &= \nabla_{\mathbf{x}^*} x_i^*, \quad i = 1 \dots n-1 \\ \sum_{i=1}^n \vec{J}_i^* &= 0 \end{aligned} \right\} \quad (\text{MT-PS}^*)$$

Physical arguments and equation scaling

The Peclet number $\text{Pe}_L = \mathcal{O}(1)$ for mass transport is computed on the one hand from the gas flow rate and thus the advective flow velocity that is specified as part of the experimental conditions and on the other hand from the characteristic diffusivity of the gas phase. Further, it is assumed that diffusive transport and chemical reaction occur at the same rate with $t_c/t_{c,r} = \mathcal{O}(1)$.

Homogenization ansatz

Next, we introduce the homogenization ansatz using asymptotic expansions with different orders of the scale separation parameter written in the two-scale coordinates $(\mathbf{x}^*, \mathbf{y}^*)$ with $\mathbf{y}^* = \varepsilon^{-1} \mathbf{x}^*$ for the dimensionless quantities $\rho_i^*, \vec{v}^*, x_i^*, w_i^*, D_{ij}^*$ as in [25,26].

We recall that the species mass fractions $w_i^* = w_i^*(x_i^*(\mathbf{x}^*, \mathbf{y}^*))$ are functions of the molar fractions $x_i^*(\mathbf{x}^*, \mathbf{y}^*)$. The species partial densities are related to the overall density via the species mass fractions $\rho_i^* = w_i^* \rho^*$.

Considering (E.13) we introduce further:

$$\begin{aligned} B_{ij}^*(\mathbf{x}^*, \mathbf{y}^*) &= B_{ij,0}^*(\mathbf{x}^*, \mathbf{y}^*) + \varepsilon B_{ij,1}^*(\mathbf{x}^*, \mathbf{y}^*) + \varepsilon^2 B_{ij,2}^*(\mathbf{x}^*, \mathbf{y}^*) + \dots \\ \vec{J}_i^*(\mathbf{x}^*, \mathbf{y}^*) &= \sum_{j=1}^{n-1} (B_{ij,0}^* + \varepsilon B_{ij,1}^* + \varepsilon^2 B_{ij,2}^*) (\nabla_{\mathbf{x}^*} + \varepsilon^{-1} \nabla_{\mathbf{y}^*}) (x_{j,0}^* + \varepsilon x_{j,1}^* + \varepsilon^2 x_{j,2}^*) + \dots \end{aligned} \quad (\text{E.14})$$

For convenience, we introduce the shorthand notation

$$\vec{J}_{i,-1}^* = \sum_{j=1}^{n-1} B_{ij,0}^* \nabla_{\mathbf{y}^*} x_{j,0}^* \quad (\text{E.15})$$

at order ε^{-1} of the scale separation parameter so we can write:

$$\vec{J}_i^*(\mathbf{x}^*, \mathbf{y}^*) = \varepsilon^{-1} \vec{J}_{i,-1}^* + \vec{J}_{i,0}^* + \varepsilon \vec{J}_{i,1}^* + \mathcal{O}(\varepsilon^2) \quad (\text{E.16})$$

where $\vec{J}_{i,0}^*$ and $\vec{J}_{i,1}^*$ correspond to the sum of order ε^0 and ε^1 terms in (E.14), respectively.

Further, we apply Taylor series expansion of the dimensionless bulk reaction rate for the gas phase species $r_i^*(\varrho^*)$ around the support point ϱ_0^* , truncated after the first term with the vector of species mass densities $(\varrho^*)_i = \rho_i^*$. Assuming r_i^* is at least once differentiable in the neighborhood of the support point, the total differential of r_i^* , dr_i^* can be written as:

$$dr_i^*(\varrho^*) = \sum_{j=1}^n \frac{\partial r_i^*}{\partial \rho_j^*} d\rho_j^*$$

Then, the Taylor series approximation developed around ϱ_0^* truncated after the first term with $d\varrho^* = \varrho^* - \varrho_0^*$ thus takes the form:

$$\begin{aligned} r_i^*(\varrho^*) &= r_i^*(\varrho_0^*) + dr_i^*(\varrho_0^*) + \mathcal{O}(\varepsilon^2) \\ &= r_i^*(\varrho_0^*) + \varepsilon \left(\sum_{j=1}^n \frac{\partial r_i^*}{\partial \rho_{j,0}^*} \rho_{j,1}^* \right) + \mathcal{O}(\varepsilon^2) \\ &= r_{i,0}^*(\varrho_0^*) + \varepsilon r_{i,1}^*(\varrho_1^*) + \mathcal{O}(\varepsilon^2) \end{aligned}$$

Inserting the ansatz functions into (MT-PS*) considering the transformed differential operators we obtain when writing in index notation $i = 1 \dots n$:

$$\begin{aligned} \frac{\partial}{\partial t^*} (\rho_{i,0}^* + \varepsilon \rho_{i,1}^* + \varepsilon^2 \rho_{i,2}^*) + (\nabla_{\mathbf{x}^*} + \varepsilon^{-1} \nabla_{\mathbf{y}^*}) \cdot (\rho_{i,0}^* + \varepsilon \rho_{i,1}^* + \varepsilon^2 \rho_{i,2}^*) \\ (\vec{v}_0^* + \varepsilon \vec{v}_1^* + \varepsilon^2 \vec{v}_2^*) + (\varepsilon^{-1} \vec{J}_{i,-1}^* + \vec{J}_{i,0}^* + \varepsilon \vec{J}_{i,1}^*) = r_{i,0}^* + \varepsilon r_{i,1}^* + \mathcal{O}(\varepsilon^2), && \text{in } \Omega_f^* \\ \vec{n} \cdot (\varepsilon^{-1} \vec{J}_{i,-1}^* + \vec{J}_{i,0}^* + \varepsilon \vec{J}_{i,1}^*) = 0, && \text{on } \Gamma \\ \varepsilon^{-1} \vec{J}_{i,-1}^* + \vec{J}_{i,0}^* + \varepsilon \vec{J}_{i,1}^* = \\ \sum_{j=1}^{n-1} (B_{ij,0}^* + \varepsilon B_{ij,1}^* + \varepsilon^2 B_{ij,2}^*) (\nabla_{\mathbf{x}^*} + \varepsilon^{-1} \nabla_{\mathbf{y}^*}) (x_{j,0}^* + \varepsilon x_{j,1}^* + \varepsilon^2 x_{j,2}^*) \\ \sum_{i=1}^n (\varepsilon^{-1} \vec{J}_{i,-1}^* + \vec{J}_{i,0}^* + \varepsilon \vec{J}_{i,1}^*) = 0 \end{aligned} \quad (\text{E.17})$$

Proceeding, we replace (E.17)₁ by its equivalent scaled version (E.17)₁ $\Leftrightarrow \varepsilon \cdot$ (E.17)₁ to yield the equivalent system:

$$\begin{aligned} \varepsilon \cdot (\text{E.17})_1 \\ \widehat{(\text{E.17})} = & \quad (\text{E.17})_2 \\ & \quad (\text{E.17})_3 \\ & \quad (\text{E.17})_4 \end{aligned} \quad \widehat{(\text{E.17})}$$

Collecting the terms in increasing order of ϵ we get for order ϵ^{-1} from (E.17) for $i = 1 \dots n$:

$$\begin{aligned} \nabla_{\mathbf{y}^*} \cdot \vec{J}_{i,-1}^* &= 0 && \text{in } \Omega_f^* \\ \vec{n} \cdot \vec{J}_{i,-1}^* &= 0 && \text{on } \Gamma \\ \vec{J}_{i,-1}^* &= \sum_{j=1}^{n-1} B_{ij,0}^* \nabla_{\mathbf{y}^*} x_{j,0}^* \\ \sum_{i=1}^n \vec{J}_{i,-1}^* &= 0 \end{aligned} \tag{E.18}$$

We find from (E.18)_{1,2} that $\vec{J}_{i,-1}^* = 0$ and with $B_{ij,0}^* \neq 0$ we get $\nabla_{\mathbf{y}^*} x_{i,0}^* = 0$ in Ω_f^* . We can deduce, that $x_{i,0}^*(\mathbf{x}^*, \mathbf{y}^*) = x_{i,0}^*(\mathbf{x}^*)$. The next higher order terms, of order ϵ^0 , reveal:

$$\begin{aligned} \nabla_{\mathbf{y}^*} \cdot \vec{J}_{i,0}^* &= 0 && \text{in } \Omega_f^* \\ \vec{n} \cdot \vec{J}_{i,0}^* &= 0 && \text{on } \Gamma \\ \vec{J}_{i,0}^* &= \sum_{j=1}^{n-1} B_{ij,0}^* (\nabla_{\mathbf{x}^*} x_{j,0}^* + \nabla_{\mathbf{y}^*} x_{j,1}^*) \\ \sum_{i=1}^n \vec{J}_{i,0}^* &= 0 \end{aligned} \tag{E.19}$$

In order to obtain (E.19)₁ at order ϵ^0 from (E.17) starting from $\rho_{i,0}^* = w_{i,0}^* \rho_0^*$ we apply the product and chain rules of differentiation to show that $\nabla_{\mathbf{y}^*} \cdot (\rho_{i,0}^* \vec{v}_0^*) = 0$ with $\nabla_{\mathbf{y}^*} \cdot (\rho_0^* \vec{v}_0^*) = 0$ from (E⁰) in Appendix E.1 and:

$$\nabla_{\mathbf{y}^*} w_{i,0}^* = \nabla_{\mathbf{y}^*} w_{i,0}^* (x_{i,0}^*(\mathbf{x}^*)) \underbrace{\nabla_{\mathbf{y}^*} x_{i,0}^*(\mathbf{x}^*)}_{=0} = 0. \tag{E.20}$$

With (E.6) and (E.20) we get

$$\nabla_{\mathbf{y}^*} \rho_{i,0}^* = 0. \tag{E.21}$$

Similar to Appendix E.1 we then write $\nabla_{\mathbf{x}^*} x_{i,0}^* = \partial x_{i,0}^* / \partial x_k^*$ for coordinate $k = 1, \dots, d$ of spatial dimension d , and we assume that the \mathbf{y}^* -periodic functions $x_{i,1}^*$ can be written as linear combinations of $\nabla_{\mathbf{x}^*} x_{i,0}^*$ and the \mathbf{y}^* -periodic, d -dimensional functions $\vec{\chi}(\mathbf{y}^*)$:

$$x_{i,1}^*(\mathbf{x}^*, \mathbf{y}^*) = \sum_{k=1}^d \frac{\partial x_{i,0}^*}{\partial x_k^*}(\mathbf{x}^*) \chi_k(\mathbf{y}^*) \tag{E.22}$$

with $\int_{Y^*} \chi_k d\mathbf{y}^* = 0$ for $k = 1, \dots, d$.

We can thus rewrite the terms $\nabla_{\mathbf{x}^*} x_{i,0}^* + \nabla_{\mathbf{y}^*} x_{i,1}^*$ for species $i = 1, \dots, n$:

$$\begin{aligned} \nabla_{\mathbf{x}^*} x_{i,0}^* + \nabla_{\mathbf{y}^*} x_{i,1}^* &= \frac{\partial x_{i,0}^*}{\partial x_k^*}(\mathbf{x}^*) + \frac{\partial}{\partial y_k^*} \left(\sum_{l=1}^d \frac{\partial x_{i,0}^*}{\partial x_l^*}(\mathbf{x}^*) \chi_l(\mathbf{y}^*) \right), \quad k = 1, \dots, d \\ &= \sum_{l=1}^d \frac{\partial x_{i,0}^*}{\partial x_l^*}(\mathbf{x}^*) (\delta_{kl} + \frac{\partial}{\partial y_k^*} \chi_l(\mathbf{y}^*)), \quad k = 1, \dots, d \\ &= (\mathbf{I} + \nabla_{\mathbf{y}^*} \otimes \vec{\chi}) \nabla_{\mathbf{x}^*} x_{i,0}^* \end{aligned} \tag{E.23}$$

with Kronecker delta δ_{kl}

$$\delta_{kl} = \begin{cases} 0, & k \neq l \\ 1, & k = l. \end{cases}$$

Inserting (E.23) into (E.19)_{1,2} yields:

$$\begin{aligned} \nabla_{\mathbf{y}^*} \cdot \left(\sum_{j=1}^{n-1} B_{ij,0}^* (\mathbf{I} + \nabla_{\mathbf{y}^*} \otimes \vec{\chi}) \nabla_{\mathbf{x}^*} x_{j,0}^* \right) &= 0 && \text{in } \Omega_f^* \\ \vec{n} \cdot \left(\sum_{j=1}^{n-1} B_{ij,0}^* (\mathbf{I} + \nabla_{\mathbf{y}^*} \otimes \vec{\chi}) \nabla_{\mathbf{x}^*} x_{j,0}^* \right) &= 0 && \text{on } \Gamma \end{aligned} \tag{E.24}$$

The function $\vec{\chi}$ must be chosen such that (E.24) holds for all possible values of $\nabla_{\mathbf{x}^*} x_{i,0}^*$. We can consider each element χ_k individually and separate derivatives with respect to \mathbf{x}^* and \mathbf{y}^* due to the linearity of (E.24). We thus obtain the so-called cell problems to solve for the periodic functions $\chi_k(\mathbf{y}^*)$ in each spatial dimension $k = 1 \dots d$:

$$\begin{aligned} \nabla_{\mathbf{y}^*} \cdot (\vec{e}_k + \nabla_{\mathbf{y}^*} \chi_k(\mathbf{y}^*)) &= 0 && \text{in } \Omega_f^* \\ \vec{n} \cdot (\vec{e}_k + \nabla_{\mathbf{y}^*} \chi_k(\mathbf{y}^*)) &= 0 && \text{on } \Gamma \end{aligned} \tag{MT}_k$$

where \vec{e}_k is the k th unit vector in Cartesian coordinate system. Here we used the fact that $B_{ij,0}^* = B_{ij,0}^*(x_{i,0}^*, \rho_{i,0}^*, \vec{D}_{ij,0}^*)(\mathbf{x}^*) \neq 0$ are independent of the microscopic coordinate \mathbf{y}^* .

Finally, the terms of order ε for $(\text{E.17})_{1,2}$ yield:

$$\begin{aligned} & \underbrace{\frac{\partial \rho_{i,0}^*}{\partial t^*}}_{\textcircled{1}} + \underbrace{\nabla_{\mathbf{x}^*} \cdot (\rho_{i,0}^* \vec{v}_0^*)}_{\textcircled{2}} + \underbrace{\nabla_{\mathbf{x}^*} \cdot \vec{J}_{i,0}}_{\textcircled{3}} \\ & + \underbrace{\nabla_{\mathbf{y}^*} \cdot (\rho_{i,0}^* \vec{v}_0^* + \rho_{i,1}^* \vec{v}_1^*)}_{\textcircled{4}} + \underbrace{\nabla_{\mathbf{y}^*} \cdot \vec{J}_{i,1}}_{\textcircled{5}} = \underbrace{r_{i,0}^*}_{\textcircled{6}} \quad \text{in } \Omega_f^* \\ & \vec{n} \cdot \vec{J}_{i,1}^* = 0 \quad \text{on } \Gamma \end{aligned} \quad (\text{E.25})$$

To obtain a macroscopic description of gas phase species mass transport we apply the volumetric averaging operator (E.7) on (E.25)₁ and integrate over the period $\Omega^* = \Omega_f^* \cup \Omega_s^*$ with $|\Omega^*| = |\Omega_f^*| + |\Omega_s^*|$. Further, we make use of the Gauß divergence theorem and the Ω^* -periodicity of the fields that depend on the microscopic variable \mathbf{y}^* . The sections on the boundary of the period belonging to either the fluid or solid phase, are defined as $S_f^* = \Omega_f^* \cap \partial\Omega^*$ and $S_s^* = \Omega_s^* \cap \partial\Omega^*$, respectively. For an illustration of the spatial domain and its boundaries we refer to Fig. E.13. Here we introduce the porosity or void fraction $\phi = |\Omega_f^*|/|\Omega^*|$ which is the volume occupied by the fluid phase $|\Omega_f^*|$ divided by the total volume $|\Omega^*|$. We recall the identities:

$$\vec{J}_{i,0}^* = \nabla_{\mathbf{y}^*} \cdot (\mathbf{y}^* \otimes \vec{J}_{i,0}^*) \quad (\text{E.26})$$

$$\vec{J}_{i,0}^* = \sum_{j=1}^{n-1} B_{ij,0}^* (\mathbf{I} + \nabla_{\mathbf{y}^*} \otimes \vec{\chi}) \nabla_{\mathbf{x}^*} x_{j,0} \quad (\text{E.27})$$

Further we recall, that

$$\int_{\Omega^*} \cdot d\Omega^* = \int_{\Omega_f^*} \cdot d\Omega^* + \int_{\Omega_s^*} \cdot d\Omega^*$$

and that all terms of (E.25)₁ vanish in the interior of the solid domain Ω_s^* such that the respective integrals over the solid part of the domain also vanish. Proceeding on a term-by-term basis we obtain:

①:

$$\frac{1}{|\Omega^*|} \int_{\Omega^*} \frac{\partial}{\partial t^*} (\rho_{i,0}^*) d\Omega^* \stackrel{\text{with (E.21)}}{=} \phi \frac{\partial \rho_{i,0}^*}{\partial t^*} \quad (\text{E.28})$$

②:

$$\frac{1}{|\Omega^*|} \int_{\Omega^*} \nabla_{\mathbf{x}^*} \cdot (\rho_{i,0}^* \vec{v}_0^*) d\Omega^* \stackrel{\text{with (E.21)}}{=} \nabla_{\mathbf{x}^*} \cdot (\rho_{i,0}^* \langle \vec{v}_0^* \rangle) \quad (\text{E.29})$$

where $\langle \vec{v}_0^* \rangle$ is the Darcy velocity as defined in (E.11).

③:

$$\begin{aligned} & \frac{1}{|\Omega^*|} \int_{\Omega^*} \nabla_{\mathbf{x}^*} \cdot (\vec{J}_{i,0}^*) d\Omega^* \stackrel{\text{with (E.26)}}{=} \nabla_{\mathbf{x}^*} \cdot \left(\frac{1}{|\Omega^*|} \int_{\Omega_f^*} \nabla_{\mathbf{y}^*} \cdot (\mathbf{y}^* \otimes \vec{J}_{i,0}^*) d\Omega^* \right) = \\ & \nabla_{\mathbf{x}^*} \cdot \left(\frac{1}{|\Omega^*|} \left(\int_{S_f^*} (\mathbf{y}^* \otimes \vec{J}_{i,0}^*) \cdot \vec{n} dS^* + \underbrace{\int_{\Gamma} (\mathbf{y}^* \otimes \vec{J}_{i,0}^*) \cdot \vec{n} dS^*}_{=0, (\text{E.19})_2} \right) \right) \stackrel{\text{with (E.27)}}{=} \\ & \nabla_{\mathbf{x}^*} \cdot \left(\frac{1}{|\Omega^*|} \int_{S_f^*} (\mathbf{y}^* \otimes \sum_{j=1}^{n-1} B_{ij,0}^* (\mathbf{I} + \nabla_{\mathbf{y}^*} \otimes \vec{\chi}) \nabla_{\mathbf{x}^*} x_{j,0}^*) \cdot \vec{n} dS^* \right) = \\ & \nabla_{\mathbf{x}^*} \cdot \left(\frac{1}{|\Omega^*|} \int_{S_f^*} \mathbf{y}^* \otimes \left(\sum_{j=1}^{n-1} B_{ij,0}^* (\mathbf{I} + \nabla_{\mathbf{y}^*} \otimes \vec{\chi}) \nabla_{\mathbf{x}^*} x_{j,0}^* \cdot \vec{n} \right) dS^* \right) \stackrel{\text{(E.7), Gauß, (E.26)}}{=} \\ & \nabla_{\mathbf{x}^*} \cdot \left(\sum_{j=1}^{n-1} \langle B_{ij,0}^* \rangle \nabla_{\mathbf{x}^*} x_{j,0}^* \right) = \\ & \nabla_{\mathbf{x}^*} \cdot \langle \vec{J}_{i,0}^* \rangle \end{aligned} \quad (\text{E.30})$$

④:

$$\begin{aligned} & \frac{1}{|\Omega^*|} \int_{\Omega^*} \nabla_{\mathbf{y}^*} \cdot (\rho_{i,0}^* \vec{v}_0^* + \rho_{i,1}^* \vec{v}_1^*) d\Omega^* = \frac{1}{|\Omega^*|} \int_{\partial\Omega_f^*} (\rho_{i,0}^* \vec{v}_0^* + \rho_{i,1}^* \vec{v}_1^*) \cdot \vec{n} dS^* = \\ & \frac{1}{|\Omega^*|} \int_{S_f^*} \underbrace{(\rho_{i,0}^* \vec{v}_0^* + \rho_{i,1}^* \vec{v}_1^*)}_{=0, \Omega^*\text{-periodicity of } \rho_{i,0}^*, \rho_{i,1}^*, \vec{v}_0^*, \vec{v}_1^*} \cdot \vec{n} dS^* + \\ & \frac{1}{|\Omega^*|} \int_{\Gamma^*} \underbrace{(\rho_{i,0}^* \vec{v}_0^* + \rho_{i,1}^* \vec{v}_1^*)}_{=0, \vec{v}_0^*, \vec{v}_1^* = 0 \text{ on } \Gamma^*, (\varepsilon^0), (\varepsilon^1)} \cdot \vec{n} dS^* = 0 \end{aligned} \quad (\text{E.31})$$

⑤:

$$\begin{aligned} & \frac{1}{|\Omega^*|} \int_{\Omega^*} \nabla_{\mathbf{y}^*} \cdot \vec{J}_{i,1}^* d\Omega^* = \frac{1}{|\Omega^*|} \int_{\partial\Omega_f^*} \vec{J}_{i,1}^* \cdot \vec{n} dS^* = \\ & \frac{1}{|\Omega^*|} \int_{S_f^*} \underbrace{\vec{J}_{i,1}^*}_{=0, \Omega^*\text{-periodicity of } \vec{J}_{i,1}^*} \cdot \vec{n} dS^* + \frac{1}{|\Omega^*|} \int_{\Gamma^*} \underbrace{\vec{J}_{i,1}^*}_{=0, (\text{E.25})_2} \cdot \vec{n} dS^* = 0 \end{aligned} \quad (\text{E.32})$$

Ⓒ:

$$\frac{1}{|\Omega^*|} \int_{\Omega^*} r_{i,0}^*(\boldsymbol{\rho}_0^*) d\Omega^* \stackrel{\text{with (E.21)}}{=} \phi r_{i,0}^*(\boldsymbol{\rho}_0^*) \quad (\text{E.33})$$

Summarizing, we obtain the macroscopic equation for gas phase species mass transport through porous media at first order of approximation for $i = 1 \dots n$:

$$\phi \frac{\partial \rho_{i,0}^*}{\partial t^*} + \nabla_{\mathbf{x}^*} \cdot (\rho_{i,0}^* \langle \vec{v}_0^* \rangle + \langle \vec{J}_{i,0}^* \rangle) = \phi r_{i,0}^*(\boldsymbol{\rho}_0^*) \quad \text{in } \Omega^* \quad (\text{MT}_0^*)$$

From (E.30) we obtain the spatially averaged diffusive species mass fluxes

$$\langle \vec{J}_{i,0}^* \rangle = \sum_{j=1}^{n-1} \langle \mathbf{B}_{ij,0}^* \rangle \nabla_{\mathbf{x}^*} x_{j,0}^*. \quad (\text{E.34})$$

Recalling that we rewrote (MT-PS)₃ and (MT-PS)₄ to yield (E.13) at the outset of the derivation we can now rewrite (E.34) again in Maxwell–Stefan formulation for $i = 1 \dots n - 1$:

$$-\sum_{\substack{j=1 \\ j \neq i}}^n x_{i,0}^* x_{j,0}^* \langle \mathbf{D}_{ij,0}^{\text{eff}*} \rangle^{-1} \left(\frac{\langle \vec{J}_{i,0}^* \rangle}{\rho_{i,0}^*} - \frac{\langle \vec{J}_{j,0}^* \rangle}{\rho_{j,0}^*} \right) = \nabla_{\mathbf{x}^*} x_{i,0}^* \quad (\text{E.35})$$

complemented by

$$\sum_{i=1}^n \langle \vec{J}_{i,0}^* \rangle = 0 \quad (\text{E.36})$$

with the effective Maxwell–Stefan diffusivities:

$$\begin{aligned} \langle \mathbf{D}_{ij,0}^{\text{eff}*} \rangle &= \frac{1}{|\Omega^*|} \int_{\Omega^*} \mathbf{D}_{ij,0}^*(\mathbf{I} + \nabla_{\mathbf{y}^*} \otimes \boldsymbol{\chi}) d\Omega^* \\ &= \mathbf{D}_{ij,0}^* \langle \mathbf{I} + \nabla_{\mathbf{y}^*} \otimes \boldsymbol{\chi} \rangle. \end{aligned} \quad (\text{E.37})$$

Here we used the fact that $\mathbf{D}_{ij,0}^*(\mathbf{x}^*) = \mathbf{D}_{ij,0}^*(p_0^*, T_0^*)(\mathbf{x}^*)$ are independent of \mathbf{y}^* as is shown for p_0^* and T_0^* in Appendices E.1 and E.3, respectively.

In dimensional variables we have:

$$\phi \frac{\partial \rho_i}{\partial t} + \nabla_{\mathbf{x}} \cdot (\rho_i \langle \vec{v} \rangle + \langle \vec{J}_i \rangle) = \phi r_i(\boldsymbol{\rho}) + \mathcal{O}(\epsilon) \quad \text{in } \Omega \quad (\text{MT})$$

with the diffusive species mass fluxes in Maxwell–Stefan formulation for $i = 1 \dots n - 1$:

$$-\sum_{\substack{j=1 \\ j \neq i}}^n x_i x_j \langle \mathbf{D}_{ij}^{\text{eff}} \rangle^{-1} \left(\frac{\langle \vec{J}_i \rangle}{\rho_i} - \frac{\langle \vec{J}_j \rangle}{\rho_j} \right) = \nabla_{\mathbf{x}} x_i + \mathcal{O}(\epsilon) \quad (\text{E.38})$$

with the effective Maxwell–Stefan diffusivities

$$\langle \mathbf{D}_{ij}^{\text{eff}} \rangle = \mathbf{D}_{ij} \langle \mathbf{I} + \nabla_{\mathbf{y}} \otimes \boldsymbol{\chi} \rangle + \mathcal{O}(\epsilon) \quad (\text{E.39})$$

where \mathbf{D}_{ij} are the gas phase Maxwell–Stefan diffusivities complemented by

$$\sum_{i=1}^n \langle \vec{J}_i \rangle = \mathcal{O}(\epsilon). \quad (\text{E.40})$$

E.3. Thermal energy transport

In the following, thermal energy (i.e. heat) transport in a porous medium consisting of porous solid phase b and gas phase a saturating the pore space as shown in Fig. E.14 is described. On the pore scale (PS), heat transport in the gas phase occurs via conduction–advection accompanied by heat source originating from bulk chemical reactions as described in (2.20) while in the porous solid phase heat is transported via conduction only. Heat exchange between the gas phase Ω_a and the porous solid phase Ω_b over the boundary Γ is described as proportional to a heat transfer coefficient h and the local difference in temperatures between the phases $T_a - T_b$. Similar treatments are shown in [26,27].

Thus, the pore scale equations for heat transport inside the gas and solid phases Ω_a and Ω_b , formulated in terms of the temperatures of T_a and T_b , respectively, including heat exchange and heat flux continuity on the boundary Γ take the form:

$$\left. \begin{aligned} \frac{\partial}{\partial t} (\rho_a c_a T_a) - \nabla_{\mathbf{x}} \cdot (\lambda_a \nabla_{\mathbf{x}} T_a - \rho_a c_a T_a \vec{v}) &= q_a && \text{in } \Omega_a \\ \frac{\partial}{\partial t} (\rho_b c_b T_b) - \nabla_{\mathbf{x}} \cdot (\lambda_b \nabla_{\mathbf{x}} T_b) &= 0 && \text{in } \Omega_b \\ \vec{n} \cdot (\lambda_b \nabla_{\mathbf{x}} T_b) &= -h(T_a - T_b) && \text{on } \Gamma \\ \vec{n} \cdot (\lambda_a \nabla_{\mathbf{x}} T_a - \lambda_b \nabla_{\mathbf{x}} T_b) &= 0 && \text{on } \Gamma \end{aligned} \right\} \quad (\text{HT-PS})$$

with heat release or consumption from bulk chemical reactions in the gas phase q_a .

Introduce the non-dimensional variables of order $\mathcal{O}(1)$ with superscript $*$ by scaling the dimensional variables with characteristic values:

$$\begin{aligned} \mathbf{X} &= L_c \mathbf{x}^*, & T_a &= T_c T_a^*, & \lambda_a &= \lambda_{ac} \lambda_a^*, & \rho_a &= \rho_{ac} \rho_a^*, & c_a &= c_{ac} c_a^* \\ t &= t_c t^*, & T_b &= T_c T_b^*, & \lambda_b &= \lambda_{bc} \lambda_b^*, & \rho_b &= \rho_{bc} \rho_b^*, & c_b &= c_{bc} c_b^* \\ \vec{v} &= v_c \vec{v}^*, & h &= h_c h^*, & q_a &= \rho_{ac} c_{ac} T_c / t_{Rc} q_a^*, \end{aligned}$$

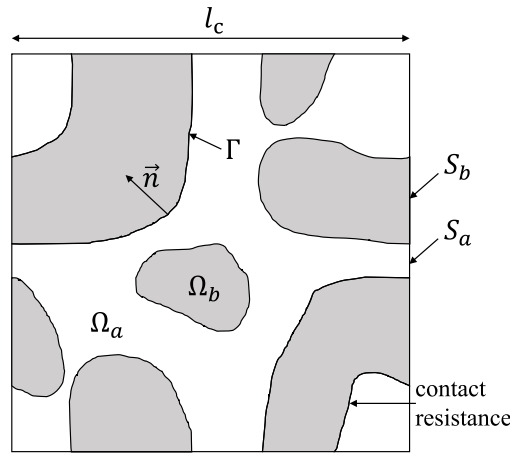


Fig. E.14. Period Ω of porous domain with the gas phase Ω_a and the solid phase Ω_b , considering contact resistance affecting heat exchange between the phases. Source: Reproduced from [26].

Here, t_c is the timescale of transient temperature change in phase a relative to rate of conductive heat transfer in phase a and t_{RC} is the timescale of heat release or consumption by chemical reactions relative to conductive heat transport in phase a .

Based on the characteristic quantities, the following dimensionless numbers can be defined that indicate the relative magnitude of the different terms:

$$\text{Pe}_L = \frac{\rho_{ac} c_{ac} L_c v_c}{\lambda_{ac}}, \quad \mathcal{L} = \frac{\lambda_{bc}}{\lambda_{ac}}, \quad \mathcal{P}_L = \frac{\rho_{ac} c_{ac} L_c^2}{\lambda_{ac} t_c}, \quad C = \frac{\rho_{bc} c_{bc}}{\rho_{ac} c_{ac}}, \quad \text{Bi}_L = \frac{h_c L_c}{\lambda_{bc}},$$

$$\mathcal{T} = \frac{t_c}{t_{RC}}$$

The boundary value problem (HT-PS) can thus be rewritten with dimensionless variables in terms of the dimensionless numbers:

$$\left. \begin{aligned} & \mathcal{P}_L \frac{\partial}{\partial t^*} (\rho_a^* c_a^* T_a^*) \\ & -\nabla_{\mathbf{x}^*} \cdot (\lambda_a^* \nabla_{\mathbf{x}^*} T_a^* - \text{Pe}_L \rho_a^* c_a^* T_a^* \vec{v}^*) = \mathcal{P}_L \mathcal{T} q_a^* & \text{in } \Omega_a^* \\ & C \mathcal{P}_L \frac{\partial}{\partial t^*} (\rho_b^* c_b^* T_b^*) - \mathcal{L} \nabla_{\mathbf{x}^*} \cdot (\lambda_b^* \nabla_{\mathbf{x}^*} T_b^*) = 0 & \text{in } \Omega_b^* \\ & (1/\mathcal{L}) \vec{n} \cdot (\lambda_a^* \nabla_{\mathbf{x}^*} T_a^*) = -\text{Bi}_L h^* (T_a^* - T_b^*) & \text{on } \Gamma^* \\ & \vec{n} \cdot (\lambda_a^* \nabla_{\mathbf{x}^*} T_a^* - \mathcal{L} \lambda_b^* \nabla_{\mathbf{x}^*} T_b^*) = 0 & \text{on } \Gamma^* \end{aligned} \right\} \quad (\text{HT-PS}^*)$$

Physical arguments and equation scaling

In the following the magnitude of the dimensionless numbers that quantify the relative magnitude and thus importance of different processes are discussed based on physical arguments in connection with the application of interest. The dimensionless numbers presented herein are discussed in the computational notebook ‘‘PTReactorDemo.jl’’.

The Peclet number $\text{Pe}_L = \mathcal{O}(1)$ is computed on the one hand from the gas flow rate and thus the advective flow velocity that is specified as part of the experimental conditions and on the other hand from the density and thermal properties of the gas phase.

The ratio of thermal conductivities $\mathcal{L} = \mathcal{O}(\varepsilon^{-1})$ follows from the fact that the solid phase b has a thermal conductivity λ_{bc} that is roughly one order of magnitude larger than that of the gas phase a , λ_{ac} .

The dimensionless number $\mathcal{P}_L = \mathcal{O}(\varepsilon^2)$ quantifies the ratio of thermal power to overcome thermal inertia in a transient setting to the conductive heat transport rate in phase a . In our application, we are interested in stationary solutions or slowly-varying solutions approaching the stationary solution, such that large values for the characteristic time t_c are chosen leading to a small value for \mathcal{P}_L .

To estimate \mathcal{T} we begin by writing t_c , the timescale of transient temperature change in phase a relative to rate of conductive heat transfer in phase a as $t_c = \rho_{ac} c_{ac} L_c^2 / \lambda_{ac} \mathcal{P}_L^{-1}$. To estimate t_{RC} , the timescale of heat release or consumption by chemical reactions relative to conductive heat transport in phase a , we assume, that the rate of heat release or consumption by reaction is of same magnitude than the rate of conductive heat transport in phase a expressed by $|q_a| \approx |\nabla_{\mathbf{x}^*} \cdot (\lambda_a^* \nabla_{\mathbf{x}^*} T_a^*)|$. We can then write $t_{RC} = \rho_{ac} c_{ac} L_c^2 / \lambda_{ac}$ and thus obtain for $\mathcal{T} = \frac{t_c}{t_{RC}} = \mathcal{P}_L^{-1} = \mathcal{O}(\varepsilon^{-2})$.

The ratio of the volumetric heat capacities $C = \mathcal{O}(\varepsilon^{-2})$ follows from the fact that phase a is a gas while phase b is a solid with a density that is roughly three orders of magnitude larger than that of phase a .

The Biot number $\text{Bi}_L = \mathcal{O}(\varepsilon^{-1})$ accounts for the ratio of interfacial heat transfer to thermal conductivity in the solid phase and in the present case is evaluated with an interfacial heat transfer coefficient computed according to [59] and the thermal conductivity of the material of the solid phase.

Homogenization ansatz

The homogenization ansatz we use relies on asymptotic expansions with different orders of the scale separation parameter written in the two-scale coordinates $(\mathbf{x}^*, \mathbf{y}^*)$ with $\mathbf{y}^* = \varepsilon^{-1} \mathbf{x}^*$ for the dimensionless quantities T_a^* , ρ_a^* , \vec{v}^* , T_b^* , where functions T_a^* , T_b^* are periodic in \mathbf{y}^* analogous to (E.3). The dimensionless physical properties of gas phase a , thermal conductivity λ_a^* and heat capacity c_a^* are approximated to the first order by $\lambda_a^* = \lambda_{a,0}^*(T_{a,0}^*)$, $c_a^* = c_{a,0}^*(T_{a,0}^*)$ while the physical properties of solid phase b , λ_b^* , ρ_b^* and c_b^* are considered constant.

Further, we apply Taylor series expansion of the dimensionless heat release from bulk chemical reactions in the gas phase $q_a^* = q_a^*(T_a^*)$ around the support point $T_{a,0}^*$, truncated after the first term. Assuming q_a^* is at least once differentiable in the neighborhood of the support point, the total differential of q_a^* , dq_a^* can be written as:

$$dq_a^*(T_a^*) = \frac{\partial dq_a^*}{\partial T_a^*} dT_a^*$$

Then, the Taylor series approximation developed around $T_{a,0}^*$ truncated after the first term with $dT_a^* = T_a^* - T_{a,0}^*$ takes the form:

$$\begin{aligned} q_a^*(T_a^*) &= q_a^*(T_{a,0}^*) + dq_a^*(T_{a,0}^*) + \mathcal{O}(\varepsilon^2) \\ &= q_a^*(T_{a,0}^*) + \varepsilon \frac{\partial q_a^*}{\partial T_{a,0}^*} T_{a,1}^* + \mathcal{O}(\varepsilon^2) \\ &= q_{a,0}^*(T_{a,0}^*) + \varepsilon q_{a,1}^*(T_{a,1}^*) + \mathcal{O}(\varepsilon^2) \end{aligned}$$

The change of independent variable necessitates the following transformation of the derivative operator: $\nabla_{\mathbf{x}} \rightarrow \nabla_{\mathbf{x}^*} + \varepsilon^{-1} \nabla_{\mathbf{y}^*}$. Inserting the ansatz functions into (HT-PS*) considering the transformed differential operators we obtain:

$$\begin{aligned} &\varepsilon^2 \frac{\partial}{\partial t^*} \left(c_a^*(\rho_{a,0}^* + \varepsilon \rho_{a,1}^* + \varepsilon^2 \rho_{a,2}^*)(T_{a,0}^* + \varepsilon T_{a,1}^* + \varepsilon^2 T_{a,2}^*) \right) - (\nabla_{\mathbf{x}^*} + \varepsilon^{-1} \nabla_{\mathbf{y}^*}) \cdot \\ &\left(\lambda_{a,0}^*(\nabla_{\mathbf{x}^*} + \varepsilon^{-1} \nabla_{\mathbf{y}^*})(T_{a,0}^* + \varepsilon T_{a,1}^* + \varepsilon^2 T_{a,2}^*) \right. \\ &\left. - c_a^*(\rho_{a,0}^* + \varepsilon \rho_{a,1}^* + \varepsilon^2 \rho_{a,2}^*)(T_{a,0}^* + \varepsilon T_{a,1}^* + \varepsilon^2 T_{a,2}^*)(\vec{v}_0^* + \varepsilon \vec{v}_1^* + \varepsilon^2 \vec{v}_2^*) \right) = \\ &q_{a,0}^*(T_{a,0}^*) + \varepsilon q_{a,1}^*(T_{a,1}^*) + \mathcal{O}(\varepsilon^2) \quad \text{in } \Omega_a^* \end{aligned} \quad (\text{E.41})$$

$$\begin{aligned} &\frac{\partial}{\partial t^*} \left(\rho_b^* c_b^*(T_{b,0}^* + \varepsilon T_{b,1}^* + \varepsilon^2 T_{b,2}^*) \right) - \varepsilon^{-1} (\nabla_{\mathbf{x}^*} + \varepsilon^{-1} \nabla_{\mathbf{y}^*}) \cdot \\ &\left(\lambda_b^*(\nabla_{\mathbf{x}^*} + \varepsilon^{-1} \nabla_{\mathbf{y}^*})(T_{b,0}^* + \varepsilon T_{b,1}^* + \varepsilon^2 T_{b,2}^*) \right) = 0 \quad \text{in } \Omega_b^* \end{aligned} \quad (\text{E.42})$$

$$\begin{aligned} &\varepsilon \vec{n} \cdot \left(\lambda_{a,0}^*(\nabla_{\mathbf{x}^*} + \varepsilon^{-1} \nabla_{\mathbf{y}^*})(T_{a,0}^* + \varepsilon T_{a,1}^* + \varepsilon^2 T_{a,2}^*) \right) = \\ &-\varepsilon^{-1} h^*(T_{a,0}^* + \varepsilon T_{a,1}^* + \varepsilon^2 T_{a,2}^* - T_{b,0}^* - \varepsilon T_{b,1}^* - \varepsilon^2 T_{b,2}^*) \quad \text{on } \Gamma^* \end{aligned} \quad (\text{E.43})$$

$$\begin{aligned} &\vec{n} \cdot \left(\lambda_{a,0}^*(\nabla_{\mathbf{x}^*} + \varepsilon^{-1} \nabla_{\mathbf{y}^*})(T_{a,0}^* + \varepsilon T_{a,1}^* + \varepsilon^2 T_{a,2}^*) \right) = \\ &\vec{n} \cdot \left(\varepsilon^{-1} \lambda_b^*(\nabla_{\mathbf{x}^*} + \varepsilon^{-1} \nabla_{\mathbf{y}^*})(T_{b,0}^* + \varepsilon T_{b,1}^* + \varepsilon^2 T_{b,2}^*) \right) \quad \text{on } \Gamma^* \end{aligned} \quad (\text{E.44})$$

Consecutively, for each equation in (E.41)–(E.44), we consider terms of increasing order in ε . Therefore, from (E.41), with order ε^{-2} we get:

$$\nabla_{\mathbf{y}^*} \cdot \left(\underbrace{\lambda_{a,0}^*}_{>0} \nabla_{\mathbf{y}^*} T_{a,0}^* \right) = 0 \quad \text{in } \Omega_a^* \quad (\text{E.45})$$

From (E.42) for order ε^{-3} we get analogously:

$$\nabla_{\mathbf{y}^*} \cdot \left(\underbrace{\lambda_b^*}_{>0} \nabla_{\mathbf{y}^*} T_{b,0}^* \right) = 0 \quad \text{in } \Omega_b^* \quad (\text{E.46})$$

Scaling both sides of the heat transfer boundary condition between the phases (E.43) by ε^{-1} yields the equivalent expression:

$$\begin{aligned} &\vec{n} \cdot \left(\lambda_{a,0}^*(\nabla_{\mathbf{x}^*} + \varepsilon^{-1} \nabla_{\mathbf{y}^*})(T_{a,0}^* + \varepsilon T_{a,1}^* + \varepsilon^2 T_{a,2}^*) \right) = \\ &-\varepsilon^{-2} h^*(T_{a,0}^* + \varepsilon T_{a,1}^* + \varepsilon^2 T_{a,2}^* - T_{b,0}^* - \varepsilon T_{b,1}^* - \varepsilon^2 T_{b,2}^*) \quad \text{on } \Gamma^* \end{aligned} \quad (\widetilde{\text{E.43}})$$

From (E.43) we can directly see that for order ε^{-2} we have:

$$\underbrace{h^*}_{>0} (T_{a,0}^* - T_{b,0}^*) = 0 \implies T_{a,0}^* = T_{b,0}^* \quad \text{on } \Gamma^* \quad (\text{E.47})$$

Also for order ε^{-2} we get from the heat flux continuity boundary condition between the phases (E.44):

$$\vec{n} \cdot \left(\underbrace{\lambda_b^*}_{>0} \nabla_{\mathbf{y}^*} T_{b,0}^* \right) = 0 \implies \nabla_{\mathbf{y}^*} T_{b,0}^* = 0 \quad \text{on } \Gamma^* \quad (\text{E.48})$$

Eqs. (E.46) and (E.48) form a boundary value problem for $T_{b,0}^*$ whose solution has the form:

$$T_{b,0}^*(\mathbf{x}^*, \mathbf{y}^*) = T_{b,0}^*(\mathbf{x}^*). \quad (\text{E.49})$$

Similarly, by combining (E.45), (E.47) and (E.48) we can deduce for $T_{a,0}^*$ at order ε^{-2} :

$$T_{a,0}^*(\mathbf{x}^*, \mathbf{y}^*) = T_{b,0}^*(\mathbf{x}^*) = T_0^*(\mathbf{x}^*) \quad \text{in } \Omega_a^* \cup \Omega_b^* \quad (\text{E.50})$$

In other words, to first order of approximation, the temperature is constant across the period Ω^* .

For (E.41) the next higher order is ε^{-1} and with (E.50) and $(\bar{\varepsilon}^0)_2$ from Appendix E.1 it yields:

$$\begin{aligned} & \nabla_{\mathbf{x}^*} \cdot (\lambda_{a,0}^* \underbrace{\nabla_{\mathbf{y}^*} T_{a,0}^*}_{=0}) \\ & + \nabla_{\mathbf{y}^*} \cdot (\lambda_{a,0}^* (\nabla_{\mathbf{x}^*} T_{a,0}^* + \nabla_{\mathbf{y}^*} T_{a,1}^*) - \rho_{a,0}^* c_{a,0}^* \bar{v}_0^* T_{a,0}^*) = \\ & \nabla_{\mathbf{y}^*} \cdot (\lambda_{a,0}^* (\nabla_{\mathbf{x}^*} T_{a,0}^* + \nabla_{\mathbf{y}^*} T_{a,1}^*)) \\ & - c_{a,0}^* (\underbrace{(\nabla_{\mathbf{y}^*} \cdot (\rho_{a,0}^* \bar{v}_0^*))}_{=0} T_{a,0}^* + (\rho_{a,0}^* \bar{v}_0^*) \cdot \underbrace{\nabla_{\mathbf{y}^*} T_{a,0}^*}_{=0}) = \end{aligned} \tag{E.51}$$

Similarly, the terms of order ε^{-2} for (E.42) under consideration of (E.49) lead to:

$$\nabla_{\mathbf{x}^*} \cdot (\lambda_b^* \underbrace{\nabla_{\mathbf{y}^*} T_{b,0}^*}_{=0}) + \nabla_{\mathbf{y}^*} \cdot (\lambda_b^* (\nabla_{\mathbf{x}^*} T_{b,0}^* + \nabla_{\mathbf{y}^*} T_{b,1}^*)) = 0 \quad \text{in } \Omega_b^* \tag{E.52}$$

For order ε^{-1} in (E.43), which corresponds to order ε^0 in (E.43), we get:

$$\bar{n} \cdot (\lambda_a^* \underbrace{\nabla_{\mathbf{y}^*} T_{a,0}^*}_{=0 \text{ (E.50)}}) = \underbrace{h^*}_{>0} (T_{a,1}^* - T_{b,1}^*) \implies T_{a,1}^* = T_{b,1}^* \quad \text{on } \Gamma^* \tag{E.53}$$

In the same way we get for order ε^{-1} in (E.44):

$$\bar{n} \cdot (\lambda_a^* \underbrace{\nabla_{\mathbf{y}^*} T_{a,0}^*}_{=0 \text{ (E.50)}}) = \bar{n} \cdot (\lambda_b^* (\nabla_{\mathbf{x}^*} T_{b,0}^* + \nabla_{\mathbf{y}^*} T_{b,1}^*)) \quad \text{on } \Gamma^* \tag{E.54}$$

Taken together, (E.52) and (E.54) form a boundary value problem for $\lambda_b^* (\nabla_{\mathbf{x}^*} T_{b,0}^* + \nabla_{\mathbf{y}^*} T_{b,1}^*)$ with the solution

$$\underbrace{\lambda_b^* (\nabla_{\mathbf{x}^*} T_{b,0}^* + \nabla_{\mathbf{y}^*} T_{b,1}^*)}_{>0} = \bar{0} \quad \text{in } \Omega_b^* \tag{E.55}$$

From (E.55) we can see that a solution for $T_{b,1}^*$ is:

$$T_{b,1}^*(\mathbf{x}^*, \mathbf{y}^*) = -\mathbf{y}^* \cdot \nabla_{\mathbf{x}^*} T_{b,0}^* + \bar{T}_{b,1}^*(\mathbf{x}^*) \tag{E.56}$$

where $\bar{T}_{b,1}^*(\mathbf{x}^*)$ is an arbitrary function of \mathbf{x}^* .

We now seek expressions for the field $T_{a,1}^*$ in terms of $T_{a,0}^*$. We begin by rewriting $\nabla_{\mathbf{x}^*} T_{a,0}^*$ and by further assuming that the functional form of the Ω^* -periodic field $T_{a,1}^*$ can be represented as a linear combination in terms of $\nabla_{\mathbf{x}^*} T_{a,0}^*$:

$$\nabla_{\mathbf{x}^*} T_{a,0}^* = \sum_{k=1}^d \frac{\partial T_{a,0}^*}{\partial x_k^*}(\mathbf{x}^*) \bar{e}_k \tag{E.57}$$

$$T_{a,1}^*(\mathbf{x}^*, \mathbf{y}^*) = \sum_{k=1}^d \frac{\partial T_{a,0}^*}{\partial x_k^*}(\mathbf{x}^*) t_{a,k}(\mathbf{y}^*) \tag{E.58}$$

Upon inserting (E.57), (E.58) into (E.51), (E.53) and factoring out the terms which are constant with respect to \mathbf{y}^* we obtain the cell problems in the form of boundary value problems for the Ω^* -periodic functions $t_{a,k}$. The cell problems for each spatial dimension $k = 1, \dots, d$ can thus be formulated:

$$\left. \begin{aligned} \nabla_{\mathbf{y}^*} \cdot (\lambda_{a,0}^* (\bar{e}_k + \nabla_{\mathbf{y}^*} t_{a,k})) &= 0 \quad \text{in } \Omega_a^* \\ t_{a,k} - y_k^* &= 0 \quad \text{on } \Gamma^* \\ \int_{\Omega_a^*} t_{a,k} d\Omega^* &= 0 \quad \text{in } \Omega_a^* \end{aligned} \right\} \tag{HT}_k$$

We require a vanishing mean value for $t_{a,k}$ when integrating over the period $\Omega^*(\text{HT}_k)_3$. We can write $t_{a,k}$, $j = k, \dots, d$, where d is the spatial problem dimension, more compactly in vector form:

$$\begin{aligned} \bar{t}_a &= \sum_{k=1}^d t_{a,k} \bar{e}_k \\ \nabla_{\mathbf{y}^*} T_{a,1}^* &= \nabla_{\mathbf{y}^*} \sum_{k=1}^d \frac{\partial T_{a,0}^*}{\partial x_k^*} t_{a,k} = \sum_{k=1}^d \frac{\partial T_{a,0}^*}{\partial x_k^*} \nabla_{\mathbf{y}^*} t_{a,k} \end{aligned}$$

And thus:

$$\nabla_{\mathbf{x}^*} T_{a,0}^* + \nabla_{\mathbf{y}^*} T_{a,1}^* = (\mathbf{I} + \nabla_{\mathbf{y}^*} \otimes \bar{t}_a) \nabla_{\mathbf{x}^*} T_{a,0}^* \tag{E.59}$$

For the next higher order corresponding to ε^0 for (E.41) we get:

$$\begin{aligned} \nabla_{\mathbf{x}^*} \cdot (c_{a,0}^* T_{a,0}^* \rho_{a,0}^* \bar{v}_0^*) + \nabla_{\mathbf{y}^*} \cdot (c_{a,0}^* (T_{a,0}^* (\rho_{a,0}^* \bar{v}_1^* + \rho_{a,1}^* \bar{v}_0^*) + T_{a,1}^* \rho_{a,0}^* \bar{v}_0^*)) \\ - \nabla_{\mathbf{x}^*} \cdot (\lambda_{a,0}^* (\nabla_{\mathbf{x}^*} T_{a,0}^* + \nabla_{\mathbf{y}^*} T_{a,1}^*)) - \nabla_{\mathbf{y}^*} \cdot (\lambda_{a,0}^* (\nabla_{\mathbf{x}^*} T_{a,1}^* + \nabla_{\mathbf{y}^*} T_{a,2}^*)) &= q_{a,0}^* \quad \text{in } \Omega_a^* \end{aligned} \tag{E.60}$$

An intermediate result that will be used later can be obtained from the order ε^{-1} for (E.42):

$$-\nabla_{\mathbf{x}^*} \cdot (\underbrace{\lambda_b^* (\nabla_{\mathbf{x}^*} T_{b,0}^* + \nabla_{\mathbf{y}^*} T_{b,1}^*)}_{=0, \text{ (E.55)}})$$

$$-\nabla_{\mathbf{y}^*} \cdot (\lambda_b^* (\nabla_{\mathbf{x}^*} T_{b,1}^* + \nabla_{\mathbf{y}^*} T_{b,2}^*)) = 0 \quad \text{in } \Omega_b^* \tag{E.61}$$

For order ϵ^0 for (E.42) we get:

$$\begin{aligned} \frac{\partial}{\partial t^*} (\rho_b^* c_b^* T_{b,0}^*) - \nabla_{\mathbf{x}^*} \cdot (\lambda_b^* (\nabla_{\mathbf{x}^*} T_{b,1}^* + \nabla_{\mathbf{y}^*} T_{b,2}^*)) \\ - \nabla_{\mathbf{y}^*} \cdot (\lambda_b^* (\nabla_{\mathbf{x}^*} T_{b,2}^* + \nabla_{\mathbf{y}^*} T_{b,3}^*)) = 0 \quad \text{in } \Omega_b^* \end{aligned} \tag{E.62}$$

For convenience, we introduce the heat fluxes through each phase:

$$\begin{aligned} q_a^* &= \lambda_a^* (\nabla_{\mathbf{x}^*} T_{a,0}^* + \nabla_{\mathbf{y}^*} T_{a,1}^*) \\ &= \lambda_a^* (\mathbf{I} + \nabla_{\mathbf{y}^*} \otimes \vec{t}_a) \nabla_{\mathbf{x}^*} T_{a,0}^* \end{aligned} \tag{E.63}$$

$$q_b^* = \lambda_b^* (\nabla_{\mathbf{x}^*} T_{b,1}^* + \nabla_{\mathbf{y}^*} T_{b,2}^*) \tag{E.64}$$

for which it holds due to (E.51) and (E.61):

$$q_a^* = \nabla_{\mathbf{y}^*} \cdot (\mathbf{y}^* \otimes q_a^*) \tag{E.65}$$

$$q_b^* = \nabla_{\mathbf{y}^*} \cdot (\mathbf{y}^* \otimes q_b^*) \tag{E.66}$$

As they will be used in later steps, the expressions obtained from the heat flux continuity boundary condition (E.44) of order ϵ^0 and ϵ^1 are:

$$\underbrace{\vec{n} \cdot (\lambda_{a,0}^* (\nabla_{\mathbf{x}^*} T_{a,0}^* + \nabla_{\mathbf{y}^*} T_{a,1}^*))}_{q_a^*} = \underbrace{\vec{n} \cdot (\lambda_b^* (\nabla_{\mathbf{x}^*} T_{b,1}^* + \nabla_{\mathbf{y}^*} T_{b,2}^*))}_{q_b^*} \quad \text{on } \Gamma^* \tag{E.67}$$

and

$$\vec{n} \cdot (\lambda_{a,0}^* (\nabla_{\mathbf{x}^*} T_{a,1}^* + \nabla_{\mathbf{y}^*} T_{a,2}^*)) = \vec{n} \cdot (\lambda_b^* (\nabla_{\mathbf{x}^*} T_{b,2}^* + \nabla_{\mathbf{y}^*} T_{b,3}^*)) \quad \text{on } \Gamma^* \tag{E.68}$$

respectively.

Summarizing, the following boundary value problem at order ϵ^0 for the Ω^* -periodic fields $T_{a,0}^*, T_{a,1}^*, T_{a,2}^*$ and $T_{b,0}^*, T_{b,1}^*, T_{b,2}^*$ is obtained from (E.60), (E.62), (E.53) and (E.67):

$$\begin{aligned} &\underbrace{\nabla_{\mathbf{x}^*} \cdot (c_{a,0}^* T_{a,0}^* \rho_{a,0}^* \vec{v}_0^*)}_{\textcircled{1}} + \underbrace{\nabla_{\mathbf{y}^*} \cdot (c_{a,0}^* (T_{a,0}^* (\rho_{a,0}^* \vec{v}_1^* + \rho_{a,1}^* \vec{v}_0^*) + T_{a,1}^* \rho_{a,0}^* \vec{v}_0^*))}_{\textcircled{2}} \\ &- \underbrace{\nabla_{\mathbf{x}^*} \cdot (\lambda_{a,0}^* (\nabla_{\mathbf{x}^*} T_{a,0}^* + \nabla_{\mathbf{y}^*} T_{a,1}^*))}_{\textcircled{3}} - \underbrace{\nabla_{\mathbf{y}^*} \cdot (\lambda_{a,0}^* (\nabla_{\mathbf{x}^*} T_{a,1}^* + \nabla_{\mathbf{y}^*} T_{a,2}^*))}_{\textcircled{4}} = \underbrace{q_{a,0}^*}_{\textcircled{5}} \\ &\text{in } \Omega_a^* \\ &\underbrace{\frac{\partial}{\partial t^*} (\rho_b^* c_b^* T_{b,0}^*)}_{\textcircled{6}} - \underbrace{\nabla_{\mathbf{x}^*} \cdot (\lambda_b^* (\nabla_{\mathbf{x}^*} T_{b,1}^* + \nabla_{\mathbf{y}^*} T_{b,2}^*))}_{\textcircled{7}} \\ &- \underbrace{\nabla_{\mathbf{y}^*} \cdot (\lambda_b^* (\nabla_{\mathbf{x}^*} T_{b,2}^* + \nabla_{\mathbf{y}^*} T_{b,3}^*))}_{\textcircled{8}} = 0 \quad \text{in } \Omega_b^* \\ &T_{a,1}^* - T_{b,1}^* = 0 \quad \text{on } \Gamma^* \\ &\vec{n} \cdot (\lambda_{a,0}^* (\nabla_{\mathbf{x}^*} T_{a,0}^* + \nabla_{\mathbf{y}^*} T_{a,1}^*)) = \vec{n} \cdot (\lambda_b^* (\nabla_{\mathbf{x}^*} T_{b,1}^* + \nabla_{\mathbf{y}^*} T_{b,2}^*)) \quad \text{on } \Gamma^* \end{aligned}$$

For the macroscopic equations we integrate over the period $\Omega^* = \Omega_a^* \cup \Omega_b^*$ with $|\Omega^*| = |\Omega_a^*| + |\Omega_b^*|$. Here we introduce the porosity or void fraction $\phi = |\Omega_a^*|/|\Omega^*|$ which is the volume occupied by the gas phase $|\Omega_a^*|$ divided by the total volume $|\Omega^*|$. The solid fraction thus becomes $|\Omega_b^*|/|\Omega^*| = 1 - \phi$. The sections on the boundary of the period belonging to either the fluid or solid phase, S_a^* or S_b^* are defined as $S_a^* = \Omega_a^* \cap \partial\Omega^*$ and $S_b^* = \Omega_b^* \cap \partial\Omega^*$, respectively as shown in Fig. E.14. We make use of the Gauß divergence theorem, the Ω^* -periodicity of the fields that depend on the microscopic variable \mathbf{y}^* and the volumetric averaging operator (E.7). We recall that \vec{n} is the unit normal pointing out of Ω_a^* , so that $(\vec{n} dS_a)_{\Gamma^*} = -(\vec{n} dS_b)_{\Gamma^*}$ holds.

Further, proceed on a term by term basis: $\textcircled{1}$:

$$\frac{1}{|\Omega^*|} \int_{\Omega^*} \nabla_{\mathbf{x}^*} \cdot (c_{a,0}^* T_{a,0}^* \rho_{a,0}^* \vec{v}_0^*) d\Omega^* \stackrel{\text{with (E.50)}}{=} \nabla_{\mathbf{x}^*} \cdot (c_a^* \rho_{a,0}^* T_0^* \langle \vec{v}_0^* \rangle)$$

where $\langle \vec{v}_0^* \rangle$ is the Darcy velocity as defined in (E.11).

$\textcircled{2}$:

$$\begin{aligned} &\frac{1}{|\Omega^*|} \int_{\Omega^*} \nabla_{\mathbf{y}^*} \cdot (c_{a,0}^* (T_{a,0}^* (\rho_{a,0}^* \vec{v}_1^* + \rho_{a,1}^* \vec{v}_0^*) + T_{a,1}^* \rho_{a,0}^* \vec{v}_0^*)) d\Omega^* = \\ &\frac{1}{|\Omega^*|} \int_{\partial\Omega^*} (c_{a,0}^* (T_{a,0}^* (\rho_{a,0}^* \vec{v}_1^* + \rho_{a,1}^* \vec{v}_0^*) + T_{a,1}^* \rho_{a,0}^* \vec{v}_0^*)) \cdot \vec{n} dS^* = \\ &\frac{1}{|\Omega^*|} \int_{S_a^*} (c_{a,0}^* (T_{a,0}^* (\rho_{a,0}^* \vec{v}_1^* + \rho_{a,1}^* \vec{v}_0^*) + T_{a,1}^* \rho_{a,0}^* \vec{v}_0^*)) \cdot \vec{n} dS^* + \\ &\quad = 0, \Omega^*\text{-periodicity of } T_{a,0}^*, T_{a,1}^*, \rho_{a,0}^*, \rho_{a,1}^*, \vec{v}_0^*, \vec{v}_1^* \end{aligned}$$

$$\begin{aligned}
& \frac{1}{|\Omega^*|} \int_{\Gamma^*} \left(c_{a,0}^* (T_{a,0}^* (\rho_{a,0}^* \vec{v}_1^* + \rho_{a,1}^* \vec{v}_0^*) + T_{a,1}^* \rho_{a,0}^* \vec{v}_0^*) \right) \cdot \vec{n} dS^* = 0 \\
& \quad = 0, \vec{v}_0^*, \vec{v}_1^* = 0 \text{ on } \Gamma^*, (\epsilon^0), (\epsilon^1) \\
\textcircled{3} + \textcircled{7}: \\
& - \frac{1}{|\Omega^*|} \int_{\Omega^*} \nabla_{\mathbf{x}^*} \cdot \underbrace{(\lambda_{a,0}^* (\nabla_{\mathbf{x}^*} T_{a,0}^* + \nabla_{\mathbf{y}^*} T_{a,1}^*))}_{q_a^*} d\Omega^* \\
& - \frac{1}{|\Omega^*|} \int_{\Omega^*} \nabla_{\mathbf{x}^*} \cdot \underbrace{(\lambda_b^* (\nabla_{\mathbf{x}^*} T_{b,1}^* + \nabla_{\mathbf{y}^*} T_{b,2}^*))}_{q_b^*} d\Omega^* \stackrel{\text{with (E.65),(E.66)}}{=} \\
& - \frac{1}{|\Omega^*|} \nabla_{\mathbf{x}^*} \cdot \left(\int_{S_a^*} (\mathbf{y}^* \otimes q_a^*) \cdot \vec{n} dS^* + \int_{\Gamma^*} (\mathbf{y}^* \otimes q_a^*) \cdot \vec{n} dS^* \right) \\
& \quad \text{cancel out with (E.67)} \\
& - \frac{1}{|\Omega^*|} \nabla_{\mathbf{x}^*} \cdot \left(\int_{S_b^*} (\mathbf{y}^* \otimes q_b^*) \cdot \vec{n} dS^* - \int_{\Gamma^*} (\mathbf{y}^* \otimes q_b^*) \cdot \vec{n} dS^* \right) \stackrel{\text{with (E.63)}}{=} \\
& \quad = 0, \Omega^*\text{-periodicity of } T_{b,1}^*, T_{b,2}^* \quad \text{cancel out with (E.67)} \\
& - \nabla_{\mathbf{x}^*} \cdot \left(\frac{1}{|\Omega^*|} \int_{S_a^*} \lambda_{a,0}^* (\mathbf{y}^* \otimes (\mathbf{I} + \nabla_{\mathbf{y}^*} \otimes \vec{t}_a)) \cdot \vec{n} dS^* \nabla_{\mathbf{x}^*} T_{a,0}^* \right) \stackrel{\text{with (E.50)}}{=} \\
& \quad = \lambda_0^{\text{eff}^*} \\
& - \nabla_{\mathbf{x}^*} \cdot ((\lambda_0^{\text{eff}^*}) \nabla_{\mathbf{x}^*} T_0^*) \\
\textcircled{4} + \textcircled{8}: \\
& - \frac{1}{|\Omega^*|} \int_{\Omega^*} \nabla_{\mathbf{y}^*} \cdot (\lambda_{a,0}^* (\nabla_{\mathbf{x}^*} T_{a,1}^* + \nabla_{\mathbf{y}^*} T_{a,2}^*)) d\Omega^* \\
& - \frac{1}{|\Omega^*|} \int_{\Omega^*} \nabla_{\mathbf{y}^*} \cdot (\lambda_b^* (\nabla_{\mathbf{x}^*} T_{b,2}^* + \nabla_{\mathbf{y}^*} T_{b,3}^*)) d\Omega^* = \\
& - \frac{1}{|\Omega^*|} \left(\int_{S_a^*} \underbrace{(\lambda_{a,0}^* (\nabla_{\mathbf{x}^*} T_{a,1}^* + \nabla_{\mathbf{y}^*} T_{a,2}^*))}_{=0, \Omega^*\text{-periodicity of } T_{a,1}^*, T_{a,2}^*} \cdot \vec{n} dS^* + \int_{\Gamma^*} \underbrace{(\lambda_{a,0}^* (\nabla_{\mathbf{x}^*} T_{a,1}^* + \nabla_{\mathbf{y}^*} T_{a,2}^*))}_{\text{cancel out with (E.68)}} \cdot \vec{n} dS^* \right) \\
& - \frac{1}{|\Omega^*|} \left(- \int_{S_b^*} \underbrace{(\lambda_b^* (\nabla_{\mathbf{x}^*} T_{b,2}^* + \nabla_{\mathbf{y}^*} T_{b,3}^*))}_{=0, \Omega^*\text{-periodicity of } T_{b,2}^*, T_{b,3}^*} \cdot \vec{n} dS^* - \int_{\Gamma^*} \underbrace{(\lambda_b^* (\nabla_{\mathbf{x}^*} T_{b,2}^* + \nabla_{\mathbf{y}^*} T_{b,3}^*))}_{\text{cancel out with (E.68)}} \cdot \vec{n} dS^* \right) = 0 \\
\textcircled{5}: \\
& \frac{1}{|\Omega^*|} \int_{\Omega^*} q_{a,0}^* (T_{a,0}^*) d\Omega^* \stackrel{\text{with (E.50)}}{=} \phi q_{a,0}^* (T_0^*) \\
\textcircled{6}: \\
& \frac{1}{|\Omega^*|} \int_{\Omega^*} \frac{\partial}{\partial t^*} (\rho_b^* c_b^* T_{b,0}^*) d\Omega^* \stackrel{\text{with (E.50)}}{=} (1 - \phi) \rho_b^* c_b^* \frac{\partial T_0^*}{\partial t^*}
\end{aligned}$$

Summarizing, we obtain the macroscopic equation for thermal energy (heat) transport through porous media at first order of approximation:

$$(1 - \phi) \rho_b^* c_b^* \frac{\partial T_0^*}{\partial t^*} + \nabla_{\mathbf{x}^*} \cdot (c_a^* \rho_{a,0}^* T_0^* \langle \vec{v}_0^* \rangle) - \nabla_{\mathbf{x}^*} \cdot ((\lambda_0^{\text{eff}^*}) \nabla_{\mathbf{x}^*} T_0^*) = \phi q_{a,0}^* \quad \text{in } \Omega^* \quad (\text{HT}_0^*)$$

with the effective, non-dimensional thermal conductivity (λ^{eff^*}) to first order of approximation:

$$\langle \lambda_0^{\text{eff}^*} \rangle = \frac{1}{|\Omega^*|} \int_{S_a^*} \lambda_{a,0}^* (\mathbf{y}^* \otimes (\mathbf{I} + \nabla_{\mathbf{y}^*} \otimes \vec{t}_a)) \cdot \vec{n} dS^* \quad (\text{E.69})$$

We can rewrite (E.69) by first applying Gauß Theorem to obtain:

$$\langle \lambda_0^{\text{eff}^*} \rangle = \frac{1}{|\Omega^*|} \int_{\Omega_a^*} \nabla_{\mathbf{y}^*} \cdot (\lambda_{a,0}^* (\mathbf{y}^* \otimes (\mathbf{I} + \nabla_{\mathbf{y}^*} \otimes \vec{t}_a))) d\Omega^* \quad (\text{E.70})$$

which can be simplified by applying the product rule and (HT_k):

$$\begin{aligned}
& \nabla_{\mathbf{y}^*} \cdot (\lambda_{a,0}^* (\mathbf{y}^* \otimes (\mathbf{I} + \nabla_{\mathbf{y}^*} \otimes \vec{t}_a))) \\
& = \lambda_{a,0}^* (\mathbf{I} \otimes (\mathbf{I} + \nabla_{\mathbf{y}^*} \otimes \vec{t}_a) + \mathbf{y}^* \otimes \underbrace{(\nabla_{\mathbf{y}^*} \cdot (\mathbf{I} + \nabla_{\mathbf{y}^*} \otimes \vec{t}_a))}_{=0, (\text{HT}_k)}) \\
& = \lambda_{a,0}^* (\mathbf{I} + \nabla_{\mathbf{y}^*} \otimes \vec{t}_a)
\end{aligned} \quad (\text{E.71})$$

So we can write:

$$\begin{aligned} \langle \lambda_0^{\text{eff}*} \rangle &= \frac{1}{|\Omega^*|} \int_{\Omega_a^*} \lambda_{a,0}^* (\mathbf{I} + \nabla_{\mathbf{y}^*} \otimes \vec{t}_a) d\Omega^* \\ &= \lambda_{a,0}^* \langle \mathbf{I} + \nabla_{\mathbf{y}^*} \otimes \vec{t}_a \rangle \end{aligned} \quad (\text{E.72})$$

It should be noted, that due to strong contrast in heat capacity of the two phases, expressed by $C = \mathcal{O}(\varepsilon^{-2})$, the heat capacity of phase a is not considered in the storage term to first order of approximation. Similarly, the effective thermal conductivity $\lambda^{\text{eff}*}$ is a function of the thermal conductivity $\lambda_{a,0}^*$ alone, which is the phase with lower thermal conductivity expressed by $\mathcal{L} = \mathcal{O}(\varepsilon^{-1})$ as this corresponds to the case of infinite thermal conductivity of phase b (and thus vanishing temperature gradient across phase b) to first order. The microscopic geometry is accounted for via the solution of the cell problem \vec{t}_a . In dimensional variables we have:

$$(1 - \phi)\rho_b c_b \frac{\partial T}{\partial t} + \nabla_{\mathbf{x}} \cdot (c_a \rho_a T(\vec{v})) - \nabla_{\mathbf{x}} \cdot (\langle \lambda^{\text{eff}} \rangle \nabla_{\mathbf{x}} T) = \phi q_a + \mathcal{O}(\varepsilon) \quad \text{in } \Omega \quad (\text{HT})$$

with the effective thermal conductivity $\langle \lambda^{\text{eff}} \rangle$:

$$\langle \lambda^{\text{eff}} \rangle = \lambda_a \langle \mathbf{I} + \nabla_{\mathbf{y}^*} \otimes \vec{t}_a \rangle + \mathcal{O}(\varepsilon) \quad (\text{E.73})$$

Data availability

The model implementation and data that supports the findings of this study are available on GitHub at - <https://github.com/DavidBrust/MultiComponentReactiveMixtureProject>.

References

- [1] C.K. Ho (Ed.), *Gas Transport in Porous Media*, in: *Theory and Applications of Transport in Porous Media*, vol. 20, Springer, Dordrecht, 2006.
- [2] S. Göll, M. Piesche, Multi-component gas transport in micro-porous domains: Multidimensional simulation at the macroscale, *Int. J. Heat Mass Transfer* 55 (1–3) (2012) 480–487, <http://dx.doi.org/10.1016/j.ijheatmasstransfer.2011.09.049>.
- [3] A.Z. Weber, R.L. Borup, R.M. Darling, P.K. Das, T.J. Dursch, W. Gu, D. Harvey, A. Kusoglu, S. Litster, M.M. Mench, R. Mukundan, J.P. Owejan, J.G. Pharoah, M. Secanell, I.V. Zenyuk, A critical review of modeling transport phenomena in polymer-electrolyte fuel cells, *J. Electrochem. Soc.* 161 (12) (2014) F1254–F1299, <http://dx.doi.org/10.1149/2.0751412jes>.
- [4] C. Agrafiotis, M. Roeb, C. Sattler, A review on solar thermal syngas production via redox pair-based water/carbon dioxide splitting thermochemical cycles, *Renew. Sustain. Energy Rev.* 42 (2015) 254–285, <http://dx.doi.org/10.1016/j.rser.2014.09.039>.
- [5] R. Taylor, R. Krishna, *Multicomponent Mass Transfer*, in: *Wiley Series in Chemical Engineering*, Wiley, New York, 1993.
- [6] E.A. Mason, A.P. Malinauskas, *Gas Transport in Porous Media: The Dusty-gas Model*, vol. Bd. 17, Elsevier, 1983.
- [7] P. Schneider, Multicomponent isothermal diffusion and forced flow of gases in capillaries, *Chem. Eng. Sci.* 33 (10) (1978) 1311–1319, [http://dx.doi.org/10.1016/0009-2509\(78\)85112-4](http://dx.doi.org/10.1016/0009-2509(78)85112-4).
- [8] P.J. Kerkhof, A modified Maxwell-Stefan model for transport through inert membranes: the binary friction model, *Chem. Eng. J. Biochem. Eng. J.* 64 (3) (1996) 319–343, [http://dx.doi.org/10.1016/S0923-0467\(96\)03134-X](http://dx.doi.org/10.1016/S0923-0467(96)03134-X).
- [9] T. Krüger, H. Kusumaatmaja, A. Kuzmin, O. Shardt, G. Silva, E.M. Viggen, *The Lattice Boltzmann Method*, Springer International Publishing, Cham, 2017, <http://dx.doi.org/10.1007/978-3-319-44649-3>.
- [10] G. Kefayati, A. Tolooiyan, A.P. Bassom, K. Vafai, A mesoscopic model for thermal–solutal problems of power-law fluids through porous media, *Phys. Fluids* 33 (3) (2021) <http://dx.doi.org/10.1063/5.0042526>.
- [11] A.Z. Weber, J. Newman, Modeling gas-phase flow in porous media, *Int. Commun. Heat Mass Transfer* 32 (7) (2005) 855–860, <http://dx.doi.org/10.1016/j.icheatmasstransfer.2004.08.026>.
- [12] J. Fuhrmann, et al., VoronoiFVM.jl: Finite volume solver for coupled nonlinear partial differential equations, 2019 - 2024, <http://dx.doi.org/10.5281/zenodo.3529808>.
- [13] A. Van-Brunt, P.E. Farrell, C.W. Monroe, Consolidated theory of fluid thermodiffusion, *AIChE J.* 68 (5) (2022) <http://dx.doi.org/10.1002/aic.17599>.
- [14] G.D.C. Kuiken, *Thermodynamics of Irreversible Processes: Applications to Diffusion and Rheology*, in: *Wiley Tutorial Series in Theoretical Chemistry*, Wiley, New York, NY, 1994.
- [15] V. Giovangigli, *Multicomponent Flow Modeling*, in: *Modeling and Simulation in Science, Engineering, and Technology*, Birkhäuser, Boston and Basel and Berlin, 1999.
- [16] R.J. Kee, M.E. Coltrin, P. Glarborg, H. Zhu, *Chemically Reacting Flow*, second ed., 2017, <http://dx.doi.org/10.1002/9781119186304>.
- [17] R.B. Bird, W.E. Stewart, E.N. Lightfoot, *Transport Phenomena*, second ed., 2006.
- [18] V. Giovangigli, Solutions for models of chemically reacting compressible mixtures, in: *Handbook of Mathematical Analysis in Mechanics of Viscous Fluids*, Springer, 2018, pp. 2979–3030, http://dx.doi.org/10.1007/978-3-319-13344-7_73.
- [19] J. Bzowski, J. Kestin, E.A. Mason, F.J. Uribe, Equilibrium and transport properties of gas mixtures at low density: Eleven polyatomic gases and five noble gases, *J. Phys. Chem. Ref. Data* 19 (5) (1990) 1179–1232, <http://dx.doi.org/10.1063/1.555867>.
- [20] D.A. Nield, A. Bejan, *Convection in Porous Media*, Springer International Publishing, Cham, 2017, <http://dx.doi.org/10.1007/978-3-319-49562-0>.
- [21] J. Bear, S. Whitaker, *The Method of Volume Averaging*, vol. 13, Springer Netherlands, Dordrecht, 1999, <http://dx.doi.org/10.1007/978-94-017-3389-2>.
- [22] M. Quintard, S. Whitaker, Transport in ordered and disordered porous media I: The cellular average and the use of weighting functions, *Transp. Porous Media* 14 (2) (1994) 163–177, <http://dx.doi.org/10.1007/BF00615199>.
- [23] M. Quintard, S. Whitaker, Transport in ordered and disordered porous media II: Generalized volume averaging, *Transp. Porous Media* 14 (2) (1994) 179–206, <http://dx.doi.org/10.1007/BF00615200>.
- [24] M. Quintard, S. Whitaker, Transport in ordered and disordered porous media III: Closure and comparison between theory and experiment, *Transp. Porous Media* 15 (1) (1994) 31–49, <http://dx.doi.org/10.1007/BF01046157>.
- [25] L. Kadanoff, J.E. Marsden, L. Sirovich, S. Wiggins, F. John, U. Hornung, *Homogenization and Porous Media*, vol. 6, Springer New York, New York, NY, 1997, <http://dx.doi.org/10.1007/978-1-4612-1920-0>.
- [26] J.-L. Auriault, C. Boutin, C. Geindreau, *Homogenization of Coupled Phenomena in Heterogeneous Media*, ISTE and Wiley, London and Hoboken, N.J., 2009, URL <https://onlinelibrary.wiley.com/doi/book/10.1002/9780470612033>.
- [27] H.I. Ene, D. Polisevski, *Thermal Flows in Porous Media*, Springer Netherlands, Dordrecht, Netherlands, The, 1987.
- [28] ROBU Glasfilter-Geräte GmbH, VitraPOR sinterfilter borosilicatglas 3.3: Pore properties, 2024, URL https://www.robuglas.com/fileadmin/dateien/Bilder/Service/Downloads/Technische_Daten_im_Detail_eng/poreproperties_vitrapor_e.pdf.
- [29] C. Moyne, T.D. Le, G. Maranzana, Upscaled model for multicomponent gas transport in porous media incorporating slip effect, *Transp. Porous Media* 135 (2) (2020) 309–330, <http://dx.doi.org/10.1007/s11242-020-01478-x>.
- [30] A. Jüngel, Entropy Methods for Diffusive Partial Differential Equations, in: *SpringerBriefs in Mathematics*, Springer, 2016, p. viii+139, <http://dx.doi.org/10.1007/978-3-319-34219-1>.
- [31] A. Jüngel, J. Mikyška, N. Zamponi, Existence analysis of a single-phase flow mixture with van der Waals pressure, *SIAM J. Math. Anal.* 50 (1) (2018) 1367–1395, <http://dx.doi.org/10.1137/16M1107024>.

- [32] P. Grisvard, Elliptic Problems in Nonsmooth Domains, in: *Classics in Applied Mathematics*, vol. 69, Society for Industrial and Applied Mathematics (SIAM), 2011, p. xx+410, <http://dx.doi.org/10.1137/1.9781611972030.ch1>.
- [33] D. Bothe, W. Dreyer, Continuum thermodynamics of chemically reacting fluid mixtures, *Acta Mech.* 226 (6) (2015) 1757–1805, <http://dx.doi.org/10.1007/s00707-014-1275-1>.
- [34] M. Neubronner, T. Bodmer, C. Hübner, P.B. Kempa, E. Tsotsas, A. Eschner, G. Kasperek, F. Ochs, H. Müller-Steinhagen, H. Werner, M.H. Spitzner, D6 properties of solids and solid materials, in: *VDI Heat Atlas*, Springer Berlin Heidelberg, Berlin, Heidelberg, 2010, pp. 551–614, http://dx.doi.org/10.1007/978-3-540-77877-6_26.
- [35] A. Cheilytko, P. Schwarzbözl, K. Wiegardt, Modeling of heat conduction processes in porous absorber of open type of solar tower stations, *Renew. Energy* 215 (2023) <http://dx.doi.org/10.1016/j.renene.2023.118995>.
- [36] ROBU Glasfilter-Geräte GmbH, VitrapOR sinterfilter borosilicatlglas 3.3: Data sheet and properties, 2023, URL https://www.robuglas.com/fileadmin/dateien/Bilder/Service/Downloads/Technische_Daten_im_Detail_eng/datasheet_vitrapor_e.pdf.
- [37] M.A. Schuetz, L.R. Glicksman, A basic study of heat transfer through foam insulation, *J. Cell. Plast.* 20 (2) (1984) 114–121, <http://dx.doi.org/10.1177/0021955X8402000203>.
- [38] J.A. Wesselingh, R. Krishna, *Mass Transfer in Multicomponent Mixtures*, first ed., VSSD, 2006.
- [39] P. Farrell, N. Rotundo, D. Doan, M. Kantner, J. Fuhrmann, T. Koprucki, Numerical methods for drift-diffusion models, in: J. Piprek (Ed.), in: *Handbook of Optoelectronic Device Modeling and Simulation: Lasers, Modulators, Photodetectors, Solar Cells, and Numerical Methods*, vol. 2, CRC Press, Boca Raton, 2017, pp. 733–771.
- [40] H. Si, K. Gärtner, J. Fuhrmann, Boundary conforming delaunay mesh generation, *Comput. Math. Math. Phys.* 50 (2010) 38–53, <http://dx.doi.org/10.1134/S0965542510010069>.
- [41] C. Chainais-Hillairet, Entropy method and asymptotic behaviours of finite volume schemes, in: *Finite Volumes for Complex Applications VII-Methods and Theoretical Aspects: FVCA 7*, Berlin, June 2014, Springer, 2014, pp. 17–35.
- [42] B. Gaudeul, J. Fuhrmann, Entropy and convergence analysis for two finite volume schemes for a Nernst-Planck-Poisson system with ion volume constraints, *Numer. Math.* 151 (1) (2022) 99–149, <http://dx.doi.org/10.1007/s00211-022-01279-y>.
- [43] K. Ehrhardt, K. Klusáček, P. Schneider, Finite-difference scheme for solving dynamic multicomponent diffusion problems, *Comput. Chem. Eng.* 12 (1988) 1151–1155.
- [44] P. Vágner, M. Pavelka, J. Fuhrmann, V. Klika, A multiscale thermodynamic generalization of Maxwell-Stefan diffusion equations and of the dusty gas model, *Int. J. Heat Mass Transfer* 199 (2022) 123405, <http://dx.doi.org/10.1016/j.ijheatmasstransfer.2022.123405>.
- [45] J. Revels, M. Lubin, T. Papamarkou, Forward-mode automatic differentiation in Julia, 2016, [arXiv:1607.07892](https://arxiv.org/abs/1607.07892).
- [46] A. Montoisson, D. Orban, Krylov.jl: A Julia basket of hand-picked Krylov methods, *J. Open Source Softw.* 8 (89) (2023) 5187, <http://dx.doi.org/10.21105/joss.05187>.
- [47] Intel Corporation, oneMKL PARDISO - Parallel direct sparse solver interface, 2024, URL <https://www.intel.com/content/www/us/en/docs/onemkl/developer-reference-c/2024-0/onemkl-pardiso-parallel-direct-sparse-solver-iface.html>.
- [48] P. Krysl, J. Fuhrmann, et al., Sparspak.jl, 2023, URL <https://github.com/PetrKryslUCSD/Sparspak.jl>.
- [49] D. Brust, M. Wullenkord, H.G. Gómez, J. Albero, C. Sattler, Experimental investigation of photo-thermal catalytic reactor for the reverse water gas shift reaction under concentrated irradiation, *J. Environ. Chem. Eng.* 12 (5) (2024) 113372, <http://dx.doi.org/10.1016/j.jece.2024.113372>.
- [50] Y. Dubi, I.W. Un, Y. Sivan, Thermal effects - an alternative mechanism for plasmon-assisted photocatalysis, *Chem. Sci.* 11 (19) (2020) 5017–5027, <http://dx.doi.org/10.1039/c9sc06480j>.
- [51] J. Xu, G.F. Froment, Methane steam reforming, methanation and water-gas shift: I. Intrinsic kinetics, *AIChE J.* 35 (1) (1989) 88–96, <http://dx.doi.org/10.1002/aic.690350109>.
- [52] D. Brust, J. Fuhrmann, MultiComponentReactiveMixtureProject, 2024, <http://dx.doi.org/10.5281/zenodo.10901335>.
- [53] A. Wolf, A. Jess, C. Kern, Syngas production via reverse water-gas shift reaction over a Ni-Al₂O₃ catalyst: Catalyst stability, reaction kinetics, and modeling, *Chem. Eng. Technol.* 39 (6) (2016) 1040–1048, <http://dx.doi.org/10.1002/ceat.201500548>.
- [54] T.L. Bergman, A. Lavine, F.P. Incropera, *Fundamentals of Heat and Mass Transfer*, John Wiley & Sons, Inc, Hoboken, NJ, 2019.
- [55] W. Roetzel, B. Spang, C3 typical values of overall heat transfer coefficients, in: *VDI Heat Atlas*, Springer Berlin Heidelberg, Berlin, Heidelberg, 2010, pp. 75–78, http://dx.doi.org/10.1007/978-3-540-77877-6_6.
- [56] C. Bringedal, I. Berre, I.S. Pop, F.A. Radu, Upscaling of non-isothermal reactive porous media flow with changing porosity, *Transp. Porous Media* 114 (2) (2016) 371–393, <http://dx.doi.org/10.1007/s11242-015-0530-9>.
- [57] C.C. Mei, Method of homogenization applied to dispersion in porous media, *Transp. Porous Media* 9 (3) (1992) 261–274, <http://dx.doi.org/10.1007/BF00611970>.
- [58] M. Gahn, M. Neuss-Radu, I.S. Pop, Homogenization of a reaction-diffusion-advection problem in an evolving micro-domain and including nonlinear boundary conditions, *J. Differential Equations* 289 (2021) 95–127, <http://dx.doi.org/10.1016/j.jde.2021.04.013>.
- [59] F. Kuwahara, M. Shirota, A. Nakayama, A numerical study of interfacial convective heat transfer coefficient in two-energy equation model for convection in porous media, *Int. J. Heat Mass Transfer* 44 (6) (2001) 1153–1159, [http://dx.doi.org/10.1016/s0017-9310\(00\)00166-6](http://dx.doi.org/10.1016/s0017-9310(00)00166-6).